2-1-2016

RELATIVISTIC BACKWARD WAVE OSCILLATOR WITH A GAUSSIAN RADIATION PATTERN AND RELATED TECHNOLOGIES

Ahmed Elfrgani

AHMED M. ELFRGANI
Candidate

Electrical and Computer Engineering
Department

This dissertation is approved, and it is acceptable in quality and form for publication:

Approved by the Dissertation Committee:

Edl Schamiloglu , Chairperson

Mark Gilmore

Christos Christodoulou

Anil Prinja

RELATIVISTIC BACKWARD WAVE OSCILLATOR WITH A GAUSSIAN RADIATION PATTERN AND RELATED TECHNOLOGIES

by

AHMED ELFRGANI

B.Sc., Electrical & Electronic Engineering,
University of Benghazi, Libya, 2004
M.Sc., Electrical & Electronic Engineering,
University of Benghazi, Libya, 2008

DISSERTATION

Submitted in Partial Fulfillment of the
Requirements for the Degree of

Doctor of Philosophy
Engineering

The University of New Mexico
Albuquerque, New Mexico

December, 2015

DEDICATION

I dedicate this to my parents, my wife, and my siblings who gave me support, inspiration and ultimatum to finish my dissertation. I also dedicate this work to every organization and institution that has invested in me.

ACKNOWLEDGEMENTS

I would like to thank my advising professor, Edl Schamiloglu, for accepting me as his student and for his support and guidance. I wish to thank Prof. Mikhail Fuks, my co-author, for his ideas, helpful discussions, and guidance. I also would to thank Prof. Christos Christodoulou, Prof. Mark Gilmore, and Prof. C. Jerald Buchenauer for their help over the past 5 years. I gratefully acknowledge the assistance of my dissertation committee members: Prof. Christos Christodoulou, Prof. Mark Gilmore, and Prof. Anil Prinja.

I am thankful to Jerald Buchenauer, Chris Leach, Sarita Prasad, Jeremy McConaha for helping in the electrodynamic components design and manufacturing, and high voltage experiment. I am also thankful to Prof. Christos Christodoulou, who allowed me to fabricate the cold test set up in his lab, and I want to thank Firas Ayoub, Sabahattin Yurt, and Georgios Atmazakis for helping me with the cold test measurements.

Finally, the research performed as part of this Dissertation was partially supported by AFOSR Grants FA9550-11-1-0200, FA9550-15-1-0094, and ONR Grant N000141310565.

RELATIVISTIC BACKWARD WAVE OSCILLATOR WITH A GAUSSIAN RADIATION PATTERN AND RELATED TECHNOLOGIES

by

AHMED ELFRGANI

B.Sc., Electrical & Electronic Engineering, University of Benghazi, Libya, 2004

M.Sc., Electrical & Electronic Engineering, University of Benghazi, Libya, 2008

Ph.D., Electrical & Computer Engineering, University of New Mexico, Albuquerque, New Mexico, USA, 2015

ABSTRACT

Short pulse high power microwave (HPM) devices with Gaussian radiation pattern are attractive for many applications. The importance of the Gaussian microwave beam is that its maximum energy density is concentrated on axis. The purpose of this study is to use a backward wave oscillator (BWO), which is typically known to radiate in the TM_{01} mode, to produce an HPM Gaussian wave beam.

A BWO generates an electromagnetic wave with negative group velocity where the wave is traveling in the direction opposite to the electron beam. Thus, to extract the microwave signal axially, a cavity resonator reflector or cutoff waveguide section are widely used to reflect the TM_{01} mode backward wave to a TM_{01} mode forward wave. To provide a HPM Gaussian-like TE_{11} wave beam, an X-band relativistic BWO (RBWO) is proposed that uses a Bragg reflector instead of a cavity resonator reflector. Therefore, the device of interest is a RBWO consisting of two periodic slow wave structures (SWSs).

In the original design, the inner radii of both SWSs were the same. For a uniform electron beam, a Bragg structure that is placed at the cathode (upstream) end, unfavorably perturbed the electron beam. Thus, two designs were proposed to minimize the interaction between the electron beam and the Bragg reflector structure. First, a uniform magnetic field was used with increased radial gap between the electron beam and the structure by optimizing the Bragg structure dimensions. This configuration generated a single frequency at X-band. The second design used a nonuniform magnetic field to control the gap between the electron beam and the SWSs, and to optimize the electron beam-Bragg structure interaction for C-band radiation generation. This is a dual-band RBWO operation with a possibility of generating a TE_{11}-mode with linear polarization at single or dual frequencies (X- and C-bands).

The radiation at C-band was generated in the Bragg structure as an asymmetric mode. The only known way to extract such a wave is by using a cutoff neck section. The disadvantage of the cutoff neck reflector is its proximity to the electron beam, and that leads to beam scrape-off and alignment difficulty. A novel idea of combining a periodic SWS with an electromagnetic band gap (EBG) medium for coupling and extracting a Gaussian radiation pattern is presented.

Finally, it is well known that the power handling ability of a single RBWO is limited by material technology. Since it is always desired to generate higher microwave power than a single microwave device can produce, an N-way power combiner is proposed as an attractive alternative. A novel structure, which is an oversized circular waveguide to overcome standard waveguides limitations, is designed for power combining and higher order mode output.

TABLE OF CONTENTS

LIST OF FIGURES

LIST OF TABLES

CHAPTER 1. INTRODUCTION

Microwave tubes are electronic devices that convert electron beam energy into RF energy to be used mainly as oscillators or amplifiers. At low microwave power levels, the microwave tubes perform the same functions as conventional vacuum tubes did and solid state semiconductor transistors do, but operate in the microwave frequency spectrum. They differ from vacuum tubes and semiconductor transistors in that their basic principles of electronic operation are different and the microwave circuits are integral parts of the microwave tubes. At high power levels, microwave tubes are presently the only option to generate megawatts of microwave power or greater [1]. The basic operating principle of all microwave oscillators and amplifiers are the same and may be explained using Fig. 1.1.

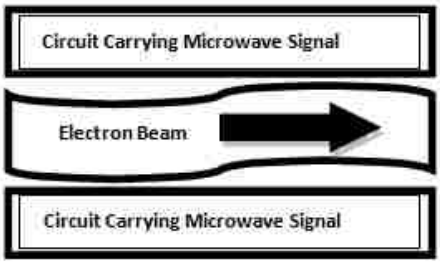

Figure 1.1 Simplistic view of a microwave tube [2].

An electron gun (or an electron beam accelerator) is used to produce an electron beam, a power supply source is used to drive the electron gun, a collector is used to dump the electron beam, a focusing magnet (or a pulsed magnetic circuit with a solenoid) is used to guide the electrons, and a circuit carrying microwave signal (slow wave structure - SWS) are the main components of a microwave device. For HPM an electron beam accelerator

provides a high voltage pulse for electron beam excitation and a solenoid generates a magnetic field to guide the electron beam through a linear device. The circuit shown in Fig. 1.1 is constructed so that the velocity of the traveling electromagnetic signal is close to the velocity of the electron beam passing through the tube near the circuit [1–4].

HPM sources have potential uses in many different scientific areas, such as in radar systems, to solve environmental problems, in materials science, in medicine, for confined thermonuclear fusion, and in linear accelerators. These sources provide high peak power with a high degree of stability in repetitively pulsed operation [1].

Generally, HPM sources (or microwave tubes) can be divided into O-type and M-type devices. Traveling wave tubes (TWTs) and BWOs are called O-type devices because the electrons travel along the axial magnetic field that guides them through the tube. In contrast, in M-type devices, such as the magnetron, the electron beam interacts with electromagnetic waves in crossed electric and magnetic fields.

The relativistic BWO (RBWO), relativistic TWT, dielectric Cerenkov maser (DCM), and plasma Cerenkov maser (PCM) are all classified as O-type Cerenkov devices. The reason for calling them Cerenkov devices is that the electrons radiate in a manner analogous to electrons emitting Cerenkov radiation when they travel through a medium at a velocity greater than the characteristic light speed in the medium.

O-type Cerenkov devices function on the same principle of operation, in which an external circuit reduces the phase velocity of the eigenmodes (modes are the distribution of fields) to less than the speed of light. The electron beam velocity and the phase velocity of the electromagnetic wave will be close (synchronous) to allow the kinetic energy of the electrons to be transferred to the waves. In other words, the electron beam

provides the energy source for the microwaves, while the periodic SWS provides a set of slow waves that can interact resonantly with space-charge waves on the beam to extract energy as microwaves.

From the wide spectrum of generators of high power coherent radiation, the BWO can be considered as one of the most popular. This is attributed to its high degree of adaptability to variations in electron beam parameters and to its rapid risetime of the oscillations. The simple design of the BWO's electrodynamic system also accommodates large electrical field stresses within the circuit. Furthermore, BWOs can operate in both the single-shot and repetitive regimes with gigawatt power output.

O-type Cerenkov devices are known to radiate a symmetric field pattern (TM_{0n} modes) with an energy distribution off axis. This is not attractive for many applications that require the electromagnetic energy to be concentrated on axis. The goal of the research described in this dissertation is to investigate the possibilities of generating a Gaussian wave beam from a BWO.

1.1. Motivation

The motivation for this work is to create a short pulse microwave source that outputs a Gaussian wave beam with linear polarization. This is attractive for many applications such as excitation of plasmas in different gases, plasma diagnostics, sounding systems, and for short pulse radar, among others. For instance, radiation in the form of short nanosecond pulses makes it possible to detect small targets moving amidst heavy clutter, as was realized in the NAGIRA radar [1,5]. The NAGIRA radar used a RBWO as a source to radiate short pulses with symmetric radiation. In the research described in this

dissertation, the suggested design is to use a Bragg reflector in NAGIRA's RBWO to produce a linearly polarized Gaussian wave beam.

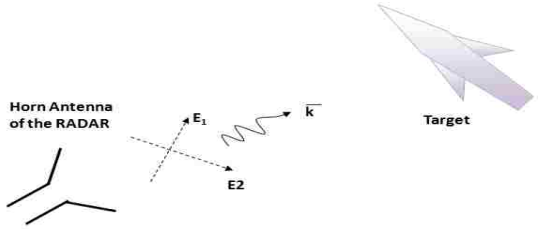

Figure 1.2 Schematic of a radar with linearly polarized microwave pulses.

For radar applications, frequency tuning makes it difficult to determine a radar's location for purpose of jamming, whereas changing the direction of the linear polarization gives information about a target's configuration. Figure 1.3 shows examples of different reflections from an ellipsoidal target for different polarization vectors of linear polarization.

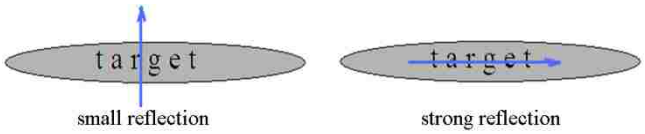

Figure 1.3 Reflections of radiation with different vectors of linear polarization from an ellipsoidal target.

The importance of a Gaussian microwave beam is that its maximum energy density is concentrated on axis. A Gaussian radiation pattern is formed as a combination of 85% TE_{11} mode and 15% TM_{11} mode in a smooth circular waveguide [6]. As is well known, a corrugated horn antenna creates a Gaussian beam from the TE_{11} mode by forming an appropriate relative phasing. Therefore, the main task is to create a microwave source generating the TE_{11} mode and couple to the fundamental free space Gaussian mode at the open ended waveguide.

In RBWOs, the TM_{01} mode is generated with negative group velocity where the wave is traveling in a direction opposite to that of the electron beam. Therefore, to extract the

microwave signal axially, a cavity resonator reflector or a cutoff neck section is widely used to reflect the backward TM_{01} wave to a forward TM_{01} wave. To provide high power Gaussian radiation, a RBWO is proposed that uses a Bragg reflector instead of a cavity resonator reflector to reflect the backward TM_{01} wave and self-consistently convert it to a forward TE_{11} wave. A linearly and circularly polarized TE_{11} mode with a Gaussian beam can be produced using the Bragg reflector.

In addition, RBWOs can generate such Gaussian pulses by either converting the generated wave to a TE_{11} mode using a mode converter, or by designing a SWS able to generate it directly. We propose an electrodynamic system for a BWO that is designed to generate a TE_{11}-like mode and a novel EBG structure is designed for asymmetric mode extraction.

Several techniques were investigated to provide TE_{11} mode radiation with different polarizations for BWOs:

1. A serpentine mode converter [7] can be used to convert the TM_{01} mode to the TE_{11} mode with linear polarization at the output. However, in order to change the polarization vector of the linear polarization, both the converter and the huge reflectors that form a narrow microwave beam in radars must be rotated because the input axis of the converter is not coincident with its output axis.

2. A corrugated waveguide converter [8] at the output of the BWO converts the TM_{01} mode to the TE_{11} mode. However, such a mode converter is inconvenient because it is very long [9].

3. Cyclotron mode selection [10] can be used in a BWO to produce a circularly-polarized TE_{11} mode. The mode selection method in an oversized SWS is one of the most challenging problems in microwave electronics [11-13].

4. A Bragg reflector with single-fold-spiral corrugation at the upstream end of a BWO's SWS can be used to convert the backward TM_{01} mode to a forward circularly-polarized TE_{11} mode [14,15].

These options were carefully studied and reviewed. Because our goal was to form a Gaussian pattern with linear polarization, our first decision was to use a modified version of the fourth option. A two-spiral corrugated Bragg reflector at the upstream end of the BWO's SWS was used to convert the operating backward TM_{01} mode to a forward TE_{11} mode with linear polarization. The third option is a possible choice, but the only way to extract the Gaussian radiation is by using a cutoff section. Thus, an EBG medium was proposed as an extraction scheme. Finally, an N-way power combiner was designed based on the first option to produce a Gaussian beam.

1.2. Historical Background

For a long time klystrons and magnetrons were the most commonly used microwave tubes. During World War II, Rudolf Kompfner invented the TWT while working for the British tube establishment [16], and the BWO followed immediately after the war. Perhaps, the first to propose the idea of a helix TWT amplifier in patent was Lindenblad in 1942. Years later, a BWO utilizing intense relativistic beam technology marked the beginning of the HPM era. In the early 1970s, experiments at Cornell University [17,18], the Institute of Applied Physics in Nizhny Novgorod, and the Lebedev Institute in

Moscow [19,20] demonstrated the first true HPM source, a RBWO that produced single nanosecond, 10s-100s MW pulses with about 12% efficiency. Since then, no really major breakthroughs in theory have occurred. In the late 1970s, using a simple numerical model, it was shown that the energy exchange efficiency of uniform ultrarelativistic BWOs can reach 15%. This can be further increased to more than 45% using a jump in coupling impedance or a variable coupling impedance distribution within the device [21,22]. By the early 1980's, BWO efficiencies as high as 30% were achieved using nonuniform SWSs with a variable coupling impedance distribution [23]. Another possibility lies in changing the phase velocity at the end of the interaction region which is similar to velocity tapering in nonrelativistic TWTs [24].

The electromagnetic radiation pattern from the above devices was concentrated off axis. In 2000, an RBWO with asymmetric wave operation was experimentally investigated [25]. A Bragg structure was used as a selective mode converter for an RBWO [15,26], although various types of Bragg resonators operating at millimeter wavelengths were investigated for free electron lasers in the early 1980s [27]. The dependence of the frequency spectrum and field distributions on the corrugation structures were investigated for different coupled modes with phase velocities at speeds close to the speed of light. The modes were identified by determination of their azimuthal and longitudinal indexes. By the late 1980s these resonators were experimentally investigated and compared to the theoretically calculated formulas [27].

1.3. Organization of the Dissertation

The main part of this work describes the results of simulations comparing and contrasting the experiment of a BWO with linearly polarized Gaussian radiation. In the simulations, the fully electromagnetic software tools ANSYS-HFSS [28] and CST-MWS [29] were used for cold test investigation, while the fully electromagnetic, relativistic PIC code MAGIC [30] was used to simulate the device for the hot test. In the experimental work, SINUS-6 electron accelerator was used to provide the RBWO with a half-sine-wave-like high-voltage pulse.

The remainder of this dissertation is organized as follows: Chapter 2 discusses the linear field theory and modeling of the BWO and Bragg structures. A description of a single band HPM source physics and simulation results are presented in Chapter 3. Chapter 4 is devoted to experiments that were performed at the University of New Mexico (UNM) to compare the experimental results with the analytical (Chapter 2) and simulation (Chapter 3) results. Chapter 5 explores the development of a dual band HPM source. The design of a C- and X- band RBWO was discussed and verified using MAGIC PIC code simulatoins. Chapter 6 discusses a novel way of asymmetric mode extraction using an EBG. Microwave power combining structures were designed and tested using HFSS and are described in Chapter 7. Conclusions and future work appear in Chapter 8.

CHAPTER 2. THEORY

A linear theory was first developed by Pierce [31,32] for low power TWTs and BWOs. An equivalent circuit model [33] was also developed to understand low power oscillators. For high current BWOs, the behavior of the devices should be described by nonlinear theory. In the nonlinear theory, a number of important effects that are ignored in the framework of the linear theory are taken into account. For instance, change in the average electron velocity, electrons overtaking one another, and deformation of bunches, among other physics, are not considered in the linear theory. A comprehensive nonlinear theory of stationary oscillations in nonrelativistic BWOs was developed by Rapoport [34,35]. In 1975, Kovalev [36] expanded the nonlinear theory of a nonrelativistic BWO to an ultrarelativistic version. Fortunately, the nonlinear results can be obtained through numerical solution of approximated nonlinear equations. The PIC code, which became a reliable virtual prototyping tool in the mid-1990s, includes the nonlinear effects. The MAGIC PIC code will be used in this dissertation to study the BWO, while the analytical theory will be used to understand the results. In the linear field theory treatment, the effect of various parameters of simple physical significance is apparent, and this assists in making and in evaluating the effect of some rather drastic approximations that appear to be necessary in simplifying the problem [31]. A comprehensive theoretical treatment of an infinitely long cylindrical waveguide is discussed and then extended to be applied to different periodic SWSs of BWOs.

The dispersion characteristic of a SWS is an important relation to understand any system based on periodic SWS. In fact, any SWS can interact with an electron beam to

form an oscillator and any SWS can be used as a Bragg structure if the system satisfies certain condition.

2.1. BWO Principle of Operation

The basic component of BWOs is a strong magnetic field that guides an electron beam through a SWS, as shown in Fig. 2.1. This strong static magnetic field (B_s) makes the azimuthal motion of electrons negligible so that the electrons move only in the axial direction. However, for weak magnetic fields, the azimuthal motion affects the interaction between the electrons and the SWS.

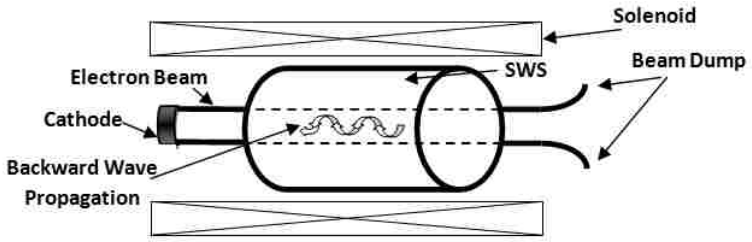

Figure 2.1 The basic components of a BWO.

In a BWO the axial electric field component interacts with the negative energy space-charge wave to bunch the beam and transfer electron kinetic energy to the microwave fields. The eigenmodes of the structure have a negative group velocity so that the energy will transfer to microwaves in a direction opposite to the electron beam streaming direction, and for this reason these devices are called backward-wave devices.

The linearized normal modes for electromagnetic waves in an infinitely long circular waveguide can be decomposed into two independent modes (TE and TM). The TM modes in periodic structures always have an axial electric field component. Indeed, if the

waveguide is corrugated, it would be useful to define the field inside the waveguide by hybrid modes HE and EH. The modes are called HE modes when the TE (H) wave predominates and are called EH modes when the TM (E) wave predominates [37]. Ideally, the TE modes do not perturb the electron motion, because there is no axial electric field component (E_z) of the wave. However, TM modes (or E-waves) and hybrid (HE and EH) modes have an E_z component that perturbs the longitudinal velocity of the beam density, and cause instabilities.

The instabilities that can exist in a BWO (as well as in a TWT) are a type of streaming instability. The physics of the transfer of energy is similar to the two stream instability where the electrons are bunched and decelerated, and then give their energy to the wave. The two stream instability is basically an inverse of nonlinear Landau damping, where the electromagnetic waves give the energy to the electron beam. However, it should be mentioned here that the electron beam cannot give its energy to the wave for an indefinite period of time. When the wave amplitude reaches some value the electrons will be trapped in the negative potential minimum of the wave and will no longer give their energy to the wave. As a result, the electron beam velocity reduces to slightly less than the phase velocity of the electromagnetic wave and the electrons start gaining energy from the waves, which is the Landau damping phenomenon.

The electromagnetic wave in a microwave vacuum tube has a temporal and a spatial dependence, and the electron beam causes the wave to vary slowly in time and axial distance. The spatial growth is measured by the imaginary part of the wavenumber (h_z) and the temporal growth by the imaginary part of the frequency (ω) in the complex dispersion curve plane. For BWOs, the instability is called an absolute instability and is

obtained whenever the wavenumber has two roots and the imaginary part of angular frequency is positive [38, 39]. The two roots are basically the electron beam velocity (v_b = V_1) and the phase velocity of the SWS normal mode (V_2), as shown in Fig. 2.2 [40].

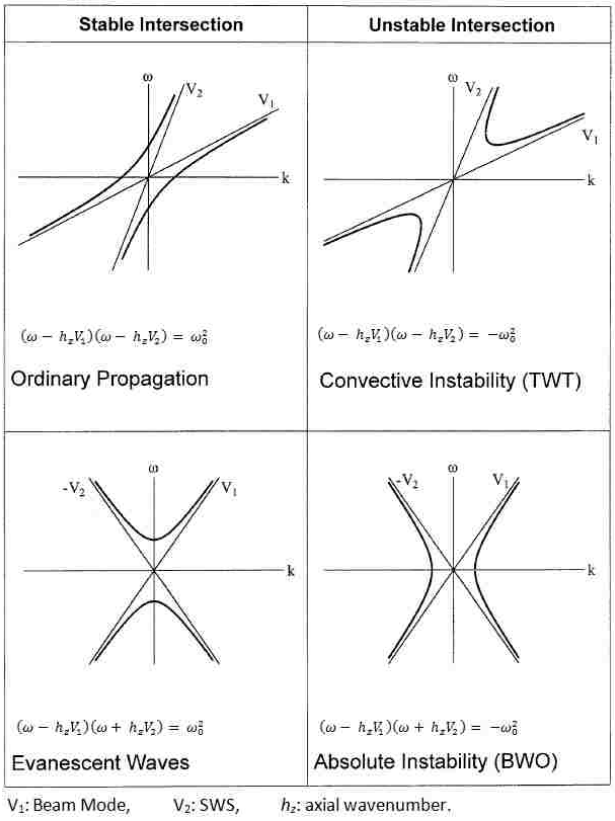

Figure 2.2 Two types of intersection of beam modes with the dispersion relation of SWS [40].

Figure 2.2 shows the four possibilities of the two stream instability. The first category is a stable interaction between the electron beam and the SWS mode and no energy exchange to cause instability is present. The second category is unstable interactions and the complex conjugate roots of the angular frequency arise near the interaction that corresponds to either a convective or absolute instability. In the case of the absolute instability, the wave grows everywhere, which is in contrast to the convective instability where the wave grows as it propagates (such as is the case for a TWT). This is true for

infinite systems, and it is not true that any system that supports an absolute instability is unstable. It usually requires some minimum length for some specific wavenumber to make the BWO unstable.

2.1.1. BWO Modeling and Analysis

A linear treatment is used to analyze the RBWO [41]. The equation of motion and the continuity equation, together with Maxwell's equations will complete the cold fluid model description. In this Subsection, two-stream instability analysis, which is widely discussed in plasma physics [42], is used to develop the treatment.

In electron beam devices, an electron beam is injected through a structure capable of propagating a slow electromagnetic wave with an electric field in the direction of electron motion. In order to generate electromagnetic waves in these devices, two basic conditions must be satisfied: (1) an axial component of the electric field must exist to satisfy the Poynting theorem, and (2) the phase velocity of the wave must be slightly less than the beam velocity, which is called the Cerenkov resonance condition. If the electron beam is injected inside a smooth wall waveguide, the Cerenkov resonance cannot be satisfied. This is due to the fact that the phase velocity of electromagnetic waves in a smooth wall waveguide is greater than the speed of light (fast waves), and the electron velocity cannot exceed the speed of light. Therefore, perturbation of the wall radius of the waveguide to form a SWS is one technique widely used. A variety of BWO designs have been published using different SWSs such as a helix [33], a rippled wall waveguide [19], a waveguide coated with a dielectric [43], or an iris-loaded waveguide [44]. In this work,

two SWSs with sinusoidal wall profile were considered. The profile, in azimuthal (ϕ), radial (r) and longitudinal (z) directions of the cylindrical coordinate, is described by

$$r_w(r, \varphi, z) = r_0 + r_1 \sin(\bar{h}z + \bar{m}\varphi), \qquad (2-1)$$

where r_0 and r_1 are the mean waveguide radius and the amplitude of the corrugation, respectively, $\bar{m}$ is the number of folds, $\bar{h} = 2\pi/d$, and d is the SWS period, as shown in the Fig. 2.3.

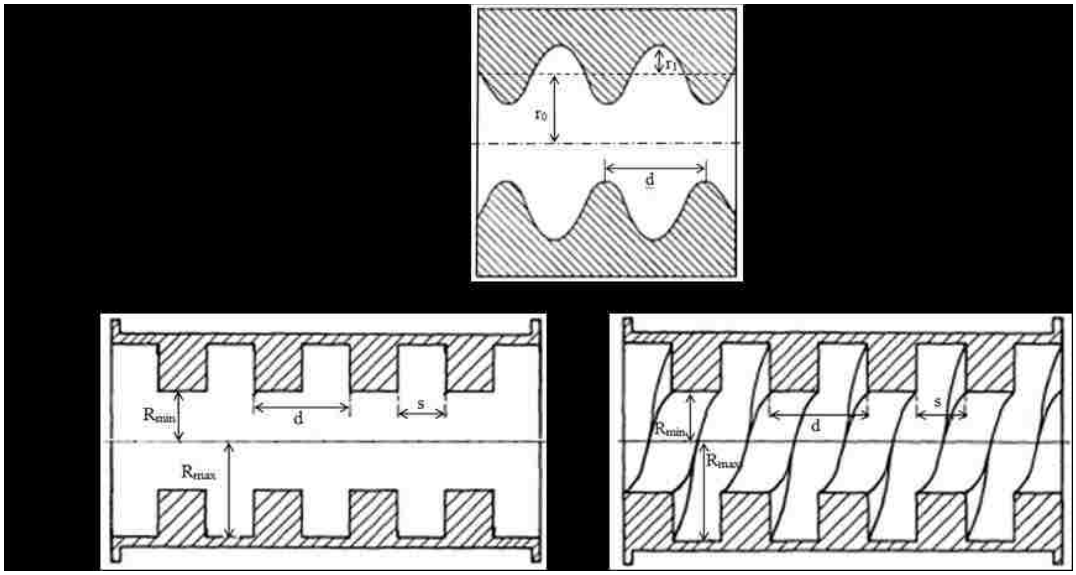

Figure 2.3 Model of the rippled wall SWS. a) sinusoidal rippled wall SWS; b) rectangular rippled wall SWS with ψ=0; c) spiral corrugated SWS; $\psi = \tan^{-1}(d/2\pi R_{max})$.

The number of folds is zero for the axisymmetric SWS, while the spiral-corrugated SWS has a single fold ($\bar{m} = \pm 1$, different signs are related to left- and right-spirals). In addition, the pitch angle (ψ =0) is zero for the axisymmetric SWS and $\psi = \tan^{-1}(d/2\pi R_{max})$ for the spiral corrugated waveguide.

The perturbed region of the waveguide behaves like an artificial dielectric or a high impedance surface, and supports surface waves. In order to simplify the problem, the

waveguide perturbation filling the entire region of an infinite system will be considered first, and then a practical SWS (Fig. 2.3) will be analyzed.

2.1.1.1. Electron Beam in Cylindrical Waveguide

Consider a circular waveguide of radius r_0 filled with an artificial dielectric or a high impedance surface which supports surface waves, and an electron beam with radius r_b injected into it. Linearization of the equation of momentum and continuity equation is the starting point in the treatment of such a system:

$$\frac{\partial \vec{P}}{\partial t} = -e\vec{E} - e\,\vec{v} \times \vec{B} - e\,\vec{v} \times \overrightarrow{B_s}, \qquad (2-2)$$

$$\frac{\partial n}{\partial t} + \nabla.(n\vec{v}) = 0, \qquad (2-3)$$

where $\vec{p} = \gamma m_0 \vec{v}$ is the momentum, γ is the relativistic factor, n is the electron density, and m_0 and e are the electron rest mass and energy, respectively. In addition, $\vec{v}$ is the electron velocity, $\vec{E}$ is the electric field, $\vec{B}$ is the magnetic field, and $\overrightarrow{B_s}$ is the static magnetic field in the axial (z) direction. The initial state will be considered as an equilibrium state that cannot contribute to wave generation. Thus, the electron density and velocity can be written as a sum of equilibrium values (n_0 and $\overrightarrow{v_0}$) and perturbed values (n_1 and $\overrightarrow{v_1}$). The relativistic factor terms can be simplified by using polynomial expansion as in

$$\gamma = \left(1 - \frac{v^2}{c^2}\right)^{-\frac{1}{2}} \approx \gamma_0 + \gamma_0^3 \frac{v_0 v_1}{c^2} = \gamma_0 + \gamma_0^3 \beta_0^2 \frac{v_1}{v_0}, \qquad (2-4)$$

where $\gamma_0 = (1-\beta_0^2)^{-1/2}$ is the initial electron beam relativistic factor, $\beta_0 = \frac{v_0}{c} = (1-\gamma_0^{-2})^{-\frac{1}{2}}$, and c is the speed of light. The velocity of the electrons has only an axial component (a *z*-component) because of the strong static magnetic field assumption, and the electron velocity depends on the electric field. Thus, the last two terms in the right hand side of the equation of motion (2 – 2) will be neglected since the velocity in the *z*-direction appears in both sides of the equation. As a result, the axial component of the equation of motion and the continuity equation can be written in time-harmonic form as follows

$$im_0 v_1 \gamma_0^3 (\omega - h_z v_0) = eE_z, \qquad (2-5)$$

$$n_1(\omega - h_z v_0) - h_z v_0 v_1 = 0, \qquad (2-6)$$

where h_z is the axial wavenumber of the wave, E_z is the longitudinal component of the electric field, and ω is the operating frequency. From (2 – 5) and (2 – 6), the electron beam current can be written as

$$\vec{J} = -en\vec{v} = \frac{-\omega\, e^2 n_0 E_z}{im_0\gamma_0^3\,(\omega - h_z v_0)^2}\hat{z} = \frac{-\omega\,\omega_p^2 \epsilon_0 E_z}{i\gamma_0^3\,(\omega - h_z v_0)^2}\hat{z}, \qquad (2-7)$$

where ω_p is the relativistic electron beam plasma frequency and ϵ_0 is the free space permittivity. In fact, the axial field component is a response of the electron beam, which is the energy source of the system. To relate the electron beam current and the structure fields, Maxwell's equations should be solved to relate the field components by applying the boundary conditions of the system. Equation (2 – 7) is the relativistic Ohm's law. For this Ohm's law Maxwell's equations split into equations for TM waves and TE waves in

a circular waveguide. For the TM wave, the ϕ component of the magnetic field and the *r* and *z* components of the electric field are perturbed. The *r* and *z* components of the magnetic field and the ϕ component of the electric field are perturbed for the TE wave [45].

The result of the time-harmonic field solution is the vector wave equation with the space-charge and the current density terms (2 – 7), which can be written as:

$$\nabla_T^2 E_z + k_\perp^2 \left(1 - \frac{\omega_p^2}{\gamma_0^3 (\omega - h_z v_0)^2}\right) E_z = 0, \qquad (2-8)$$

$$\nabla_T^2 H_z + k_\perp^2 H_z = 0, \qquad (2-9)$$

where $\nabla_T^2 = \frac{1}{r}\frac{\partial}{\partial r}\left(r\frac{\partial}{\partial r}\right) + \frac{1}{r^2}\frac{\partial^2}{\partial \phi^2} = \frac{1}{r}\frac{\partial}{\partial r}\left(r\frac{\partial}{\partial r}\right) + \frac{m^2}{r^2}$ is the transverse Laplacian operator, $k_\perp^2(\omega, h_z) = (k^2 - h_z^2)$ is the transverse wavenumber, $k = \frac{\omega}{c} = \frac{2\pi}{\lambda}$ is the TEM free space wavenumber, λ is the operating wavelength, and *m* is the azimuthal harmonic number (the angular dependent of a mode). The last term in the left hand side of (2 – 8) is the source function; $\sigma(\omega, h_z) = \left(\frac{k_\perp^2 \omega_p^2}{\gamma_0^3 (\omega - h_z v_0)^2}\right)$.

The source function consists of the dispersion function of the electromagnetic wave and the dispersion relation of the electron beam in the relativistic case. According to Uhm [46], the source function term should be modified to include the E_z perturbation and the absolute instability effect on the electron beam as

$$\sigma(\omega, h_z) = \left(\frac{k_\perp^2 \omega_p^2}{\gamma_0^3 \left(\omega - h_z v_0 + \frac{i\Delta h_z}{\gamma_0^3 m_0}\right)^2} \right), \qquad (2-10)$$

where Δ is a constant related to the growth rate and beam spread (usually, 2-4%).

Since the electron beam has only an axial velocity component, the longitudinal component of the electric and the magnetic fields are the most important components. The ϕ and r components of the fields can be found from the solution to Maxwell's equations and applying the boundary conditions for any structure. From (2 – 8) and (2 – 9), the presence of the beam has no effect whatsoever on the H_z component (the $TE_{m\rho}$ mode) but it has a great effect on E_z component (the $TM_{m\rho}$, $HE_{m\rho}$ and $EH_{m\rho}$ modes). The solution of the cold wave equation by using separation of variables [37] is the Bessel ($J_m(x)$) and Neumann ($Y_m(x)$) functions of order m in the radial direction, a sum of sine and cosine functions (and/or complex exponential functions) in both the azimuthal and axial directions as follows

$$\left.\begin{matrix} E_z(r,\phi,z) \\ H_z(r,\phi,z) \end{matrix}\right\} = [A_1\, J_m(k_\perp r) + A_2\, Y_m(k_\perp r)] \times [A_3 \cos(m\phi) + A_4 \sin(m\phi)] \times \left[A_5\, e^{-ih_z z} + A_6 e^{ih_z z}\right] e^{-i\omega t}. \quad (2-11)$$

The transverse wavenumber can be written in terms of the zeroes of the Bessel function of the first kind for $TM_{m\rho}$ modes or the zeroes of the derivative of the Bessel function of the first kind for $TE_{m\rho}$ modes ($k_\perp = \frac{x_{m\rho}}{r_0}$).

For purposes of analysis, the region inside the structure is divided into several regions in the radial direction. The constants $A_{1\text{-}6}$ can be found by matching the boundary conditions between these regions. The modes of interest are modes having m = 0, 1 with an excitation such that A_4 = 0 for E_z solutions and A_3 = 0 for H_z solutions. The waves in (2 – 11) are two oppositely propagating waves and either A_5 or A_6 terms will be zero for

studying a traveling wave in a certain direction. In addition, only the region contains the axis (r=0), forcing A_2 term to be zero because $Y_m(k_\perp r)$ are asymptotic to $-\infty$ on the axis (possess a singularity). That allows us to simplify the wave equation solution to

$$\left.\begin{matrix} E_z(r,\phi,z) \\ H_z(r,\phi,z) \end{matrix}\right\} = \left\{\begin{matrix} E_z(r)\cos(m\phi) \\ H_z(r)\sin(m\phi) \end{matrix}\right\} e^{i(h_z z - \omega t)}, \qquad (2-12)$$

where

$$\left.\begin{matrix} E_z(r) \\ H_z(r) \end{matrix}\right\} = [A_1 J_m(k_\perp r) + A_2 Y_m(k_\perp r)].$$

From the above, one needs to understand the electron beam dynamics and the electromagnetic properties of the device. First, the cold dispersion characteristics of the electromagnetic structure will be studied (Sec. 2.1.1.2). Then the effect of the electron beam will be added (Sec. 2.1.1.3). In fact, dividing the region inside the structure into several sub-regions and matching the boundary conditions of the fields between them is not only important to find the cold wave equation constants, but also is necessary to find both the cold and the hot characteristic equations of the structure, as shown in Fig. 2.4.

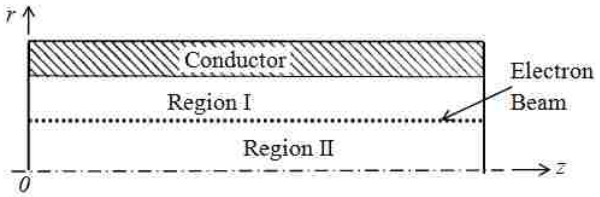

Figure 2.4 A relativistic electron beam in a circular waveguide.

Generally, the structure should exceed a certain length and the electron beam current should exceed a starting threshold (see Sec. 2.1.1.4) in order to have an absolute instability and oscillations.

2.1.1.2. Cold Dispersion Characteristics of SWS

To find the cold dispersion relation of the SWS, the structure is divided into two regions: the corrugation (or groove) space and the center space, as shown in Fig. 2.5. The center region is from the center of the waveguide to the inner radius of the corrugation, while the groove region is between the inner and the outer radii of the corrugation. The wave in the center region is called a volume wave or a fast wave since its phase velocity is greater than the speed of light. The wave near the wall of the groove region is a surface wave or a slow wave since its phase velocity is less than the speed of light. The two regions are considered separately, and the dispersion relation is obtained by matching the fields at the boundary between them.

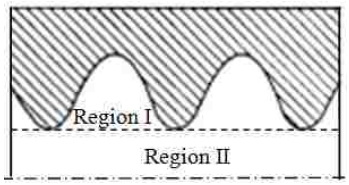

Figure 2.5 A SWS with a sinusoidal profile is divided into two regions.

In this work, two SWSs were considered: a spiral and an axisymmetric corrugated SWSs, as described in (2 – 1). The dispersion relation of an axisymmetric corrugated SWS (such as an iris or disk-loaded waveguide) is well known [44] and simpler to derive. Since the axisymmetric structure can be considered as a special case of the spiral one, the analysis is introduced for the spiral (or helical) corrugation waveguide, and then the dispersion relation of the axisymmetric SWS is obtained.

A periodic SWS has the property that its modes are composed of a Fourier sum of waves, some of which are suitable for synchronism with the electron beam. Thus, the

fields have *z*-directed components that are expanded in a Fourier series, and can be written according to Floquet's theorem as

$$\left.\begin{matrix} E_z(r,\phi,z) \\ H_z(r,\phi,z) \end{matrix}\right\} = \sum_{n=-\infty}^{\infty} \left\{\begin{matrix} E_{zn}(r)\cos(m\phi) \\ H_{zn}(r)\sin(m\phi) \end{matrix}\right\} e^{i(h_n z - \omega t)}, \qquad (2-13)$$

where

$$\left.\begin{matrix} E_{zn}(r) \\ H_{zn}(r) \end{matrix}\right\} = [A_{1n} J_m(k_{\perp n} r) + A_{2n} Y_m(k_{\perp n} r)],$$

E_{zn} is the n[th] spatial harmonic ($n = 0, \pm 1, \ldots$) of E_z and

$$h_n = h_z + n'\bar{h};\ \ n' = \begin{cases} n; & \text{for azimuthally symmetric modes } (m = 0) \\ n - m; & \text{for any mode } (m \neq 0) \end{cases}'$$

h_n is the axial wavenumber of the spatial harmonics, and $-\bar{h} < h_z < \bar{h}$ is the axial wavenumber of the fundamental branch. It is a general property of the spatially periodic SWS that the frequency is a periodic function of the wavenumber with period $\bar{h}$: $\omega(h_n) = \omega(h_z + n'\bar{h})$ for any integer *n'*. The E_z field in a periodic structure is a superposition of the spatial harmonics of the waves. These waves have different spatial structures, transverse distributions, wavenumbers (h_n), wavelengths ($\lambda_n = 2\pi/h_n$), and phase velocities ($v_{\phi,n} = \omega/h_n$). Even though the field of each harmonic satisfies Maxwell's equations but not the boundary conditions, the total field satisfies the boundary condition. Among these waves there is one wave whose phase velocity is close to the electron beam velocity which is a resonant wave. The reminder of the field is a sum of asynchronous and nonpropagating waves.

The sine and cosine functions in (2 – 13) represent standing waves that can be replaced by a complex exponential function to represent traveling waves in the azimuthal direction of the spiral corrugated structure.

The closed nature of the helical waveguide, together with the existence of a distinct groove region, requires a different mathematical approach from the axisymmetric structure and results in considerably modified propagation properties. Usual approximate analyses for axisymmetric SWSs assumes the propagation of the 1owest transverse magnetic slow wave mode only, i.e., the circularly symmetric TM_{01} mode [18-20, 44]. Thus, these SWSs are open-boundary structures (i.e., structures having one or more transverse field dimensions extending to infinity) and to analyze the problem the axial electric field component is sufficient. On the other hand, the helically corrugated waveguide is a closed-boundary structure and because of its skew boundary conditions, it is necessary to analyze the problem by using both transverse magnetic modes and transverse electric modes in complete sets [47]. Indeed, the waves are hybrid modes, and since both the axial component of the electric and magnetic field exist, the analysis must include them (Eq. (2 – 8) and (2 – 9)). Here, we assume no coupling between the modes (eigenmode coupling will be introduced in Sec. 2.2.1) and the field polarization in helical waveguides are rotating.

Having solved Maxwell's equations for the corrugation and center regions the fields are then matched at the common boundary, enabling the propagation equation to be found. According to [47, 48], the dispersion relation for a spiral SWS can be written as

$$D(\omega, h_n) = \left[\frac{J_m(kR_{max})\, Y'_m(kR_{min}) - Y_m(kR_{max}) J'_m(kR_{min})}{J_m(kR_{max}) Y_m(kR_{min}) - Y_m(kR_{max}) J_m(kR_{min})}\right]$$

$$+ \frac{s}{d} \sum_{n=-\infty}^{\infty} \frac{k\, R_{min}}{k_{\perp n} R_{min}} \left[\frac{J'_m(k_{\perp n} R_{min})}{J_m(k_{\perp n} R_{min})}\right.$$

$$\left. - \frac{(m h_n / R_{min} + k_{\perp n}^2 \tan\psi)^2}{k^2\, k_{\perp n}^2} \frac{J_m(k_{\perp n} R_{min})}{J'_m(k_{\perp n} R_{min})}\right] \times \left[\frac{\sin h_n s/2}{h_n s/2}\right]^2, \quad (2-14)$$

where $J'_m(x)$ and $Y'_m(x)$ are the derivative of the Bessel and Neumann functions (or the Bessel function of the first and second kind) of order *m* with respect to the radial coordinate.

This dispersion relation equation was derived by assuming that the corrugation depth is shallow ($r_1 = \frac{R_{max} - R_{min}}{2} \ll \lambda$), the pitch angle is small ($\tan^2\psi << 1$), no variations of longitudinal component of the electric field, and neglecting the higher order modes in the groove region. Even though this equation was derived for a rectangular corrugation of a circular waveguide, it can be used for a circular waveguide with sinusoidal corrugation. It was experimentally proven [49,50] that the rectangular corrugation has slightly less dispersion than the sinusoidal profile and the passband is a little smaller for the rectangular corrugation. From (2 – 14), the dispersion relation can be written for the TE_{11}, TM_{11}, HE_{11}, and EH_{11} modes [47,51] as

$$D(\omega, h_n) = \left[\frac{J_1(kR_{max})\, Y_1'(kR_{min}) - Y_1(kR_{max}) J_1'(kR_{min})}{J_1(kR_{max}) Y_1(kR_{min}) - Y_1(kR_{max}) J_1(kR_{min})}\right]$$

$$+ \frac{s}{d} \sum_{n=-\infty}^{\infty} \frac{k\, R_{min}}{k_{\perp n} R_{min}} \left[\frac{J_1'(k_{\perp n} R_{min})}{J_1(k_{\perp n} R_{min})}\right.$$

$$\left. - \frac{(h_n/R_{min} + k_{\perp n}^2 \tan\psi)^2}{k^2\, k_{\perp n}^2} \frac{J_1(k_{\perp n} R_{min})}{J_1'(k_{\perp n} R_{min})}\right] \times \left[\frac{\sin h_n s/2}{h_n s/2}\right]^2 = 0. \quad (2-15)$$

The mode in our spiral SWS is either an EH_{11} or HE_{11} mode. The dispersion relation was examined for a fixed outer radius of the corrugation and for a phase change per period from 0 to π. As the inner radius decreases, the dominate mode is the TM_{11} (E_{11}) mode. Therefore, the mode exhibits a backward-wave characteristic of the EH_{11} mode. On the other hand, as the inner radius increases, the dominate mode is the TE_{11} (H_{11}) mode in which the mode exhibits a forward-wave characteristics of the HE_{11} mode [51].

For azimuthally symmetric waves, the dispersion relation can be found from (2 – 14) by letting $m = 0$ and $\psi = 0$ [47, 52] as

$$D(\omega, h_n) = \left[\frac{J_0(kR_{max})\, Y_0'(kR_{min}) - Y_0(kR_{max}) J_0'(kR_{min})}{J_0(kR_{max}) Y_0(kR_{min}) - Y_0(kR_{max}) J_0(kR_{min})}\right]$$

$$+ \frac{s}{d} \sum_{n=-\infty}^{\infty} \frac{k\, R_{min}}{k_{\perp n} R_{min}} \left[\frac{J_0'(k_{\perp n} R_{min})}{J_0(k_{\perp n} R_{min})}\right] \times \left[\frac{\sin h_n s/2}{h_n s/2}\right]^2 = 0. \quad (2-16)$$

In fact, Walkinshaw derived this dispersion relation with fields averaged over the corrugation cross section (mouth) [52]. Thus, the term $\left[\frac{\sin h_n s/2}{h_n s/2}\right]^2$ in (2 – 16) was replaced by $\left[\frac{\sin h_n s/2}{h_n s/2}\right] J_0\left(\frac{h_n s}{2}\right)$.

In order to ensure the continuity of fields between the two regions and to minimize computation time, the angular dependence of a mode (m) is always considered the fundamental branch ($m = n$) of the dispersion curve [53,54]. This is acceptable since the dispersion curve is periodic and the other spatial harmonics are basically the same as the fundamental branch. In addition, when the depth of corrugation approaches zero, the fundamental spatial harmonic is continuously transformed into a TM or TE mode of ordinary waveguide. The summation of the spatial harmonics in (2 – 14) confirms that the term with $m = n$ is always the fast-wave term with the highest phase velocity and the largest amplitude, whereas terms with $m \neq n$ are all slow wave spatial harmonics. For slow waves, the argument of the Bessel function in (2 – 14) becomes imaginary and the Bessel functions are replaced by the modified Bessel functions ($J_m(ix) = (i)^m I_m(x)$, $J_m'(ix) = -i\,(i)^m I_m'(x)$, $Y_m(ix) = (i)^m K_m(x)$, and $Y_m'(ix) = -i\,(i)^m K_m'(x)$).

Before proceeding to the hot dispersion relation, another important parameter, which is the coupling impedance, should be introduced. Even though the coupling impedance is a measure of the coupling between the electron beam and the eigenmode of the SWS, it can be found from a cold SWS treatment. At the SWS radius, the coupling impedance can be written as

$$Z_n = \frac{E_{zn}^2}{2\,h_n^2 P_n} \approx \frac{|\int_0^d dz\, E_z\,|^2}{2\,h_z^2 \int_0^d dz \int_0^{r_w} dr\, \frac{2\pi r}{d}\{|E|^2 + |B|^2\}}, \qquad (2-17)$$

where P_n is the total power inside the SWS, which is the integration of the Poynting vector of a certain spatial harmonic of the SWS cross-section area.

2.1.1.3. Relativistic Electron Beam and Eigenmode Interactions in BWOs

Microwaves are generated in a BWO as a result of the energy transfer from drifting electrons to the normal electromagnetic modes of a cylindrical rippled wall waveguide. As the electron beam streams inside a SWS, the fields perturb, modulate, bunch, and then decelerate the electrons. That occurs when the dispersion curve of an eigenmode, which was introduced in Sec. 2.1.1.2, intersects with the dispersion line of the electron beam. The dispersion relation for the electron beam can be written as

$$\omega = h_n * v_0. \qquad (2-18)$$

Since the electrons bunch and repel one another other, they oscillate at the electrons' plasma frequency. The plasma frequency splits the electron beam line (2 – 18) into two space-charge waves, a fast space-charge wave increased by the electrons plasma frequency and a slow space-charge wave decreased by the plasma frequency. In fact, instability occurs, in the electron beam, where the dispersion curve of the structure eigenmode and the slower space-charge wave intersect ($v_0 \approx v_\phi$). Near resonance, the transverse wavenumber is imaginary and from (2 – 18) it becomes

$$k_\perp^2 \approx \left(\frac{\omega^2}{c^2} - \frac{\omega^2}{v_0^2}\right) = \frac{-\omega^2}{v_0^2\,\gamma_0^2}. \qquad (2-19)$$

Analytical methods were developed in order to obtain a more exact determination of the frequency characteristics of the SWSs and to calculate the linear growth rates for the instability which leads to the development of microwave oscillations.

For uniform SWS, Floquet's theorem can be applied; however, for nonuniform SWSs it cannot be used. A model based on nonlinear theory [19,55] was developed for

nonuniform SWS analysis. A set of self-consistent equations relate the steady state energy exchange between the electrons and the eigenmodes. The equations describe the changes in the electric field, the kinetic energy of the electrons, and the phase of the electrons as a function of distance traveled in the SWS.

For a uniform SWS, two theoretical models based on relativistic field theory were considered [41,56,57] to model a uniform SWS. The structure of the first model is assumed to be axisymmetric and supports only symmetric transverse magnetic modes of a circular waveguide. The electron beam is subject to the influence of two waves, the -1st spatial harmonic of the backward wave, which extracts energy from the electron beam, and the fundamental (0th) harmonic of the fast forward wave. The second model is valid for arbitrary azimuthal mode number and has been adapted for studying helical waveguides. The -2nd harmonic of the HE_{11} mode extracts the energy of the electron beam while the forward wave is the 1st spatial harmonic. In both models, it is assumed that a monoenergetic and infinitesimally thin annular electron beam is streaming in the interaction region.

A. Axisymmetric SWS Normal Modes with an Electron Beam

This approach is based on the linear fluid model [41]. To model the system theoretically, additional assumptions were made, such as

1- The system is infinitely long.

2- The system has azimuthal symmetry (i.e., $\frac{\partial}{\partial \phi} = 0$).

3- The axial magnetic field guiding the electron beam is infinitely strong. Thus, beam rotation is negligible and velocity perturbation is along the axial direction.

4- Small-amplitude signals only.

5- The transverse electric modes do not perturb electron motion.

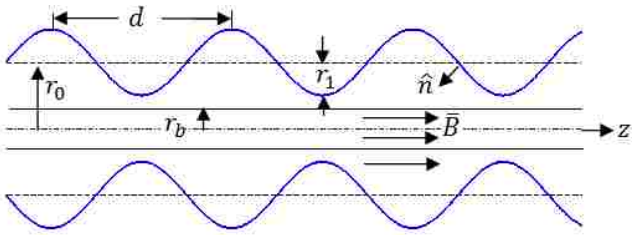

Figure 2.6 Model of the sinusoidal rippled wall SWS and the electron beam.

Since the electron beam is streaming very close to the SWS, the groove region is extended to the electron beam radius instead of the inner radius of the corrugation for the hot dispersion relation derivation. This means two regions were considered: from the center of the SWS to the electron beam and from the electron beam to the corrugation profile. Considering the spatial harmonics of the axial electric field E_z, the solution of (2 – 8) is a Bessel function (2 – 13) and can be written for $E_{zn}(r)$ as

$$E_{zn} = \begin{cases} A_{1n} J_0(k_{\perp n} r), & 0 < r < r_b \\ A_{2n} J_0(k_{\perp n} r) + A_{3n} Y_0(k_{\perp n} r), & r_b < r < r_w \end{cases}, \qquad (2-20)$$

where A_1, A_2, and A_3 are constants, r_b and r_w are the radius of the electron beam, and the SWS wall, respectively. By matching the boundary conditions at the electron beam and considering the fact that the electric field vector tangential to the corrugated wall is $\hat{n} = \hat{r}(dr_w/dz) + \hat{z}$, the dispersion relation was derived [41] and can be written as

$$\det[\boldsymbol{D}(\omega, h_z)] = 0, \qquad (2-21)$$

where $\boldsymbol{D}$ is a matrix with elements D_{ln}, which can be found by

$$D_{ln} = \left(\frac{\omega^2 - h_n h_l c^2}{k_{\perp n}^2 c^2}\right)\left[I_{0ln} - \alpha\left(\frac{c\, k_{\perp n}}{\omega - h_n v_0}\right)^2\right.$$

$$\left.\times \bar{h}\; J_0(k_{\perp n} r_b)\,[I_{0ln}\, Y_0(k_{\perp n} r_b) - K_{0ln}\, J_0(k_{\perp n} r_b)]\right]. \qquad (2-22)$$

Here α is the space-charge factor, given by

$$\alpha = \frac{\pi I_b}{\beta_0\, \gamma_0^3\, I_A}, \qquad (2-23)$$

where I_b is the electron beam current and $I_A = m_0c^3/e$ is the Alfvén current of approximately 17 kA. The terms I_{0ln} and K_{0ln} are the Fourier integrals of the Bessel functions of the first- and second-kind (J_0 and Y_0 for fast-wave), or modified Bessel functions (I_0 and K_0 for slow wave) of order zero, which are defined by

$$I_{0ln} = \int_{-\pi}^{\pi} e^{i\bar{h}(n-l)z}\; J_0\left[k_{\perp n}\, r_w\left(\bar{h}\, z\right)\right]dz, \qquad (2-24)$$

$$K_{0ln} = \int_{-\pi}^{\pi} e^{i\bar{h}(n-l)z}\; Y_0\left[k_{\perp n}\, r_w\left(\bar{h}\, z\right)\right]dz. \qquad (2-25)$$

The dispersion relation can be found from the determinant of the ***D*** matrix. Although the equation involves an infinite matrix in principle, in practice, truncating the ***D*** matrix to some smaller size is usually the common method of its solution [41].

The purpose of the reminder of the section is to show that the dispersion relation (2 – 22) can be approximated by a Pierce-type dispersion relation, thereby allowing us to gain a better understanding of the interaction process. Following Chen [58], we write (2 – 22) as

$$D_{ln}(\omega, h_z) = D_{ln}^{(0)}(\omega, h_z)\left[D_{ln}^{(sc)}(\omega, h_z) - \frac{\alpha F_{ln}(\omega, h_z)}{(\omega - h_n\, v_0)^2}\right], \qquad (2-26)$$

where the elements of the cold dispersion relation matrix $\boldsymbol{D}^{(0)}(\omega, h_n)$ are defined by

$$D_{ln}^{(0)}(\omega, h_z) = \frac{I_{0ln}}{k_{\perp n}^2}\left(h_n h_l - \frac{\omega^2}{c^2}\right), \qquad (2-27)$$

and

$$D_{ln}^{(sc)}(\omega, h_z) = 1 - \alpha\, I_0^2(k_{\perp n} r_b)\left(\frac{K_0(k_{\perp n} r_b)}{I_0(k_{\perp n} r_b)} - \frac{K_0(k_{\perp n} r_0)}{I_0(k_{\perp n} r_0)}\right)\frac{c^2 k_{\perp n}^2}{(\omega - h_n v_0)^2}, \qquad (2-28)$$

which is the dielectric function describing both the fast- and slow space-charge waves of the n[th] spatial harmonic on the electron beam streaming through a waveguide of average radius r_0. The function

$$F_{ln}(\omega, h_z) = c^2 k_{\perp n}^2\, I_0^2(k_{\perp n}\, r_b)\left(\frac{K_0(k_{\perp n}\, r_0)}{I_0(k_{\perp n}\, r_0)} - \frac{K_{0ln}}{I_{0ln}}\right) \qquad (2-29)$$

is related to Pierce's parameter.

The Pierce-type dispersion relation describes the linear coupling of the relativistic electron beam with SWS eigenmodes. By further simplifying, the dispersion relation can be expressed in the same form as Pierce's dispersion relation, i.e.,

$$\left[\Delta\omega_0 - v_g(\Delta h_c)\right]\left[(\omega - h_n\, v_0)^2 - Q_n\right] = C_n^3, \qquad (2-30)$$

where $\Delta\omega_0 = \omega - \omega_0$ and $\Delta h_c = h_z - h_c$ are the values at the intersection of a structural wave and the n[th] harmonic of the space-charge wave in the dispersion diagram and

$$v_g = -\left(\frac{\partial \det D^{(0)}}{\partial h_z} \Big/ \frac{\partial \det D^{(0)}}{\partial \omega}\right)_{\omega=\omega_0,\, h_z = h_c}, \qquad (2-31)$$

is the group velocity of the structural wave. In addition, the space-charge parameter is defined through

$$Q_n = \alpha\, c^2 k_{\perp n}^2\, I_0^2(k_{\perp n}\, r_b)\left(\frac{K_0(k_{\perp n}\, r_b)}{I_0(k_{\perp n}\, r_b)} - \frac{K_0(k_{\perp n}\, r_0)}{I_0(k_{\perp n}\, r_0)}\right), \qquad (2-32)$$

and the Pierce's parameter C_n is defined by

$$C_n^3 = \alpha \left(\frac{\partial \det D^{(0)}}{\partial \omega}\right)^{-1}_{\omega=\omega_0\,, h_z = h_c} \times \sum_{l=-\infty}^{\infty} adj\,(D^{(0)})_{ln}\;\; D_{ln}^{(0)}\, F_{ln}\,; \qquad (2-33)$$

Here $\det D^{(0)}$ and $adj\,(D^{(0)})_{ln}$ are the determinant and adjugate (or adjoint) of the matrix $\boldsymbol{D}^{(0)}(\omega, h_z)$.

B. Spiral Corrugated SWS Modes

Deriving the hot dispersion relation of asymmetric modes propagating inside a helically corrugated waveguide is more complicated than deriving the dispersion relation for axisymmetric SWSs. For this purpose, a fully self-consistent and relativistic field theory of the SWS was developed by solution of the relativistic fluid equations and Maxwell's equations [56,57]. Even though this approach was derived for a helix TWT with infinitesimal thicknesses, it can be expanded to include a helical corrugated waveguide.

The region inside the SWS is divided into three regions: the region within the beam, the region between the beam and the inner radius, and the region between the inner and the outer radii. Thus, the wave equation solutions for the axial electric and magnetic fields in the three regions are of the form

$$\left.\begin{matrix} E_z(r) \\ H_z(r) \end{matrix}\right\} = \begin{cases} A_1 J_m(k_\perp r), & 0 < r < r_b \\ A_2 J_m(k_\perp r) + A_3 Y_m(k_\perp r), & r_b < r < R_{min} \\ A_4 J_m(k_\perp r) + A_5 Y_m(k_\perp r), & R_{min} < r < R_{max} \end{cases} . \quad (2-34)$$

Note that the solution of the wave equation was written for the fundamental branch ($m = n$) of the spatial harmonic alone ($h_n = h_z$). Application of the boundary conditions permits the elimination of unknown coefficients and the derivation of the dispersion relation which governs the dispersion of the wave. From Freund [57], the dispersion relation for a helix-loaded waveguide interacting with an electron beam is given by

$$D_m^{(0)}(\omega, h_z)\, D_m^{(sc)}(\omega, h_z) = CF_m, \quad (2-35)$$

where

$$D_m^{(0)}(\omega, h_z) = \frac{\omega^2}{c^2} + k_\perp^2 \left(\frac{m h_z}{k_\perp^2 R_{min}} - \tan\psi\right)^2 \frac{J_m(k_\perp R_{min})\, J_m'(k_\perp R_{max})}{J_m(k_\perp R_{max}) J_m'(k_\perp R_{min})} \times \frac{W_m(R_{max}, R_{min})}{W_m''(R_{max}, R_{min})}, \quad (2-36)$$

$$D_m^{(sc)}(\omega, h_z) = \frac{(\omega - h_z v_0)^2}{c^2} - \frac{\omega_p^2\, (2\pi r_b \Delta r_b)}{4\, \gamma_0^3 c^2}\, k_\perp^2\, \frac{J_m(k_\perp r_b) W_m(r_b, R_{max})}{J_m(k_\perp R_{min})}, \quad (2-37)$$

$$CF_m = -\frac{\omega_p^2\, (2\pi r_b \Delta r_b)}{4\, \gamma_0^3 c^2}\, \frac{\omega^2}{c^2}\, k_\perp^2\, \frac{J_m^2(k_\perp r_b)}{J_m(k_\perp R_{max}) J_m(k_\perp R_{min})}\, W_m(R_{max}, R_{min}), \quad (2-38)$$

and

$$W_m(R_1, R_2) = Y_m(k_\perp R_1) J_m(k_\perp R_2) - J_m(k_\perp R_1) Y_m(k_\perp R_2)$$

$$W_m'(R_1, R_2) = Y_m'(k_\perp R_1) J_m(k_\perp R_2) - J_m'(k_\perp R_1) Y_m(k_\perp R_2)$$

$$W_m''(R_1, R_2) = Y_m'(k_\perp R_1) J_m'(k_\perp R_2) - J_m'(k_\perp R_1) Y_m'(k_\perp R_2).$$

Even though the annular beam was considered very thin, the beam thickness (Δr_b) was included in the dispersion relation. CF_m can be considered the coupling coefficient

between the cold dispersion relation and the electron beam dispersion relation. $D^{(sc)}$ denotes the dielectric function for the beam space-charge modes. As such, the dispersion relation for the beam space-charge modes can be obtained from a purely electrostatic analysis (i.e., solution of Poisson's equation) for the beam in the SWS. Note that this dispersion relation (2 – 35) is valid for arbitrary azimuthal mode numbers for both forward and backward propagating waves.

The dispersion relation was solved for the azimuthally symmetric wave and the coupling wave Pierce theory is recovered in the near-resonant limit [57]. Indeed, the complete field theory is more exact, while the coupled-wave theory has greater physical insight into the interaction. The connection between these two approaches is found by noting that the coupled-wave theory can be obtained from the field theory in the near-resonant limit in which the phase velocity of the mode is close to the axial velocity of the electron beam ($c\,\beta_0 \approx v_0 \approx v_\varphi$). For $TM_{0\rho}$ modes, the Pierce parameters can be extracted from (2 – 35) as

$$C_n^3 = \frac{\omega_p^2\,(2\pi r_b \Delta r_b)}{8\,\gamma_0^5 c^2}\,\cot^2\psi\;\frac{J_0^2(k_\perp r_b)J_1(k_\perp R_{min})}{J_0^2(k_\perp R_{min})J_1(k_\perp R_{max})}\,W_0''(R_{min},R_{max}), \quad (2-39)$$

$$Q_n = \frac{\tan^2\psi}{2\beta_0^2}\;\frac{J_0(k_\perp R_{min})\,J_1(k_\perp R_{max})}{J_0(k_\perp r_b)J_1(k_\perp R_{min})}\;\frac{W_0(R_{min},r_b)}{W_0''(R_{min},R_{max})}. \quad (2-40)$$

Using these parameters, we can express the dispersion relation as

$$\left((\frac{\omega}{v_0})^2 - h_z^2\right)\left[\left(\frac{\omega}{v_0} - h_z\right)^2 - 4\,Q_n\,C_n^3\,h_z^2\right] \cong -2\,C_n^3(\frac{\omega}{v_0})\,h_z^3. \quad (2-41)$$

At resonance, if we now observe that $k_\perp$ has an imaginary value, then the Q_n and C_n parameters can be cast in terms of the modified Bessel functions by replacing the Bessel functions in (2 – 39) and (2 – 40).

Finally, one can show two relatively simple limiting case that are termed the Compton (ballistic) and Raman (space-charge dominated) regimes [31]. In the Compton regime of operation, the linear instability leading to microwave generation is the result of a three-wave process involving the two space-charge waves on the beam and a normal mode of the SWS. On the other hand, the resonant interaction that leads to instability is a two-wave process in the Raman regime [59].

In conclusion, the theory of SWSs reduces to solving the Maxwell equations with periodic boundary conditions. The problem is sufficiently complicated due to complex boundary conditions. A number of computational methods have been proposed and the final results are usually developed numerically. HFSS was used to determine the cold dispersion relations while the MAGIC PIC code was used to estimate the hot test results.

C. RBWO Asymptotic Theory (or Self-Consistent Nonlinear Equations)

This approach was developed by Kovalev [19] based on a simple approximation of one-dimensional ultrarelativistic electron motion in a high frequency field derived by Petelin [60]. The self-consistent equations show how the relative bunching of the electrons relate to the electric field within the structure. This approach is a simple analysis of the phase relationship between the electrons and the eigenmodes, and was developed to demonstrate how a BWO operates, regardless of the SWS profile. For a

nonuniform SWS ($d(z)$; $\bar{h}(z) = 2\pi/d(z)$), many of the assumptions that were made for uniform SWS models are not valid. The expansion of the electric fields using Floquet's theorem and an infinite DC magnetic field cannot be assumed.

In fact, there are many factors that influence the operation of a BWO, such as coupling between the electron beam and the different modes, the space-charge effects of the beam, and the end reflections of the waves. Thus, a set of self-consistent equations that relate the steady state energy exchange between the electron beam and the electromagnetic waves excited by the beam was developed. Some simplifications were assumed to formulate the self-consistent system of equations as follows:

1- The single-frequency mode of steady-state oscillation in a one-dimensional model was considered.
2- The space-charge field and the field of the radiation opposite to the operating wave are assumed to be negligibly small.
3- There is no attenuation in the electrodynamic system.
4- Both the collector and the cathode ends are perfectly matched.
5- The spread in the electron velocities is ignored.
6- The electron energy is assumed to be ultrarelativistic.

The nonlinear equations comprise three equations which describe the changes in the dimensionless electric field amplitude (A_z), kinetic energy of the electrons (W), and phase of the electrons (θ) as a function of the dimensionless SWS length (ξ). If the electron energy E remains ultrarelativistic through all interaction processes ($E >> mc^2$), the motion

of electrons can be described with universal equations valid for any initial electron energy $E_0 = \gamma_0 mc^2$ via

$$\frac{dW(\xi)}{d\xi} = Re\left\{\left(A_z + i\,Q_n \int_0^{2\pi} e^{-i\theta} d\theta_0\right) e^{i\theta}\right\};\ W(0) = 1, \qquad (2-42)$$

$$\frac{d\theta(\xi)}{d\xi} = W^{-2} - \delta; \qquad \theta(0) = \theta_0\ \epsilon[0,2\pi), \qquad (2-43)$$

which have to be complemented with the equation of wave excitation

$$\frac{dA_z(\xi)}{d\xi} = \pm C_n \int_0^{2\pi} e^{-i\theta} d\theta_0\,; \quad A_z(L) = 0. \qquad (2-44)$$

Here, $W = \frac{\gamma}{\gamma_0}$ is the normalized electron energy, $\xi = \frac{kz}{2\gamma_0^2}$ is a dimensionless longitudinal coordinate, $\theta = \omega t - h_n z$ is the phase of electrons with respect to the electromagnetic wave, $A_z = \frac{2c\gamma_0}{k\,I_A} E_{zn}$ is a value proportional to the axial electric field, and $\delta = 2\gamma_0^2 (\frac{h_n}{k} - 1)$ is the initial synchronism mismatch. Q_n is a space-charge parameter given by (2 – 40) for an annular beam in a smooth wall waveguide and $C_n^3 = \frac{4c\,\gamma_0^3\,I_b}{I_A} Z_n$ is the coupling coefficient. By solving the nonlinear boundary-value problem of the above equations, the energy exchange efficiency can be written as

$$\eta = \frac{C_n}{2\pi} \left(\frac{\gamma_0+1}{\gamma_0}\right) \int_0^{2\pi} W d\theta_0. \qquad (2-45)$$

The optimum efficiency is $\eta \approx 0.19\ (\frac{\gamma_0+1}{\gamma_0})$ and the optimum device length is $\xi \approx 1.97$ when $C_n^3 \approx 2\pi$.

2.1.1.4. Oscillation Start Condition

BWOs generate microwaves from noise when the start oscillation conditions are satisfied. The start current for spontaneous growth of oscillations, as well as the optimum length for maximum efficiency, depend on the beam energy and the SWS geometry. The start oscillation conditions are obtained from the solution of the linearized system of the self-consistent equations. The dimensionless starting length of a BWO is

$$\xi_{st} = C_n \frac{kL_{st}}{2\gamma_0^2} \; ; \; L_{st} \leq \frac{\lambda}{\left|\frac{c}{v_0} - \frac{c}{v_\varphi}\right|}, \qquad (2-46)$$

where L_{st} is the starting length of the interaction region and $1.07 \leq \xi_{st}(\frac{C_n^3}{2\pi})^{1/2} \leq 2$.

Another important starting parameter is the starting energy, below which oscillation could not occur. The starting beam energy, which decreases by increasing the SWS length, was first discussed by Minami for an overmoded SWS and finite length RBWO [61]. For a finite length SWS, the end reflections lead to standing waves. The external Q value (quality factor) of the SWS resonator must be sufficiently large for oscillations to occur. In addition, the resonator must store a minimum amount of microwave energy for oscillations.

The calculation of the start current is quite complicated, and its derivation is beyond the scope of our work. There are many publications that deal with the start current calculation with some specific conditions, such as considering reflections from the ends ($\Gamma_z e^{i\emptyset_z}$), or considering a low beam current with an infinite magnetic field. Based on the Kovalev asymptotic model [19,62,63], the start current is given by

$$I_{start} = I_A \frac{(\gamma_0^2 - 1)^{3/2}}{4\pi^3 c Z_n} (\frac{\lambda}{L} \xi_{st})^3. \qquad (2-47)$$

The coupling impedance can be approximated from (2 – 17) and from Kovalev's theory as [64]

$$Z_n \approx \begin{cases} (\frac{r_1}{r_0})^2 \frac{(k_{\perp m}^2 + h_z \bar{h}\ )^2}{h_n^2 h_z ck} \frac{I_n^2(k_{\perp n} r_b)}{I_n^2(k_{\perp n} r_0)}; & \text{for } \mathrm{TM_{m\rho}} \text{ waves} \\ (\frac{r_1}{r_0})^2 \frac{n^2 \bar{h}^2 k^2}{h_n^2 h_z c (k_{\perp m}^2 r_0^2 - n^2)} \frac{I_n^2(k_{\perp n} r_b)}{I_n^2(k_{\perp n} r_0)}; & \text{for } \mathrm{TE_{m\rho}} \text{ waves} \end{cases}. \qquad (2-48)$$

The end reflections and finite length SWS considerations were discussed and included in [65]. The start current for a finite length SWS is given as

$$I_{start} = \frac{I_A}{8\pi N^3} \frac{\gamma_0^3 \beta_0^2}{h_c^2 d} \frac{v_g}{Z_n} \widetilde{\Gamma_{st}}, \qquad (2-49)$$

where

$$\widetilde{\Gamma_{st}} = \begin{cases} 7.7; & \text{with no end reflections} \\ \sim \Gamma_0 \Gamma_l e^{i\emptyset_0} e^{i\emptyset_l}; & \text{with end reflections'} \end{cases}$$

and

$$\gamma_0 = \gamma - \Delta\gamma;\ \gamma = 1 + \frac{|eV_c|}{m_0 c^2},$$

Here, $\Delta\gamma$ is related to the electron beam DC space-charge effect, also known as voltage depression (2 – 4). This effect is due to an electrostatic potential inside the waveguide that will reduce the beam energy. Also, I_A = 17 kA is the Alfvén current, and V_c is the applied voltage (A-K gap voltage). The number of structure periods is $N=L/d$, h_c is the resonance wavenumber, v_g is the group velocity, and $\widetilde{\Gamma_{st}}$ is related to end reflections.

Since the BWO is a finite length system, there will be reflections of the microwaves at both ends of the SWS. The end reflection is important for BWO operation to provide feedback for oscillations.

The electric field that is generated in the SWS will cause the beam particles to become bunched. This causes the axial beam current to become temporally and spatially modulated. The beam bunching induces a space-charge electric field which is proportional to the beam density. These AC space-charge fields will introduce the so-called space-charge-limited current. The space-charge-limited current is the maximum steady state axial current that a metal waveguide allows. In order to find the space-charge-limited current, the beam current [41,45] is related to the cathode potential, the relativistic factor, and to the beam dimensions (geometry) through

$$I_b = \frac{I_A}{2\ \ln\left(\frac{r_0}{r_b}\right)} (\gamma_0^2 - 1)^{\frac{1}{2}} \frac{\gamma - \gamma_0}{\gamma_0}\,. \qquad (2-50)$$

The space-charge-limited current can be found at specific values of the relativistic factor [41] ($\gamma_0 = \gamma^{1/3}$) as

$$I_b = I_{scl} = \frac{I_A}{2\ \ln\left(\frac{r_0}{r_b}\right)} (\gamma_0^2 - 1)^{\frac{3}{2}}. \qquad (2-51)$$

This space-charge limit is due to the finite thickness of the electron beam and the metallic structure of the waveguide.

2.2. Bragg Structures

Waveguides with periodic perturbations (Bragg structures) have been intensively investigated for different applications in microwave electronics [27,66-68] and integrated optics [69], where similar structures are known as photonic band gap (PBG) structures. These studies have resulted in the appearance of new active [69] and passive devices [66]. The Bragg structures are most suitable to be used as narrowband filters and reflectors, mode converters, as components for pulse compression, or as a part of an interaction region to provide distributed feedback [70]. Furthermore, they are very effective in millimeter and sub-millimeter wave ranges.

In general, the physical phenomenon behind its operation is Bragg scattering. The effects of the mode transformation, band gap formation, diffraction compensation observed in the Bragg structures are due to resonant constructive and destructive interference of waves scattered on periodic perturbations, which takes place in the vicinity of the Bragg resonance. The parameters of the frequency band where the effective scattering and wave interference takes place can be manipulated by varying the period and the amplitude of the perturbations [68].

The general structure of the Bragg reflector can take several geometries. A planar, a waveguide with shallow sinusoidal or rectangular corrugations, coaxial Bragg structures have been investigated [71]. In this work, a cylindrical waveguide with a sinusoidal corrugation was designed and manufactured as a Bragg reflector for HPM wave reflection and conversion. Generally, the Bragg structure can be designed using a periodic SWS with zero and nonzero azimuthal index dependence upon the two coupled

modes. These structures exhibit so-called stop-band phenomena leading to frequency selective scattering. A stop-band appears at a chosen frequency when the period of the SWS is one wavelength. At a wavelength outside the band gap the scattered waves are out of phase and cancel on another in one direction and add up in the other direction.

2.2.1. Spiral Corrugated Cylindrical Structure Mode Coupling

To ensure Gaussian mode operation of a RBWO, one must use an electromagnetic system providing selective reflection. In order to provide coupling coefficients between two waveguide modes, results of the linear analysis based on coupled-wave theory and perturbation theory [8,64,72-74] is presented in this Subsection. In fact, the coupled-wave theory has some different assumptions than the usual Brillouin theory of wave propagation in periodic structures [75]. It is necessary to introduce a system of two oppositely propagating waves inside a corrugated waveguide (2 – 1) to demonstrate the coupling between them. The two oppositely propagating waves $\boldsymbol{E_1}$ and $\boldsymbol{E_2}$ can be written as

$$E_1 = A_1(z)E_{z1}(r)\exp(i\omega t - i\bar{m}_1\varphi - ih_1 z), \qquad (2-52)$$

$$E_2 = A_2(z)E_{z2}(r)\exp(i\omega t - i\bar{m}_2\varphi + ih_2 z), \text{and} \qquad (2-53)$$

where A_1 and A_2 are the complex amplitude of the waves as a function of the axial direction, h_1 and h_2 are the axial wavenumbers, and $\bar{m}_1$ and $\bar{m}_2$ are the azimuthal variation of the oppositely propagating waves, respectively. Note that the subscripts *1* and *2* denote the two oppositely propagating waves, not the spatial harmonics of one wave. The corrugation parameters relate to the Bragg conditions through

$$\bar{h} \approx h_1 \pm h_2 \quad \text{and} \tag{2-54}$$

$$\bar{m} = \pm(\bar{m}_1 - \bar{m}_2), \tag{2-55}$$

where the plus sign of (2 – 54) is used when a reflector needs to be designed, while the minus sign is for a mode converter or a passive pulse compressor design. In addition, the minus or plus sign of (2 – 55) denotes a right- or left-handed helical corrugation, respectively.

When Eq. (2 – 54) and (2 – 55) are satisfied, a two-mode coupling will occur. For two oppositely propagating coupled waves, the dispersion relation for the corrugated waveguide with helical symmetry can be written as [66]

$$(k^2 - k_{\perp 1}^2 - h_1^2)(k^2 - k_{\perp 2}^2 - h_2^2) = 4\delta_{1,2}^2 k_0^2, \tag{2-56}$$

where $k_{\perp 1}$ and $k_{\perp 2}$ are wavenumbers corresponding to the cutoff frequencies of the modes, $\delta_{1,2}$ are the coupling coefficients of the two waves, , k_0 is the wavenumber of the exact Bragg resonance and $k = 2\pi/\lambda$. In addition, ($\Delta h = h_1 - h_2$) and ($\Delta k = k_{\perp 1} - k_{\perp 2}$) are the "geometrical" and frequency mismatches, respectively. There are no geometrical ($h_1 = h_2 = h$) or frequency mismatches if the coupling is between two identical modes or two modes with identical transverse mode structure ($k_{\perp 1} = k_{\perp 2} = k_{\perp}$). The Bragg frequency ($\omega_B$) in this case is

$$\omega_B = c\sqrt{\frac{h^2}{2} + k_{\perp}^2}. \tag{2-57}$$

Finally, the coupling coefficient inside a circular waveguide are given by [66]

$$\delta_{1,2} = \frac{r_1}{2\,r_0^3}\frac{-x_1^2 x_2^2 + \bar{m}_1\bar{m}_2 r_0^2\,(k^2 + h_1 h_2)}{\sqrt{h_1 h_2}\sqrt{(x_1^2 - \bar{m}_1^2)(x_2^2 - \bar{m}_2^2)}} \quad \text{for two TE} - \text{modes,} \qquad (2-58)$$

$$\delta_{1,2} = \frac{r_1}{2\,r_0}\frac{(k^2 + h_1 h_2)}{\sqrt{h_1 h_2}} \quad \text{for two TM} - \text{modes, and} \qquad (2-59)$$

$$\delta_{1,2} = \frac{r_1}{2r_0}\frac{k\bar{m}_1\bar{h}}{[h_1 h_2(x_1^2 - \bar{m}_1^2)]^{1/2}} \quad \text{for TE} - \text{TM modes,} \qquad (2-60)$$

where x_1 and x_2 are the zeroes of the Bessel function and its derivative ($x = r_0\,k_\perp$). Basically, the resonant coupling of two waves occurs between one of the waves and a spatial harmonic of the second wave, and their dispersion curves will intersect.

In general, the coupling coefficient can be found for modes for which their complex amplitudes are slowly varying $\delta << h_{1,2}$ and negligible Ohmic loss, when the coupled mode equations of $\boldsymbol{E_1}$ and $\boldsymbol{E_2}$ satisfy

$$\frac{\partial A_1}{\partial z} + i\,\Delta\bar{h}\,A_1 = -i\,\delta_{1,2}\,A_2 \qquad \text{and} \qquad (2-61)$$

$$\frac{\partial A_2}{\partial z} - i\,\Delta\bar{h}\,A_2 = i\,\delta_{2,1}\,A_1, \qquad (2-62)$$

where $\Delta\bar{h} = \left(\frac{1}{2}\right)(h_1 \pm h_2 - \bar{h})$ is the Bragg resonance mismatch and $|A_1|^2 h_1$, $|A_2|^2 h_2$ represent the power carried by these respective modes.

The corrugation couples only two selected waves if for all other combinations of waves the Bragg conditions are sufficiently disturbed. If the azimuthal coupling condition is satisfied for undesired combination of waves (parasitic waves, h_s), then their longitudinal mismatches must greatly exceed their coupling coefficients

$$\left|\bar{h} - \sqrt{h_1 h_2} - h_s\right| \gg \left|\delta_{1,2}\right|, \left|\delta_{1,s}\right|, \left|\delta_{2,s}\right| \qquad (2-63)$$

If the coupling coefficient is negligibly small, (2 – 56) splits into two equations as

$$(k^2 - k_{\perp 1}^2 - h_1^2) = 0 \text{ and } (k^2 - k_{\perp 2}^2 - h_2^2) = 0. \qquad (2-64)$$

These equations are describing the dispersion of uncoupled mode *1* and the first Floquet harmonic of mode *2* as in the smooth wall waveguide case. Since the corrugation amplitude is small compared to the wavelength ($r_1 << \lambda$), the smooth wall waveguide equations were used to design the Bragg structure. The coupling coefficient between a TE mode and a TM mode will be discussed in more detail when the Bragg reflector is introduced and designed.

CHAPTER 3. SINGLE BAND GAUSSIAN RADIATION FROM RBWO

In Chapter 3 we design and analyze a frequency tunable X-band high power BWO with a linearly polarized Gaussian radiation for radar applications. The Gaussian microwave beam is attractive for radar and other applications because its maximum energy density is concentrated on-axis. In addition, frequency tuning makes it difficult to determine such a radar's location for purpose of jamming, whereas change of the linear polarization direction gives information about a target's configuration.

A BWO is the most suitable oscillator for this purpose. The short feedback loop in a BWO provides for fast start of oscillations that is important for our experiments using the short pulse, high current electron accelerator SINUS-6 [76]. In order to avoid problems with mode selection, the lowest symmetrical TM_{01} mode is chosen as the operating mode. The operating wave is generated with a negative group velocity where it is traveling in a direction opposite (backward) to that of the electron beam streaming forward. In order to extract the radiation axially, placing either a cavity reflector or a cutoff neck at the cathode end [18,19] is widely used to reflect the generated TM_{01} mode in the forward direction. Then, a mode converter is used at the output to radiate a Gaussian pattern.

In this work, a two-spiral corrugated Bragg reflector (Fig. 3.1) on the upstream end (cathode end) of the BWO's structure is proposed instead of a cavity reflector to reflect the operating backward TM_{01} mode to a forward TE_{11} mode with linear polarization, as shown in Fig. 3.2 [77-79].

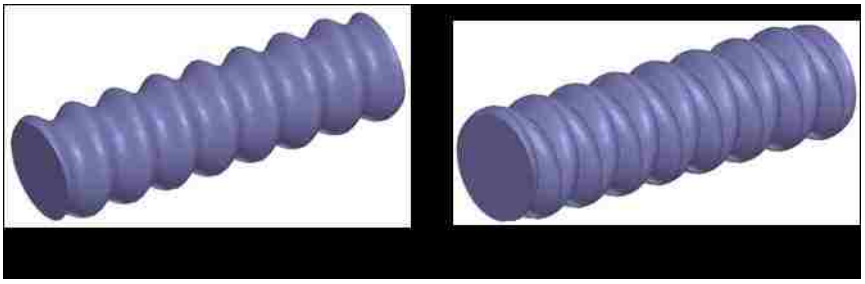

Figure 3.1 3-D view of (a) a single-fold left- or right-spiral corrugation (b) Bragg reflector.

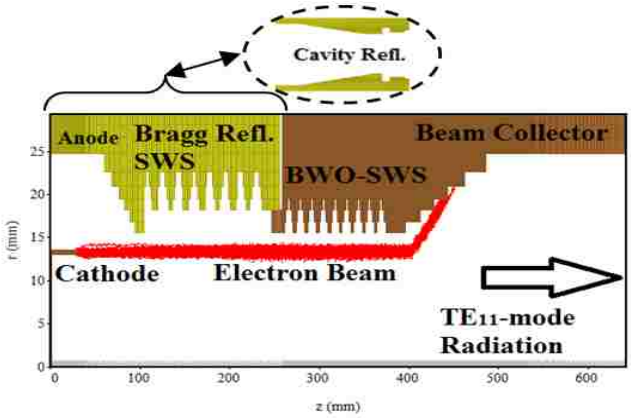

Figure 3.2 Design of the BWO with Bragg and cavity resonator reflector with a 1 mm gridding.

3.1. BWO with the Operating TM_{01} Mode

In order to achieve effective conversion of the TM_{01} mode to the TE_{11} mode, a pure operating TM_{01} mode must first be generated. For this purpose, a 460 kV X-band BWO, which was designed and investigated in [80], was used. Even though this designed BWO [81] has a cavity resonator-reflector at the cathode end (see Fig. 3.3), a cutoff section reflector can also be used. These reflectors act like a short-circuited transmission line at the cathode end of the interaction region that reflect the operating mode and preserves its field distribution. The cavity resonator reflector can only reflect azimuthally symmetric modes, while the cutoff neck can reflect any mode structure. The SWS of the BWO is a

circular waveguide with axisymmetric sinusoidal corrugation which can be described by (2 – 1) with $\bar{m} = 0$.

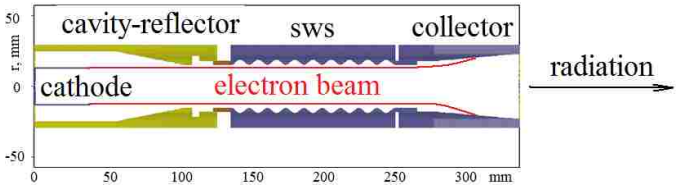

Figure 3.3 Design of the BWO with a cavity-reflector.

The dimensions of the SWS with 9 periods, the cathode, and the cavity resonator reflector are shown in Table 3-1. The cavity reflector is a pillbox cavity whose minimal radius (R_c) is the same as the minimal radius of the BWO's SWS, and the length of the cavity is L_c. The RBWO is an overmoded SWS with $2r_0/\lambda$ greater than 1. The increased cross section of the electrodynamic system not only decreases the probability of electrical breakdown, but also provides conditions for efficient operation of the device in the low magnetic field range (below the cyclotron resonance).

Table 3.1 BWO, cavity resonator reflector, and cathode dimensions.

Quantity	r_0	r_1	d	r_b	R_c	L_c
dimensions, (cm)	1.918	0.328	1.372	1.3	2.248	0.526

3.1.1. Mode Selection

A number of electromagnetic and electron methods of mode selection have been studied in RBWOs with overmoded SWSs up to a $2r_0/\lambda$ ratio of ~3 [35,74]. Electromagnetic selection of the TM_{01} mode has been achieved through variation of the

SWS parameters r_0, r_1, and d in order to increase frequency separation from the competing TM_{02} mode. The electron beam was also placed closer to the SWS in order to increase the coupling impedance, which is termed electron selection.

The electron beam radius (r_b) should be chosen to interact with the maximum electric field of the operating mode. For all TM modes (except the TM_{01} mode) and for TE modes the radius of the tubular electron beam can be chosen such that the intensity of cyclotron suppression for the operating mode is equal to zero (no cyclotron absorption), via

$$J_{m\pm1}^2\left(\frac{\chi_{m\rho}r_b}{r_0}\right) = 0. \qquad (3-1)$$

Here the ± signs correspond to the relative direction of rotation of the operating mode with respect to cyclotron rotation of electrons (m is -1 for the same direction of rotation and m is +1 for the opposite direction). In this case, there is no cyclotron interaction of electrons with this wave (this mode does not decay), whereas all other waves are suppressed. This is the principle of cyclotron mode selection.

3.1.2. Frequency Tunability

For conventional BWOs, changing the BWO oscillation frequency can be achieved by varying the electron energy; however, this mechanism is not effective in the substantially relativistic energy range.

For RBWOs with a cutoff neck reflector, shifting the reflector about the SWS was shown to tune the frequency by 4% for a uniform SWS and by 15% for a nonuniform

SWS [82,83]. Both studied devices operated with strong guide magnetic fields (well above the cyclotron resonance).

The cavity resonator serves not only as a reflector but as a prebuncher of the electron beam as well [84]. This facilitates mechanical frequency tuning by varying the distance between the reflector and the SWS end. This capability is due to preliminary modulation of the beam electrons by energy in the region of the resonant reflector. The energy modulation causes modulation of the velocity of the electrons and their inertial bunching. By varying the drift distance between the reflector and the corrugated SWS, one can vary the phase of the beam RF-current with respect to the RF field of the synchronous harmonic at the SWS input. The value of the phase affects the device starting length and, essentially, the starting synchronism mismatch and frequency. The mechanical frequency tuning, as well as by varying the amplitude of the guiding magnetic field [85], are shown in Fig. 3.4.

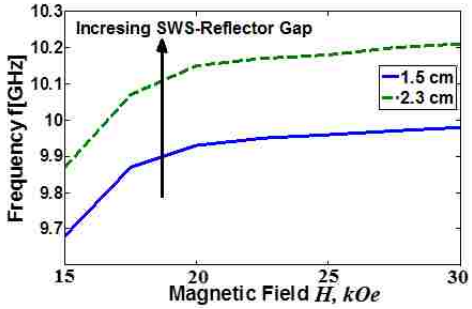

Figure 3.4 Dependence of the radiation frequency on the guide magnetic field when the gap distance between the cavity reflector and BWO-SWS end is 1.5 cm (lower curve) and 2.3 cm (upper curve).

The frequency of generation depends on the amplitude of the guide magnetic field near its resonant value H_0. Since this method of frequency tuning was used in this work, we will explain it in greater detail.

The frequency dependence on the external magnetic field *f(H)* is due to the decreasing longitudinal velocity v_0 of monoenergetic electrons. The decrease of the longitudinal velocity is caused by an increase in the transverse electron momentum [11-13]. When the value of the guide magnetic field approaches the resonant value (H_0), the fast cyclotron wave (ω_{H0}) of the electron beam resonates with the fundamental spatial harmonic of the operating wave as

$$\omega_{H_0} = \frac{eH_0}{mc\gamma_0} \approx \omega_0 + h_z v_0, \qquad (3-2)$$

where ω_0 is the cyclic frequency of the operating wave and h_z is the wavenumber of the fundamental (0^{th}) harmonic of the operating mode. Near the resonant value, a stop-band appears in spite of the absolute instability caused by the Cerenkov synchronism (Fig. 3.5); the synchronism is described by

$$\omega_0 \approx (\bar{h} - h_z)v_0. \qquad (3-3)$$

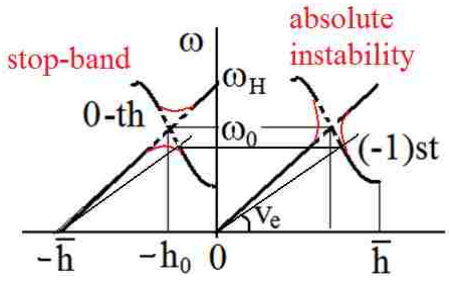

Figure 3.5 Graphs of conditions (3-2) and (3-3).

Basically, the cyclotron resonance of the fast cyclotron wave interacts with the fundamental (0^{th}) spatial harmonic of the axisymmetric operating wave, whereas the Cerenkov synchronism is the interaction of the slow space-charge wave with the negative first spatial harmonic. Therefore, the Cerenkov interaction occurs with the longitudinal

component of the electric field, whereas cyclotron interaction occurs with the transverse component. This leads to an increase of the transverse momentum (Fig. 3.6a) of electrons when the magnetic field H approaches the resonant value H_0. As a result, part of the electromagnetic energy is spent on electron rotation through the fundamental spatial harmonic of the wave. The lost energy leads to a mismatch in Cerenkov synchronism and an increase of the generation threshold. This terminates the generation (Fig. 3.6c), since the start current I_{st} exceeds the operating current, as shown in Fig. 3.6b. As a result, the region of cyclotron suppression of feedback (RCSF) appears.

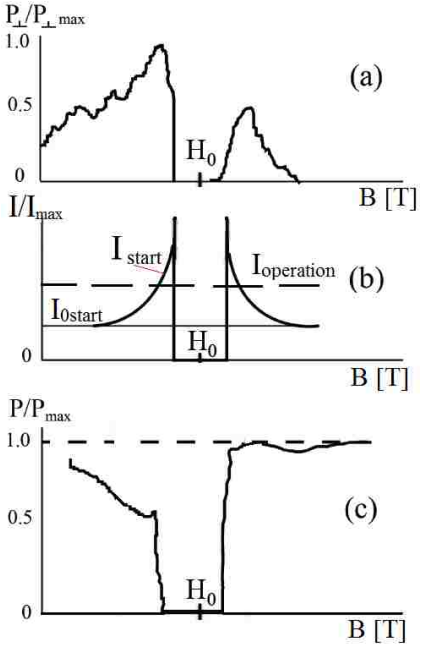

Figure 3.6 Illustration of the electrons transverse momentum (a), the start current (b), and the radiation power (c) dependence on the guide magnetic field near its resonant value (3-4).

A decrease in the velocity v_0 leads to a decrease in the resonant frequency. Thus, the cyclotron frequency can be written from (3 – 2) and (3 – 3) as

$$\omega_{H_0} \approx \bar{h} v_0. \qquad (3-4)$$

From the above discussion, frequency tuning can be achieved by controlling the magnitude of the guide magnetic field at the RCSF region. The frequency of oscillation increases when the value of the magnetic field approaches the RCSF region from weaker fields, whereas the frequency decreases when the magnetic field approaches the RCSF region from stronger fields.

In fact, the sign of the operating wave phase $\varphi \sim (\omega_H - \omega_0)t$ changes when the magnetic field passes through the resonance, which leads to a change in the frequency, $f = f_0 \pm d(\varphi)/dt$. In addition, the phase change effect can be explained by a change in the imaginary part of the conductivity and the effective permittivity of the interaction space, which are proportional to $\sim (\omega_H - \omega_0)$ [11,86]. This will lead to a change in the phase velocity of the operating wave, which in turn will change the frequency. The self-consistent theory of BWOs with cyclotron effects was given in [10,12].

3.2. Bragg Reflector as a TM_{01} - TE_{11} Mode Converter

In order to extract a Gaussian-like radiation pattern from the BWO described in Sec. 3.1, Fig. 3.3, and [80], the cavity-reflector on the "cathode" end of the BWO was replaced by a Bragg reflector. The cavity reflector and the cutoff neck reflect the operating TM_{01} mode and save its field structure, whereas the Bragg reflector reflects and transforms the field pattern of the operating mode.

The suggested Bragg reflector is basically a circular waveguide with periodic combined single-fold left- and right-spiral corrugations. One of the spiral corrugations converts the operating TM_{01} mode to the forward TE_{11} mode rotating in the clockwise direction, while

the other spiral converts the operating TM_{01} mode to the forward TE_{11} mode rotating in the counter-clockwise direction. Their sum forms a forward TE_{11} mode with linear polarization, as shown in Fig. 3.7. This version requires detailed investigation because electrons rotating around magnetic field lines can lead to asymmetry in the radiation of BWOs with opposite circular polarizations that results in a disruption of the linear polarization.

Figure 3.7 Formation of radiation with linear polarization.

Since the Bragg reflector is required to couple TM_{01} (m_{01} = 0, x_{01} = 2.4049) and TE_{11} (m_{11} = 1, x_{11} = 1.8412) modes at 10 GHz, the profile of the Bragg reflector must be a spiral corrugations profile described by (2 – 1) with $\bar{m} = \pm(m_{01} - m_{11}) = \pm 1$ to satisfy the Bragg conditions (Sec. 2.2.1). The period of the SWS must be comparable to the wavelength for Bragg scattering to occur while there is no design restriction for the depth of the SWS. Practically, the inner radius of the Bragg reflector must be larger than the electron beam (r_b = 1.3 cm) and the outer radius must be less than the radius of the existing solenoid (2.5 cm) at UNM. The SWS of the Bragg reflector was chosen to have a shallow corrugation ($r_1 << \lambda$); therefore, smooth wall waveguide relations [11] were used to determine the structure's parameters and then HFSS was used to optimize them. The axial wavenumbers are given by

$$h_{E,H} = [k^2 - (x_{E,H}/r_0)^2]^{1/2}, \qquad (3-5)$$

where subscript *E* denotes the TM mode and subscript *H* denotes the TE mode. The formulas (2 – 5) to (2 – 6) were used by replacing subscript *1* and *2* by *E* and *H*, respectively.

Since we use two spirals that convert the TM_{01} mode to oppositely rotating TE_{11} modes, the amplitude r_1 of sinusoidal corrugation must be doubled and the profile of the combined Bragg reflector is described by

$$r_w(z,\theta) = r_0 + 2r_1 \sin(\bar{h}z)\cos(\bar{m}\theta). \qquad (3-6)$$

The design formulas of the Bragg structure do not take into account the influence of the electron beam on reflector operation. Attempts to use a reflector with the same inner radius as that of the BWO's structure, when a uniform magnetic field is used, led to radiation with a complicated spectrum. The reason for such behavior is in the unfavorable influence of the reflector field on electron bunching for the operating TM_{01} mode in the BWO, unlike the field of the cavity-reflector that provides favorable azimuthally symmetric electron beam bunching. To weaken the influence of electrons on the operation of a Bragg reflector, we increased the radial gap between the electron beam and the reflector. This can be achieved in two ways, either by increasing the inner radius of the reflector or by using magnetic decompression of the electron beam. Using the design formulas, the Bragg SWS parameters were designed first with the inner radius close to the electron beam and then dimensional optimization was performed to increase the gap and keep the reflected power as high as possible. Table 3.2 shows the Bragg structure parameters before and after optimizing the radial gap.

Table 3.2 Increasing the radial beam-SWS gap.

Bragg-SWS Parameter	**Before Generation Optimization (Nonuniform Magnetic Field)**	**After Generation Optimization (Uniform Magnetic Field)**
R_{min}	1.55194 cm	1.778 cm
R_{max}	2.28346 cm	2.28346 cm
$r_0 = (R_{min}+R_{max})/2$	1.9177 cm	2.03073cm
$r_1 = (R_{min}-R_{max})/2$	0.36576 cm	0.25273 cm
$k = \omega/c$	209.5 m^{-1}	209.5 m^{-1}
$k_{\perp E} = x_{01}/r_0$	125.4 m^{-1}	118.4 m^{-1}
$k_{\perp H} = x_{11}/r_0$	96.011 m^{-1}	90.67 m^{-1}
$f_{\perp E}$	5.987 GHz	5.654 GHz
$f_{\perp H}$	4.584 GHz	4.329 GHz
$\beta_{\phi,E} = v_{\phi,E}/c$	1.2485	1.2124
$\beta_{\phi,H} = v_{\phi,H}/c$	1.1252	1.1093
$\lambda_E/2$	1.873 cm	1.819 cm
$\lambda_H/2$	1.688 cm	1.664 cm
$\lambda_{g,mean} = (\lambda_E+\lambda_H)/2$	1.78 cm	1.741 cm
h_E	166 m^{-1}	171 m^{-1}
h_H	185 m^{-1}	187 m^{-1}
$d=2\pi/h_E+h_H$	1.79324 cm	1.73736 cm
$\psi = tan^{-1}(d/2\pi R_{max})$	7.124^o	6.904^o
$\delta_{H,E}(\delta)$	0.259	0.169
N	12	8

In fact, increasing the radial gap between the electron beam and the Bragg reflector structure is the only way to overcome the unwanted radiation. However, the reflection coefficient for the Bragg reflector depends on the structure's depth and, as a result, the reflection coefficient will be affected. Fortunately, by decreasing the depth of corrugation, the reflection coefficient did not seriously drop, as shown in Fig. 3.8.

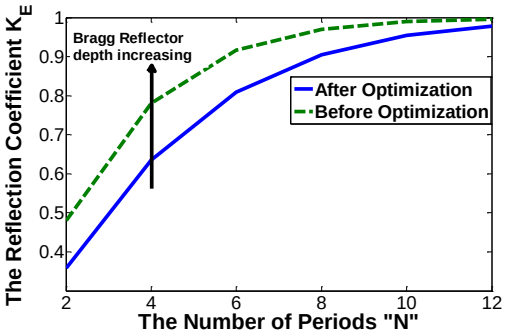

Figure 3.8 Calculated reflection coefficient as a function of Bragg reflector depth.

The reflection coefficient was calculated as a function of the number of periods ($K_P = \tanh^2(\delta L); L = Nd$) compared with the results obtained from HFSS simulation, as shown in Fig. 3.9. One can notice that there is not much difference in the reflected power if the Bragg structure has 8 or more periods. About 99.88% reflection before the optimization and 98.18% reflection after the optimization were calculated. Therefore, an 8 period SWS was chosen for our Bragg reflector design to be manufactured.

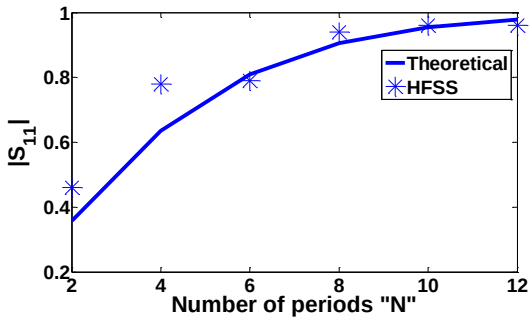

Figure 3.9 Dependence of reflection coefficient on the length of the Bragg reflector.

A solenoid is a simple way to implement a uniform magnetic field. Therefore, the Bragg reflector dimensions were chosen in which the radial beam-structure gap is increased and the reflection coefficient kept as maximum as possible. Even though there is little change in the reflection coefficient with longer length, 8 periods with more than 90% reflection is still an acceptable design, which was our choice.

The first technique that uses a dimensional optimization with a uniform magnetic field will be discussed in the reminder of this Chapter and Chapter 4 will present the experimental verification of this system. The second technique, increasing the gap by using a nonuniform magnetic field or magnetic field decompression, will be described and analyzed in Chapter 5.

Next, simulation studies of the Bragg reflector will be introduced to find the characteristic curve and measure both the reflection and transmission coefficients.

3.3. Cold SWS Characteristics

The difference in the radii of the BWO and Bragg SWSs introduces an impedance discontinuity. By injecting a TM_{01} mode at the output of the BWO, a small part of the TM_{01} mode reflects due to the discontinuity and another part penetrates through the Bragg reflector reflected from the anode. In other words, about 70% of the TM_{01} mode is converted to the TE_{11} mode and more than 96% of the TE_{11} mode will reflect back toward the output, as shown in Fig. 3.10.

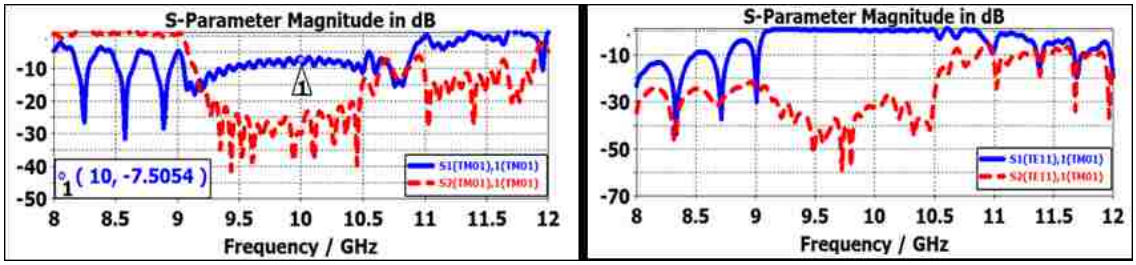

Figure 3.10 S-parameter shows the percentage of the power converted from the TM_{01} mode to the TE_{11} mode and the percentage of reflection.

A dispersion relation plot is very important to understand the propagation and coupling of modes. The dispersion characteristics of the modes of interest for both structures are

calculated using HFSS and are shown in Fig. 3.11. Intersection of the electron beam line (with energy γ = 1.9) with the -1st spatial harmonic of the backward TM_{01} mode means synchronism at frequency f = 10 GHz in the BWO. The intersection of lines of oppositely propagating TM_{01} and TE_{11} modes in the Bragg reflector forms the stop-band around f = 10 GHz where mode conversion occurs.

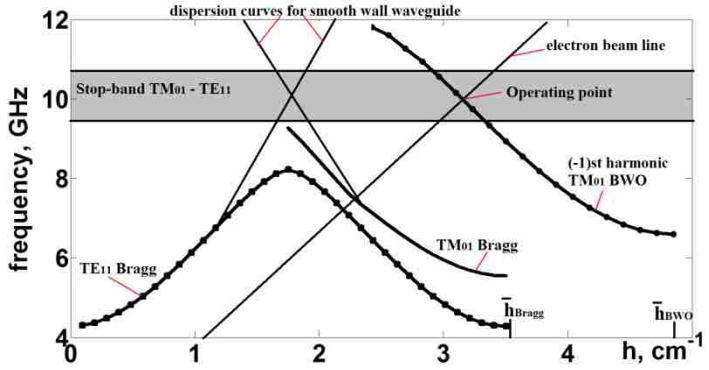

Figure 3.11 Dispersion diagrams of the lowest modes in both SWSs.

The frequency band of conversion or the Bragg stop-band can be written as

$$\frac{\Delta k}{k} = \frac{2\delta h_E h_H}{\bar{h}k^2}. \qquad (3-7)$$

3.4. BWO with Circularly Polarized TE_{11} Radiation

In this Section, hot test simulations of the BWO with single-fold left- or right-spiral Bragg reflector was considered. The aim of this investigation is to show that if the parameters of oppositely rotating TE_{11} modes of these BWOs are close, then it is possible to form a linearly polarized mode with their sum (e.g., when the combined Bragg reflector is used). The single-fold left-spiral corrugation ($\bar{m}$ = -1) and the single-fold right-spiral corrugation ($\bar{m}$ = +1) were investigated separately.

In MAGIC simulations, the left-spiral corrugation generates more output power than the right-spiral one and that is because of the coincidence with electron gyromotion. That is an indication how the Bragg structure fields affect beam modulation. By increasing the external magnetic field, this effect goes away due to decreasing the electron gyroradius and, thus, decreasing the electrons' transverse velocity.

Figure 3.12 shows the radial components of the electric field at different times. The TE_{11} mode is left-hand circularly polarized (LH) when the left-spiral corrugation is used and vice versa.

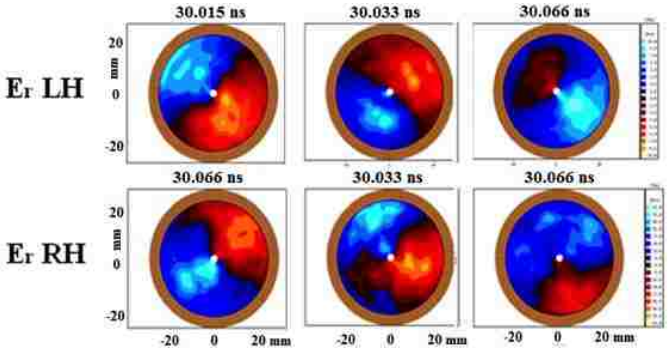

Figure 3.12 Field structure of the radiated TE_{11} mode for left-hand (LH) and right-hand (RH) circularly polarized radiation at different times.

Even though the SINUS-6 pulse that will be used in the experiment is a half-sine-wave-like pulse, a flat-top voltage pulse was used in simulations to investigate the rotation of the field.

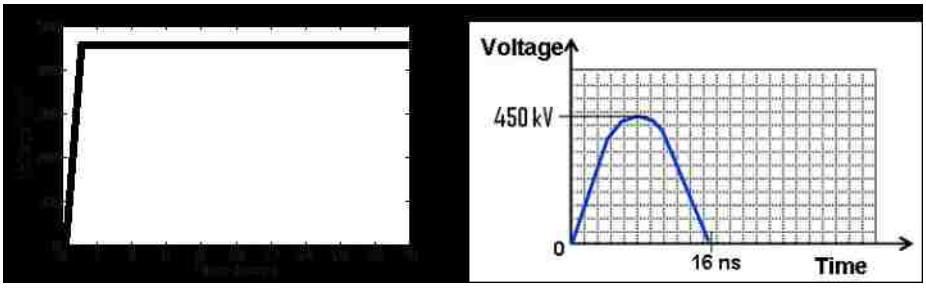

Figure 3.13 The input high voltage pulses.

3.5. BWO with Linearly Polarized TE_{11} Radiation

In order to produce linearly polarized TE_{11} modes, the combined Bragg reflector was used. For strong magnetic fields ($H > H_0$), MAGIC simulations show (Fig. 3.14) that the field structure at the BWO output corresponds to the TE_{11} mode with linear polarization and the direction of polarization is the same at all times; this is very important for applications. The direction of polarization is independent of the phase of the TM_{01} mode that is incident onto the reflector. The polarization direction is determined only by the initial phases of the spiral corrugations. Therefore, in order to change the direction of polarization, it is sufficient to rotate only the Bragg reflector.

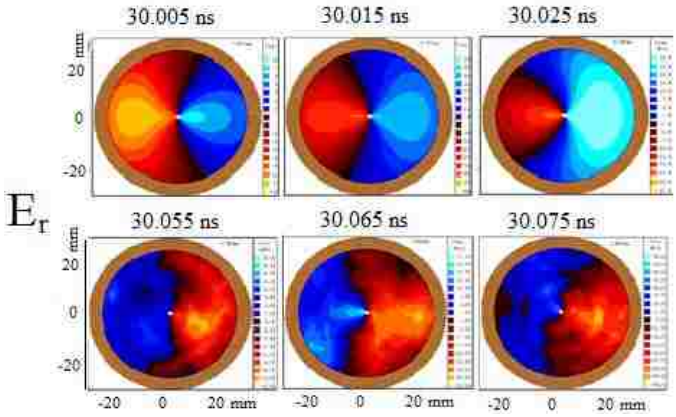

Figure 3.14 Field structure of the radiated TE_{11} mode at different times.

The dependence of frequency on the guide magnetic field near the RCSF was used for frequency tuning. In the RCSF, microwave generation is absent when the value of the magnetic field approaches H = 1.2 T. A 0.8 GHz frequency tuning was achieved with a radiated power P > 100 MW by changing the guide magnetic field from H = 1.5 T to H = 3 T, as shown in Fig. 3.15. The maximum radiated power P = 340 MW was achieved for a linearly polarized Gaussian beam at frequency f = 9.84 GHz when H = 1.95 T. This is when the applied voltage was U = 460 kV of a temporal half-sine waveform similar to

that of the output of the SINUS-6 accelerator. In this case, the efficiency of generation was 16 %, given as the ratio of the maximum output microwave power to the injected beam power.

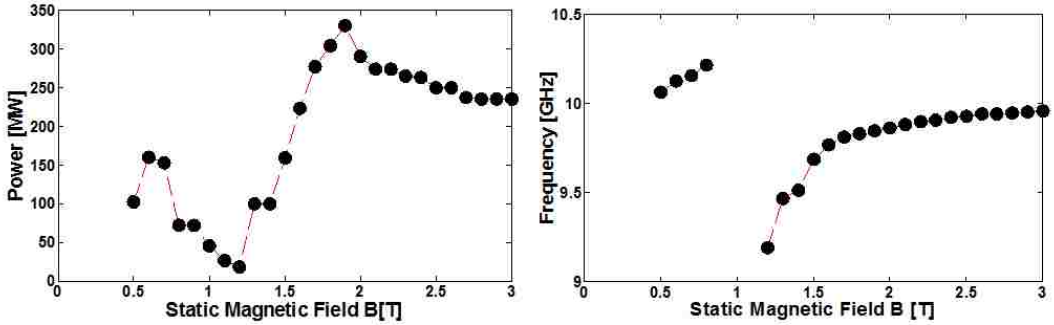

Figure 3.15 Dependences of radiation power P (left) and radiation frequency f (right) on the guide magnetic field H.

The technique of frequency tuning by changing the distance between the SWS of the BWO and the reflector is completely unsuitable here because of unfavorable modulation of the uniform electron beam for the operating TM_{01} mode caused by the field of the Bragg reflector. By plotting the axial momentum as a function of the device length, one can notice that the interaction between the electron beam and the Bragg reflector's electromagnetic field is much less intensive than in the BWO section, as shown in Fig. 3.16.

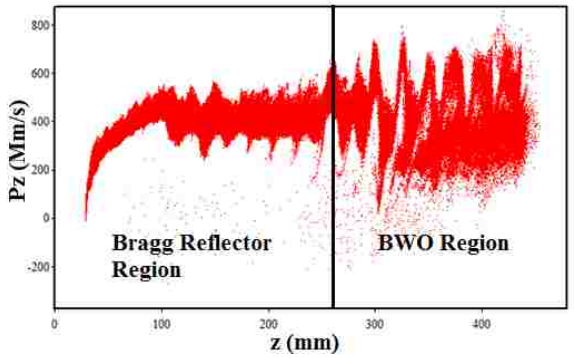

Figure 3.16 A phase-space plot of the electron momenta along the interaction region at 2 T guide magnetic field.

The unfavorable influence of the electric field of the Bragg reflector on pre-bunching the electron beam and the mix of parasitic waves may disrupt the operating wave. In this case, either increasing the reflector length or placing a simple grid consisting of parallel wires can be used at the output for mode purification. The simple grid array allows only radiation with polarization that is perpendicular to the wires to penetrate through it.

In our simulations we have observed some mixing up to 5% of power at some frequencies. In this case, we applied a simple grid consisting of parallel wires for purification of the output radiation (Fig. 3.17 (a)). These grids comprised wire conductors with a very small thickness and separation between wires that was much less than a wavelength. Therefore, only radiation with polarization that is perpendicular to the wires penetrated. As a result, the TE_{11} linearly polarized mode was radiated at the output and the TM_{01} mode reflected back and the TE_{11} mode was less contaminated, as shown in Fig. 3.17 (right).

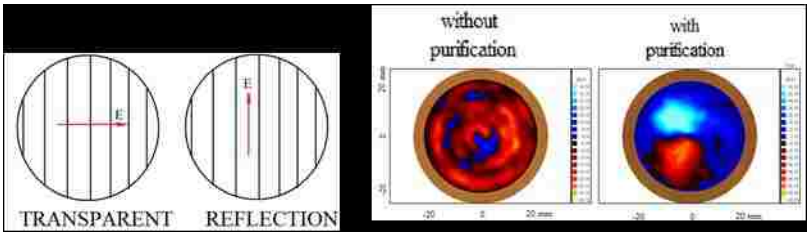

Figure 3.17 Left: Thin wire grids on the output of the BWO can be used for purification of radiation; Right: Purification of radiation (E_r) using a grid of parallel wires.

CHAPTER 4. EXPERIMENTAL RESULTS

Experimental results are very important to check the design and simulation results. Oversized waveguides are difficult to deal with. Unless the dimensions of the guide are such that only one transmission mode can exist, any excitation will set up several modes simultaneously. Both cold and hot tests were performed to gain a deeper understanding of our structures and the results are discussed.

4.1. Cold Test Experiment

In this section, cold test measurements were performed experimentally to obtain the dispersion characteristics of both the RBWO and the Bragg reflector structures (Fig. 4.1). For the RBWO, It is important to know the dispersion characteristics for SWS modes in order to synchronize the phase velocity of the wave with the electron beam to produce efficient interaction. In addition, it is important for the Bragg reflector to know the wave reflection, mode coupling, and conversion process.

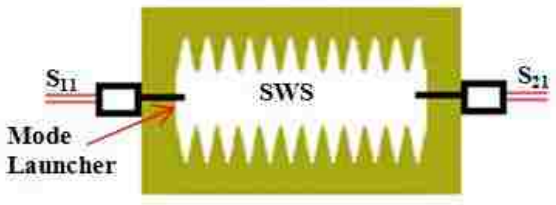

Figure 4.1 Cold test setup for both of the RBWO and the Bragg reflector.

The dispersion relation is found from the discrete measured resonant frequencies and wavenumbers of a cavity containing *N* periods of the SWS. Generally, a periodic SWS that has *N* periods will exhibit *N*+1 resonant frequencies when shorted at planes of mirror symmetry [87]. The aim of this study is to experimentally determine the dispersion

curves of the SWSs from the discrete resonant frequencies with phase shifts per period equally spaced between 0 and π. These resonant frequencies, which represent some points on the dispersion curve, can be determined by testing either the reflection coefficient [88] or the transmission coefficient [89] of the resonant cavity containing the SWS. Then, the complete dispersion relation can be constructed from these discrete points. In practice, it is much easier to find the frequencies than the wavenumbers. The dispersion relation extraction from the resonant frequencies peaks is widely used for the $TM_{0\rho}$ mode (see for example [90]) but there is no attempt to use this method for the TE_{11} mode, especially for an overmoded waveguide structure. Since our device radiates a TE_{11} mode, a TE_{11} mode launcher was designed using HFSS and experimentally tested.

4.1.1. Mode Launchers for Overmoded SWSs

In order to obtain a full dispersion curve from the experiment, a suitable mode launcher for effectively exciting both fast and slow waves needed to be designed. The monopole probe is a common $TM_{0\rho}$ mode excitation method. However, it is difficult to excite the slow waves, especially for π-mode, for which the on-axis field must not be a maximum value [88]. A coupling probe at the side of the SWS (side coupling) can excite the slow wave, but it also excites asymmetric TM modes and even undesired TE modes. A cage antenna radiator and a rod-wheel radiator have been introduced [88] to overcome this issue, especially for π-mode, 2π-mode, and higher order modes. Because we are neither interested in higher order modes nor the π-mode operating point, a λ/4 monopole antenna radiator mounted on a ground plane was used to excite the TM_{01} mode at 10 GHz.

Since the propagated waves in our device are TM_{01} and TE_{11} waves, a patch antenna was designed in order to excite the TE_{11} mode, as shown in Fig. 4.2. Microstrip antennas are simple, easy to design, and inexpensive to manufacture [91]. A circular microstrip patch antenna was the basis of our design, which is basically a circular patch on one side of a substrate and a ground plane on the other side. The modes supported by circular patch antenna can be found by treating the patch, ground plane, and material between them as a circular cavity [92,93]. In fact, the circular patch antenna is usually analyzed using a cavity model. By using a cavity model, it is reported that TE modes are not excited because they cannot propagate on the surface of the dielectric. Surface waves are not desirable because they extract power from the direct radiation and scatter at the surface discontinuities. In actuality, no propagation on the surface can be considered an advantage because it leads to weak coupling to the SWS wall. Thus, a clean mode will be excited in the structure. Since a circular patch antenna cannot excite the desired wave (TE_{11} wave), our design was more complicated than the basic patch antenna described above [94,95].

The TE_{11} mode launcher is composed of two layers of a substrate with two 8 cm×8 cm ground planes. The upper ground plane contains a circular patch with a 0.75 cm radius and the lower one has a 0.3 cm×4.5 cm rectangular slot that is fed by a stripline on the opposite side of the other substrate. The stripline excites a uniform field in the rectangular slot which couples to the TE_{11} mode of the circular waveguide through the circular patch. The existence of the upper ground plane with a circular slot prevents the excitation of the higher order modes.

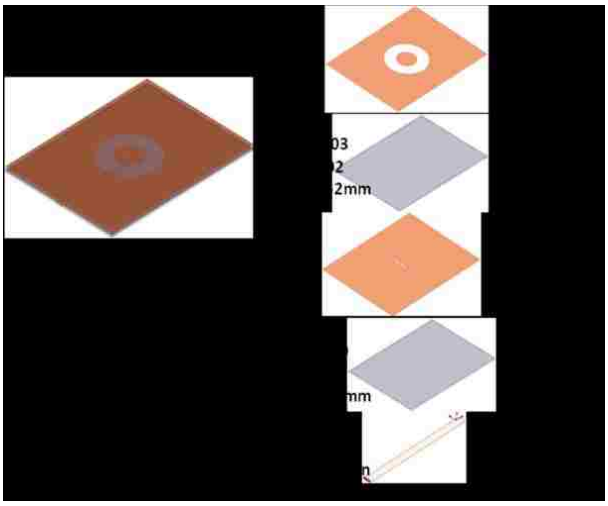

Figure 4.2 Patch antenna launchers for TE_{11} mode excitation in an overmoded SWS.

Even though the SWSs are overmoded waveguides, higher order modes were not excited when both launchers were tested. The monopole antenna successfully excited a clean TM_{01} mode, while the patch antenna excited the TE_{11} mode in an overmoded smooth wall waveguide, as shown in Fig. 4.3.

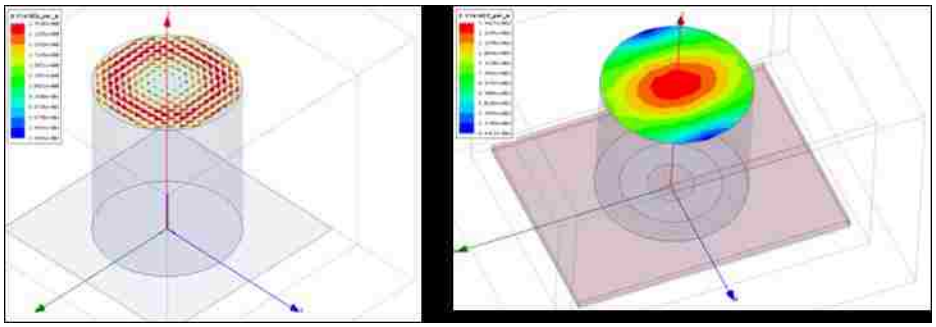

Figure 4.3 The mode launchers inside overmoded smooth wall waveguide.

4.1.2. Dispersion Characteristics Extraction

The experimental setup for dispersion curve extraction is shown in Fig. 4.4. An HP-8720D vector network analyzer (VNA) was used to measure both the reflection coefficient (S_{11}-parameter) and the transmission coefficient (S_{21}-parameter) when the

vertical scale was 10 dB/div and the horizontal axis was 0.5 GHz/div for all measurements. Using the S-parameter measurements the dispersion relation can be extracted.

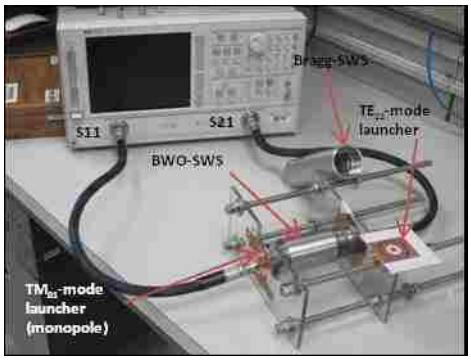

Figure 4.4 The cold test measurements setup.

The monopole antenna, which was designed at 10 GHz, was attached to the SWS of the BWO to launch the TM_{01} mode. From HFSS simulations, the propagated mode inside the overmoded SWS was a clean mode, as shown in Fig. 4.5. That gave us confidence to carry out the experiment and be sure that the measured reflection and transmission coefficients belonged to the desired mode, as shown in Fig. 4.6.

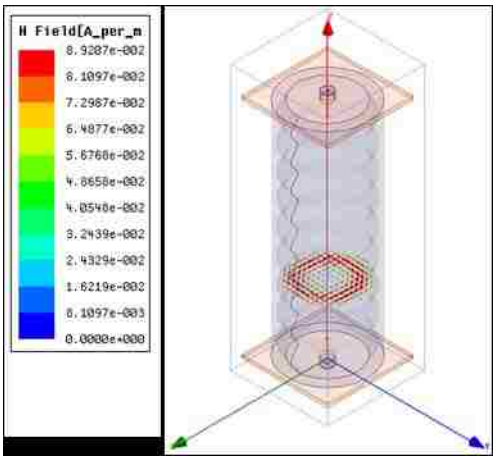

Figure 4.5 The magnetic field distribution of a clean TM_{01} mode propagates inside BWO-SWS at 10 GHz.

In principle, the complete dispersion curve of an arbitrary SWS can be obtained by

measuring very large numbers of discrete resonances associated with long structures (infinite number of periods). Since this is not practical, one needs some form of interpolation between small numbers (N+1) of experimentally measured points on the dispersion curve [88]. Because the SWS of the RBWO has 9 periods, 10 resonances were observed. The phase shift between each period of the SWS was 20°. By plotting the resonant frequency values as a function of the phase shift, the dispersion characteristics were obtained, as shown in Fig. 4.6. The experimental data were plotted as dots, while that simulation results were plotted as solid lines in all figures.

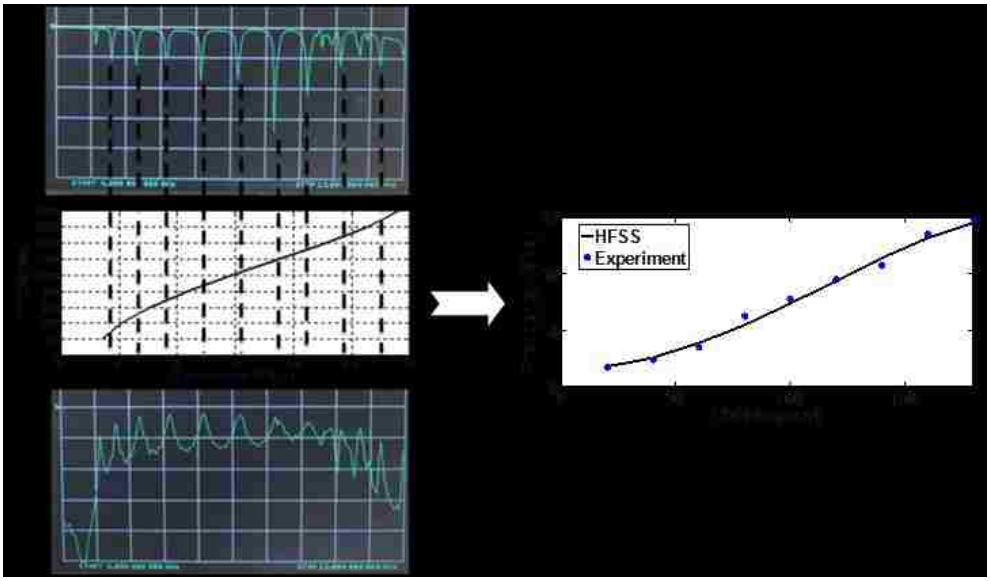

Figure 4.6 The experimentally measured reflection coefficient resonant peaks and the obtained dispersion curve for TM_{01} mode BWO-SWS.

Since 10 GHz is a band gap for the Bragg reflector, another monopole was designed at 7 GHz to excite the TM_{01} mode inside the structure. The dispersion curve was obtained for the Bragg structure by using the same method as the one described in the previous paragraph. In this case, the phase shift is about 22.5° since the SWS of the Bragg reflector has 8 periods. The measured points of the dispersion relation and the simulation are shown in Fig. 4.7.

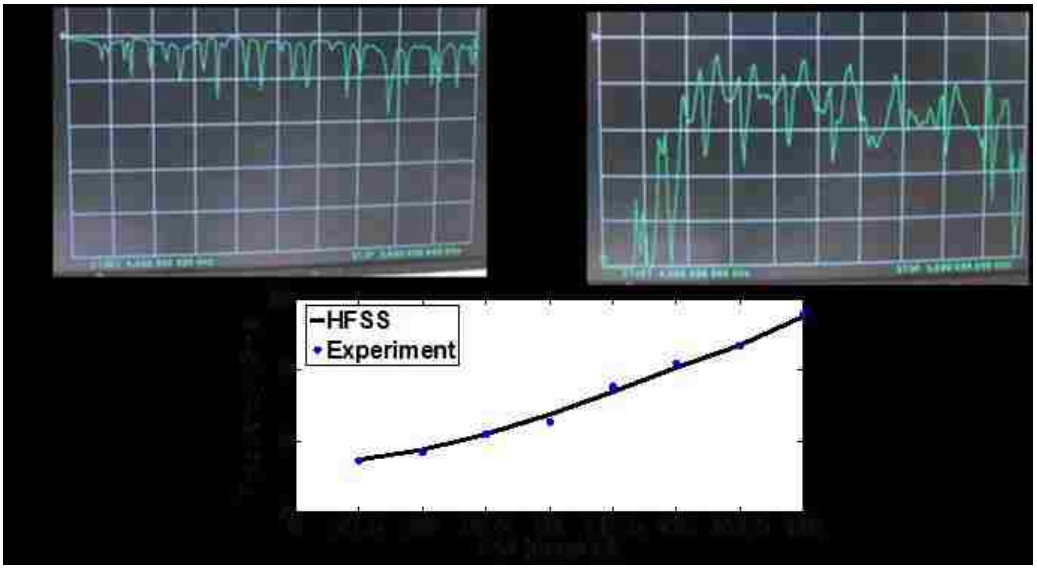

Figure 4.7 The reflection coefficient resonant peaks for TM_{01} mode of the Bragg-SWS and the dispersion relation.

The following procedure was performed in order to excite the TE_{11} mode by using a patch antenna (Fig. 4.2). Two patch antennas were connected at opposite ends of the Bragg reflector to measure the S-parameters. The patch antenna launched a clean TE_{11} mode inside the Bragg reflector structure, as shown in Fig. 4.8. Since the Bragg reflector is a combination of left- and right-single-fold spiral corrugations, a frequency split was observed. The frequency split can be related to some fabrication issues as well. By averaging the two adjacent frequency peaks, the dispersion curve was constructed. As shown in Fig. 4.9, the extracted dispersion curve from the measured S-parameters was in good agreement with the simulation results.

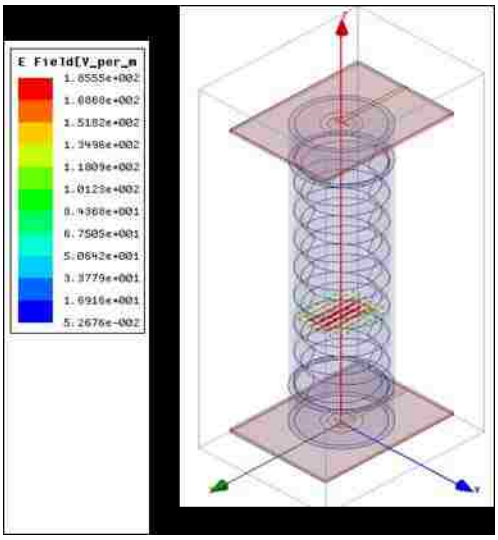

Figure 4.8 The electric field distrubtion of a clean TE_{11} mode inside Bragg-SWS at 7 GHz.

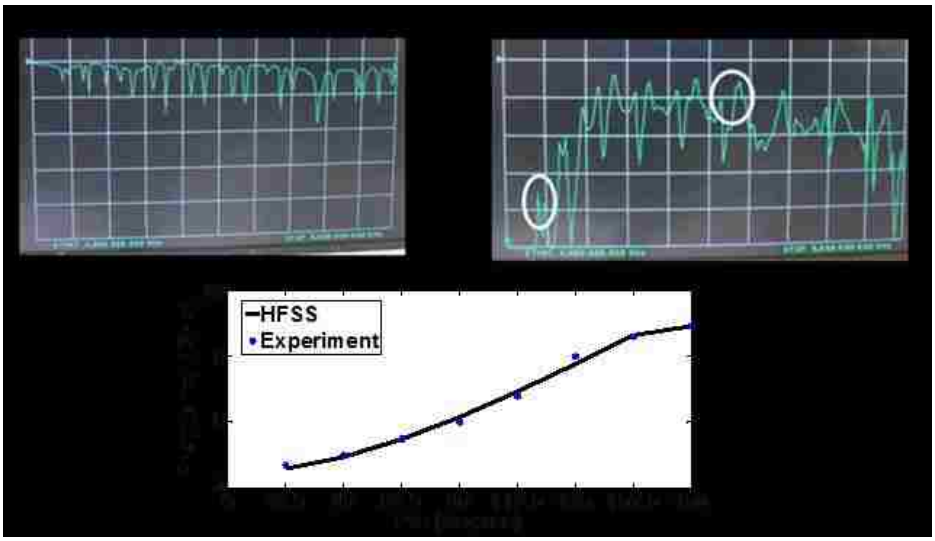

Figure 4.9 The reflection coefficient resonant peaks for TE_{11} mode of the Bragg-SWS and the dispersion relation.

4.1.3. End Reflections of SWSs

End reflection coefficients affect both the start conditions and the saturation effects of the BWOs. In addition, they affect the performance of the Bragg reflector. The end reflection coefficients can be measured by launching the desired wave inside the structure and measuring the S_{11} parameter using the VNA for both open- and shorted-ended SWSs.

By placing the short the diffraction loss is eliminated. The end reflection coefficient can be easily calculated by exploiting its relation to the diffraction quality factor of the SWS [97]. The diffraction quality factor of a structure is related to the radiation power loss by diffraction through the output aperture of the cavity. Furthermore, the Ohmic loss in the structure wall from resistive heating is related to the Ohmic quality factor. From the resonant peak, the quality factor can be calculated as $f_o/\Delta f$ where f_o is the operating frequency and Δf is a -3 dB level at which to record the upper and lower frequencies. To find the diffraction quality factor, the total quality factor was measured when the SWS was open, whereas the Ohmic quality factor was measured when the SWS was shorted (the diffraction Q is the difference between them).

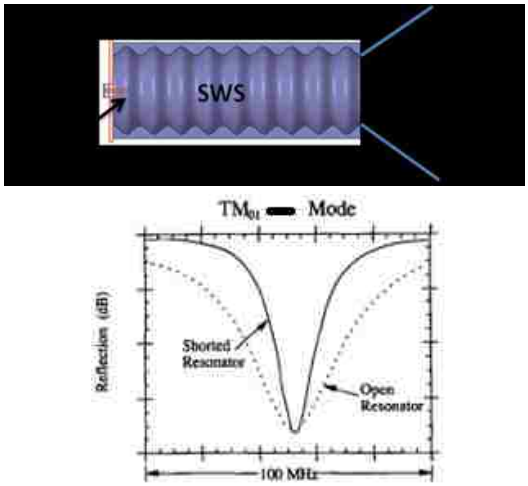

Figure 4.10 The measured transmission coefficient [88].

The end reflection coefficient is related to the quality factor by [88]

$$\Gamma = \sqrt{\frac{1 - F(\omega)}{1 + F(\omega)}};\ F(\omega) = \left(\frac{N\,d}{\bar{h}\,Q}\right)\left(\frac{\omega}{c}\right)^2, \qquad (4-1)$$

where ω is the operating frequency, d is the period, and Q is the diffraction quality factor.

4.2. Hot Test Experiments

In order to produce HPM radiation using a RBWO one needs an intense electron beam which gives its kinetic energy to the structure's electromagnetic field. The SINUS-6 accelerator at UNM provides the RBWO with a relativistic electron beam through an annular cathode. The electron beam is confined through the RBWO's structure by a guiding magnetic field. An electromagnet produces a strong guide magnetic field that diffuses through the tube and SWS walls. Before discussing the hot test experiments, brief explanations for both the pulsed power and the pulsed magnet systems will be given in the next Subsections.

4.2.1. Pulsed Power System

The main components of the SINUS-6 accelerator are shown in Fig. 4.11. The SINUS-6 accelerator produces an intense, relativistic electron beam with energy of up to 700 keV. It is a compact and efficient device and may operate in both single shot and repetitive pulse regimes, although repetitive operation capability was disabled at UNM. It consists of a bank of storage capacitors, a Tesla transformer, a nitrogen-filled high voltage spark gap switch, and a transmission line leading to a cold cathode housed inside a vacuum diode. A graphite annular cathode produces an annular electron beam with an outer diameter of 2.7 cm and a thickness of 0.51 mm.

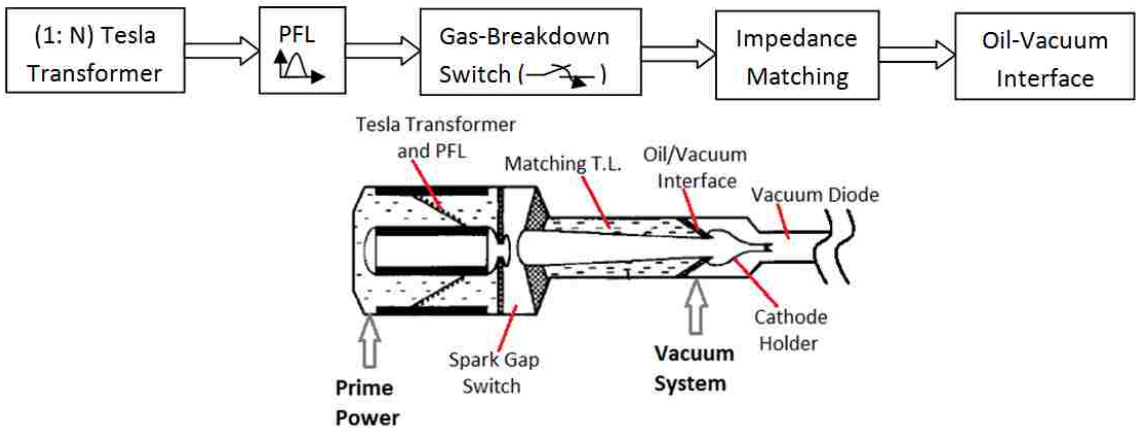

Figure 4.11 Block diagram and cross-section of the SINUS-6 accelerator.

Generally, the operation of the SINUS-6 in the single shot mode is not complicated. Basically, a 3-phase prime power system charges six parallel capacitors totaling 3 mF to provide a Tesla transformer with 300 V input. The Tesla transformer steps up the voltage from 300 V to 700 kV. The 1:3500 turns ratio of the transformer is immersed in oil, with a pulse forming line (PFL) at the output in order to provide a 12 ns duration pulse to the spark gap switch. The capacitance of the PFL is about 250 pF with a charging time of 60 μs, while the high voltage switch is a nitrogen-filled spark gap pressurized to 20 atm. The switch has spherical electrodes of 4 cm radius and a 2 cm gap. Since the output impedance of the PFL and the vacuum diode are different, an oil-filled adiabatic transmission line is used. The transmission line matches the 20 Ω impedance of the pulse forming line to the 100 Ω impedance of the vacuum diode. At this point, the high voltage pulse propagates from oil to vacuum and is ready for application to the vacuum diode. Therefore, an oil/vacuum interface is used to separate the transmission line from the vacuum diode. The interface is magnetically insulated to prevent any flashover that could be caused by backstreaming electrons. As an additional protection, a stainless steel cathode holder covers the weakest part of the system, which is well known as a triple

point [98]. Once the voltage pulse is applied between the cathode and 5 cm diameter anode, an explosive-emission graphite cathode provides an annular beam to be injected into the SWS. Since the base pressure in the vacuum region must be less than 1 mTorr, an external vacuum system was used to reach 10^{-5} Torr vacuum condition. Lastly, the beam was confined through the length of the diode by a magnetic field on the order of 2 T, which was provided by an electromagnet.

4.2.2. Pulsed Magnetic System

For single shot operation, solenoidal coils are used to provide the system with a uniform magnetic field. Strong magnetic fields not only guide the electron beam but also contribute to the microwave power. In this experiment, 12 coils enclose the magnetically insulated coaxial vacuum diode. A 2 T uniform magnetic field guides the electrons from the cathode tip to the collector. A block diagram of the magnetic pulse components and its setup are shown in Fig. 4.12.

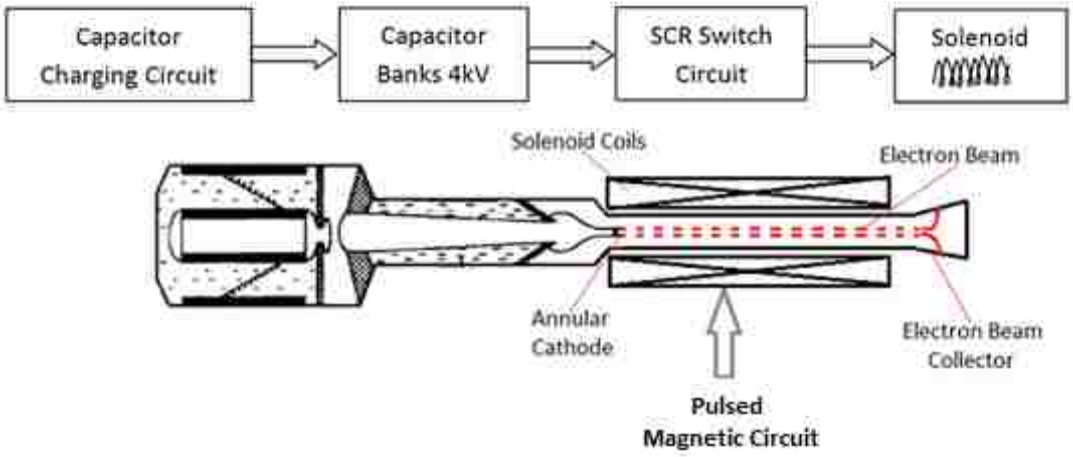

Figure 4.12 Pulsed magnetic system.

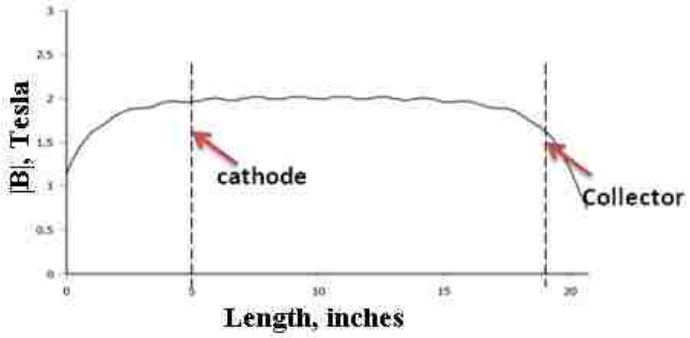

Figure 4.13 FEMM simulation of the magnetic field strength as a function of axial position showing the positions of the cathode tip and the end of the SWS [99].

Figure 4.13 shows the magnetic field strength in relation to the axial position of the vacuum tube. The field should be shaped such that it is homogeneous throughout the SWS; the magnetic field lines should flare out upstream of the cathode tip and also where the beam dump is located. This geometry is necessary to decrease plasma drifting into the SWS. Unfortunately, this was not the case here, since the magnetic field lines were flaring at the last half of the RBWO length. Because of the way the tube was constructed, shifting the SWS or magnetic field coils would require extensive machining of new parts. It was hoped that the flaring magnetic field lines would not greatly affect the results, so the experiment was carried out in spite of this issue. The solenoidal coils and the charging/discharging magnetic circuit are shown in Fig. 4.14.

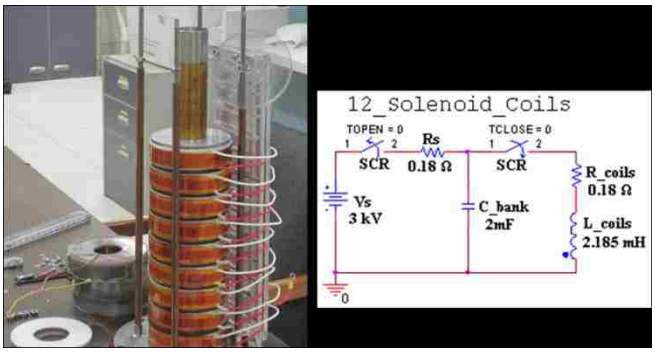

Figure 4.14 Photograph of the solenoid coils (left) and the magnetic pulse circuit (right).

The pulsed magnetic circuit is constructed such that the coils are connected in

parallel. A 2 mF capacitor bank was charged to 3 kV and then discharged into the coils by triggering a thyristor SCR switch circuit. The current through the coils was measured across a very small resistance (CVR = 5 mΩ; see Appendix) and the discharging signal was oscillating as an under-damped circuit behaves. After 3.8 ms from the discharging trigger pulse, a second trigger signal was sent to the SINUS-6 to apply its high voltage pulse. At this point, the hot test should begin, as will be described in the next Subsection.

4.2.3. Experiment Assembly and Diagnostics

The photographs of the electrodynamic components used in the experiments are shown in Fig. 4.15. The SWSs were manufactured from stainless steel. Two types of antennas were used: the first antenna that was selected was an aluminum conical horn antenna, which has a high gain. Due to some technical issues (e.g., not enough space to measure far field radiation, among others), the horn antenna was replaced by a stainless steel "coffee can" antenna, which is basically a waveguide aperture antenna.

Figure 4.15 The electrodynamic components of the experiment.

The experiment assembly was accomplished by attaching the vacuum tube to the SINUS-6 and sliding the coils around the tube to form an electron gun. The SWSs were inserted inside the tube after being threaded together; then the antenna was connected at

the BWO output, as shown in Fig. 4.16. When the vacuum condition reached 10^{-5} Torr, the high voltage firing process was initiated. This allowed a smooth streaming of electrons from the cathode tip to the collector. Before starting the measurements, cathode alignment was achieved to position the cathode at the center of the SWS. The cathode was aligned by visually checking the electron beam trace on a plastic witness target.

The general experiment setup is shown in Fig. 4.16, where the oscilloscopes and the computer control system are located inside a shielded screen room to prevent any interference. All parts of the experiment were calibrated before the hot test was carried out (more information about the calibration process can be found in the Appendix). In addition, all measurement signals were attenuated before sending them to the screen room since we are dealing with high voltage signals. Beam current and cathode voltage are measured using a Rogowski coil and capacitive divider, respectively (see Appendix). The SINUS-6 output pulse that was applied to the input of the vacuum diode is a half-sine-like wave, as shown in Fig. 4.17. Because the output impedance of the transmission line and the input impedance of the RBWO are not exactly the same, some reflections were noticed. The reflected voltage levels were very small compared to the main pulse and the corrsponding electron beam energy was small as well. Therefore, the electrons were not able to interact with the SWS eigenmodes at the operating frequency due to their small kinetic energy.

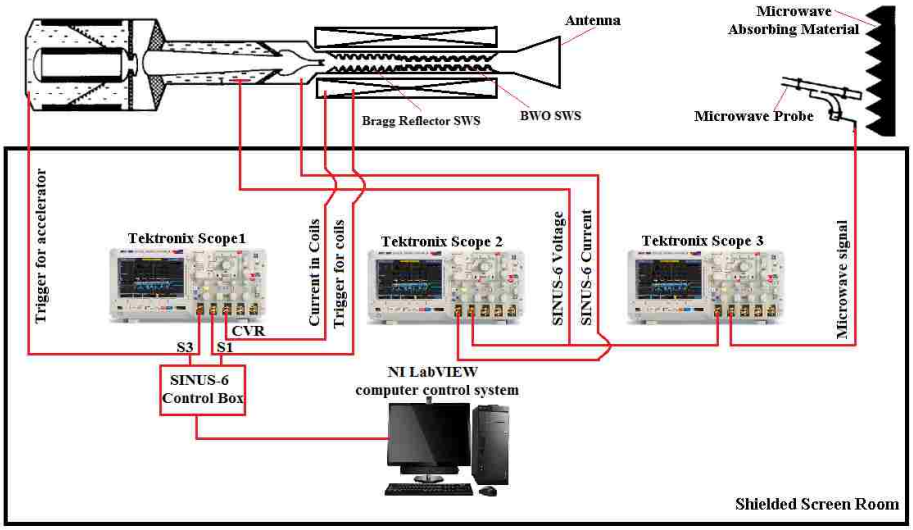

Figure 4.16 A schematic of the experiment setup and diagnostics.

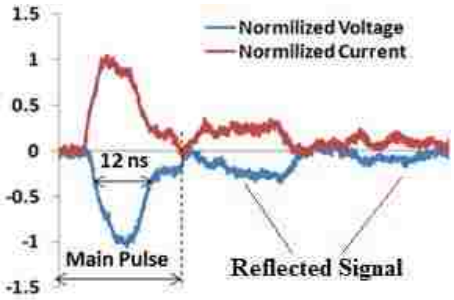

Figure 4.17 The SINUS-6 output pulse.

The microwaves radiated through the transmitting antenna were picked up by an X-band rectangular waveguide. They were attenuated by a 20 dB directional coupler and then sent to a shielded screen room using an RG 213 coaxial cable. The detector itself, an open-ended section of the WR-90 waveguide, was used to measure the microwave radiation. The area of the open end of the waveguide was 1.696 cm^2 with an effective aperture area ranging from 1.98 cm^2 to 1.57 cm^2 over a bandwidth of 9 – 10 GHz. For field pattern diagnostics, a neon bulb array was used and photographs were taken at different shots.

The classic neon bulb is made of a glass tube containing a mixture of neon (99.5%)

and argon gas. There are two electrodes, one positive, and one negative. Voltage rises and an arc is struck between them. Argon gas is used because of a lower striking temperature. After the argon strikes an arc the neon gas is warmed and current is able to flow through the neon gas, ionizing more atoms as the current rises. The neon lamp works on AC or DC power. When using the lamp with DC, only one of the electrodes will glow since ions are formed off of that electrode. AC power provides a nice uniform look with a glow evenly distributed. Neon bulbs are widely used as a detectors of radiation up into the optical regime. They have been successfully used as pixels in several experimental imaging arrays. In order to turn the bulbs on, they must be immersed in an electric field with an orientation sufficient to induce the trigger voltage. Since the trigger voltage is what determines when the neon begins to conduct and glow a 65 VAC turns it on while 90 VDC must be applied. When starting voltage is applied, the gas ionizes and start to glow permitting a very small current to travel between electrons. The nearly constant voltage over wide variation of the induced current made neon bulbs useful as voltage regulators before semiconductor Zener diodes became available.

The use of open-shutter photographs of neon bulbs radiated by microwaves gives information on the relative power, mode pattern, and mode purity of the microwaves. The neon bulb array was placed at both at the near field and far field from the transmitting antenna.

It should be mentioned here that the SINUS-6 high voltage was not measured in the vacuum diode; instead, the capacitive voltage divider probe is placed in the matching transmission line, where the probe was immersed in oil. The voltage is different from what is actually the voltage at the tip of the cathode (Fig. 3.4.8). According to [100], the

voltage value should increase by 2.5 times as the pulse propagates from the oil to the vacuum; also, a time delay should take place. For accurate measurements, we started at 460 kV measured in the oil, and the voltage was increased to reach the required value at the cathode.

Since there was no capacitive voltage divider probe close to the cathode tip, the Rogowski coil measurements were our standard current diagnostic. The Rogowski coil was located at a distance 15 cm from the cathode tip in vacuum, while the capacitive divider probe was at a distance 53 cm from the cathode tip in oil, as shown in Fig. 4.18. Thus, the voltage and the current measurements had about a 1.6 ns time delay between them.

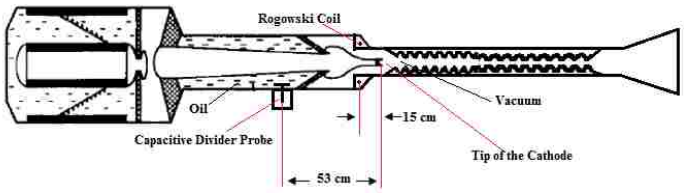

Figure 4.18 The SINUS-6 voltage and current probes for measurements at UNM.

4.2.3.1. Results of 460 kV at the Capacitive Divider Voltage Probe

When the voltage was 460 kV, the peak current measured by the Rogowski coil was about 3.3 kA. At this voltage level, the microwave probe and the neon bulb array were placed 38 cm from the output of the RBWO, as shown in Fig. 4.19. Their location was closer to the antenna than they were to the far field of the transmitting antenna, which is given approximately by $L = 2D^2/\lambda$, where D is the diameter of the antenna and λ is the wavelength of the radiated microwaves. Since the diameter of the antenna was approximately 10 cm and the wavelength was 3 cm, the distance to the far field is greater

than 70 cm, while the distance of the microwave diagnostics from the transmitting antenna was only 38 cm. Since the neon bulb array was placed in the near field, the photographs showed the bulbs lighted at various brightness. In most shots, a bright spot appeared at the center of the array, and often it displayed the expected structure of the mode. Not all of the bulbs illuminated uniformly and reproducibly because some of the bulbs were broken and the mode was impure. Therefore, care had to be taken in interpreting the mode structure, especially as the bulb array was in the near field of the transmitting antenna.

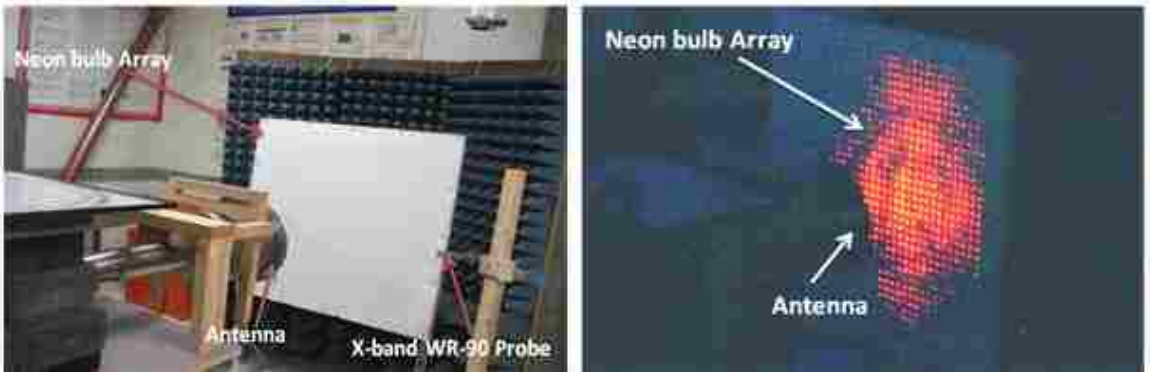

Figure 4.19 Open-shutter photograph of neon bulb array breakdown at 38 cm distance from the antenna.

The measured data of the microwaves, which was picked up by the microwave probe and displayed by a fast speed oscilloscope, was recorded for detailed analysis. The frequency of the microwaves that radiated from the RBWO was obtained by using the fast Fourier transformer (FFT) technique to confirm that the device was operating in the predicted frequency. From Fig. 4.20, the device transmitted two main frequency peaks, which means it was not operating in a single mode. We inferred that either a significant frequency chirp existed during the pulse or two modes were present. Since we knew of no previous observations of frequency chirping at this operation condition, we thought that more than one mode was operating at 460 kV input voltage. From Fig. 4.20, the

predominant operation appeared to be at 10.1 GHz, which agreed with our theoretical calculations for the TE_{11} mode.

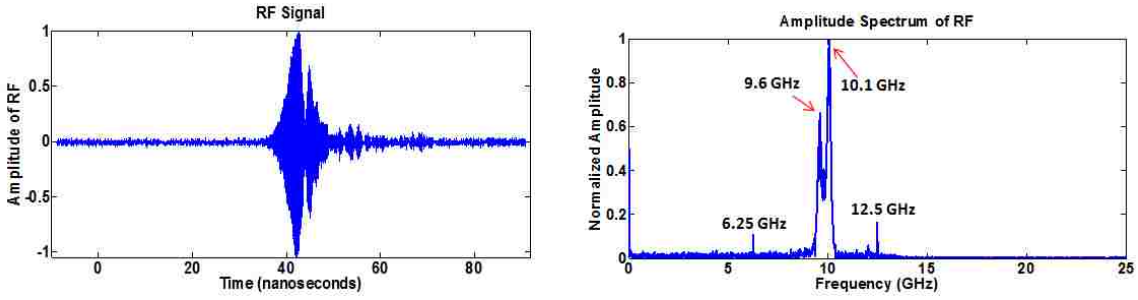

Figure 4.20 The normalized near field signal and its FFT.

Four frequency peaks were measured (6.25, 9.6, 10.1, 12.5 GHz), which means that the RF signal needed to be studied in depth. To understand the FFT of the RF signal (Fig. 4.20), the microwave signal of a 0 – 90 ns window was divided into five windows (36 – 56 ns, 36 – 44 ns, 44 – 49 ns, and 49 – 56 ns), as shown in Fig. 4.21.

The window 0 – 36 ns was basically a delay caused by the coaxial cable, the directional coupler, and the attenuators. The two small frequency peaks at 6.25 and 12.5 GHz are related to noise picked by the cable. For all windows that are shown in Fig. 4.21 the two small frequency components disappeared by deleting this time frame. The first pulse (36 – 44 ns) has a very clean frequency component at 10 GHz, which is the predominant wave. The second pulse in the 44 – 49 ns window is oscillating at 9.6 GHz with 4 ns duration and its power is less than 40% of the main RF pulse. The 49 - 56 ns window (Fig. 4.21 (d)) represents the third pulse, which is a mix of the first and the second pulses (less than 10% of the main pulse).

The radiation at 9.6GHz is the excitation of nonaxisymmetric waves with azimuthal variation which was caused by an off-axis beam and nonuniform emission of the cathode tip. This frequency peak disappeared as the voltage increased. In fact, this pulse did not

appear in our MAGIC simulation with the same operation condition, which support out interpretation.

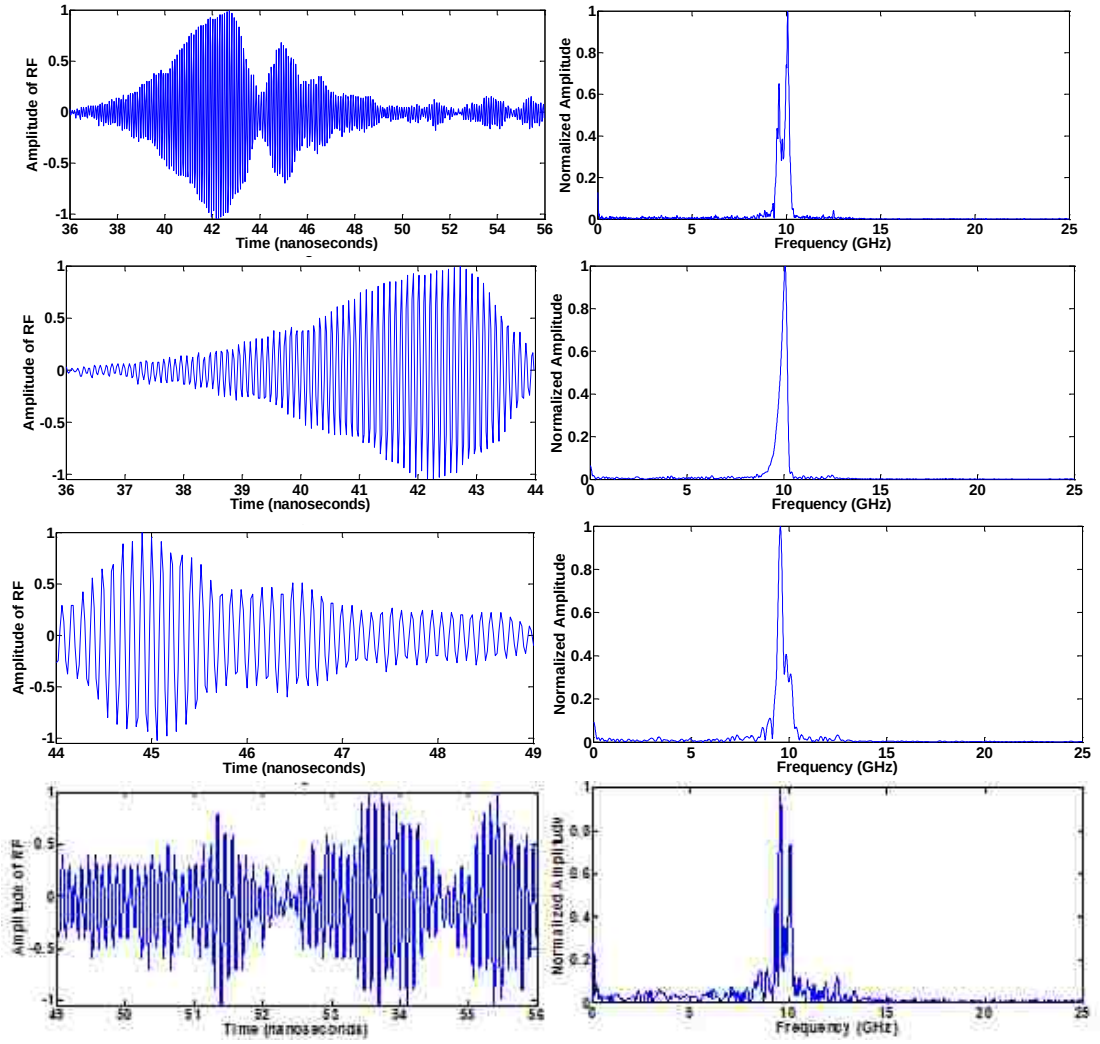

Figure 4.21 The FFT signal with different time windows.

In addition to our analysis, we normalized and squared the output signal to obtain an estimate of the radiated waveform, as shown in Fig. 4.22.

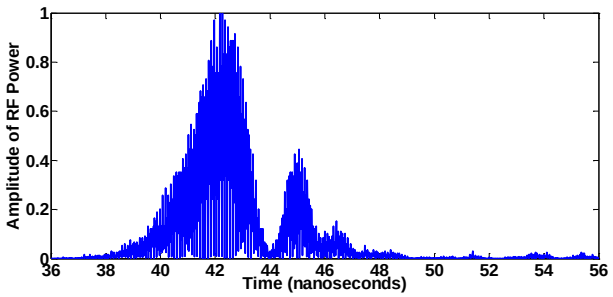

Figure 4.22 The normalized power waveform.

The polarization of the microwaves was estimated by rotating the rectangular aperture of the probe and recording the maximum of the RF signal. The ratio of the vertical polarization and the horizontal polarization gave us an idea of the microwave polarization, as shown in Fig. 4.23. A linearly polarized wave in the vertical plane was obtained, which means that the output mode was mostly a TE_{11} linearly polarized mode.

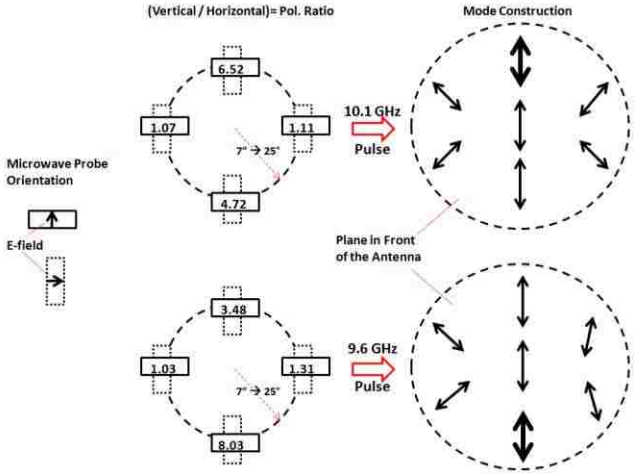

Figure 4.23 Polarization measurements and mode construction. The ratio of the maximum field when the microwave probe is horizontal (vertical polarization) and the microwave probe is vertical (horizontal polarization).

From the neon bulb array light pattern and the polarization measurements, one needs to measure the pattern in the vertical plane. By performing a vertical pattern scan, the field pattern at the near field was not clean, since the pattern was still forming side lobes were present. The scan was performed to ± 36° from the center of the transmitting

antenna, and the maxima of the first pulse were plotted, as shown in Fig. 4.24. The pattern has large side lobes, in which ground reflections can play an important role in increasing the side lobes.

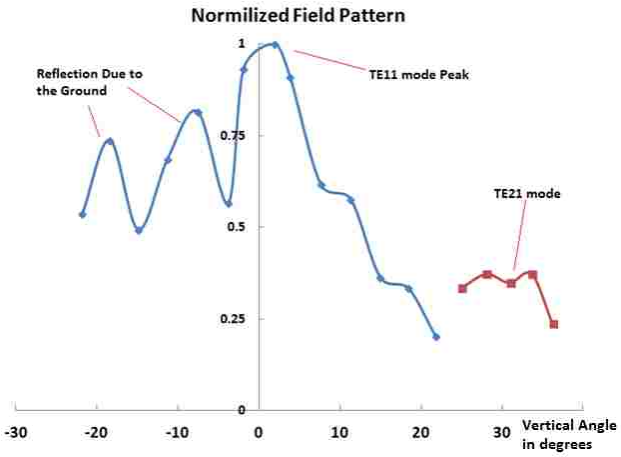

Figure 4.24 The normalized field pattern on the vertical plane at 35 cm from the antenna.

Next, we wanted to increase the voltage and increase the distance between the antenna and the diagnostic probes in order to reach the far field. Some of the pervious measurements were repeated for higher voltages in order to gain deeper insight into the device operation. The results are described in the next Subsection.

4.2.3.2. Results of Experiments with 510 kV at the Capacitive Divider Voltage Probe

In this part of the experiment, the microwave probe and the neon bulb array were placed at the far field distance. Figure 4.26 shows the normalized RF signal that was picked up by the probe. The frequency content was determined performing an FFT on the microwave signal. By increasing the voltage, the FFT became cleaner, as can be seen in Figures 3.4.10 and 3.4.15. At 510 kV only one main pulse was measured. Even though

the RBWO was found to operate at 10.1 GHz, which is in good agreement with the analytical and numerical results, the mode pattern was not as clean as required, as shown in Fig. 4.27.

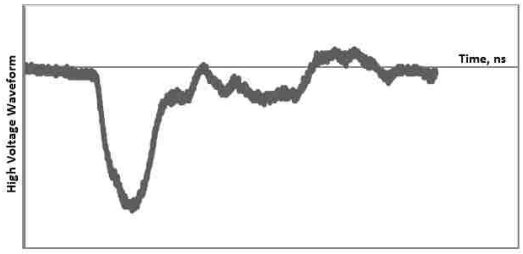

Figure 4.25 The input high voltage pulse shape at 510 kV.

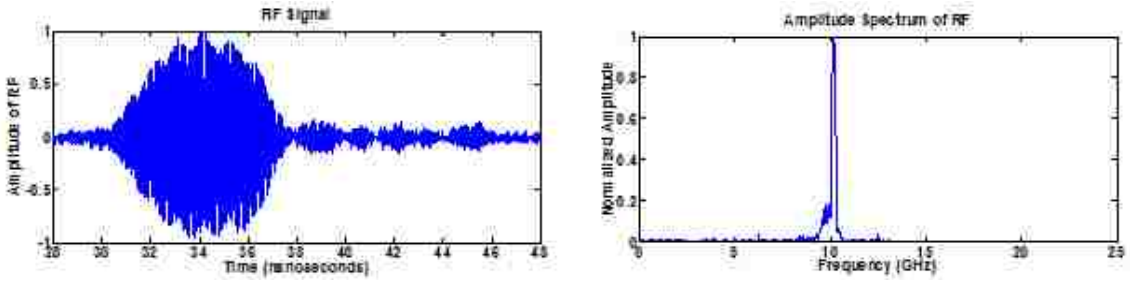

Figure 4.26 The normalized output microwave and its FFT.

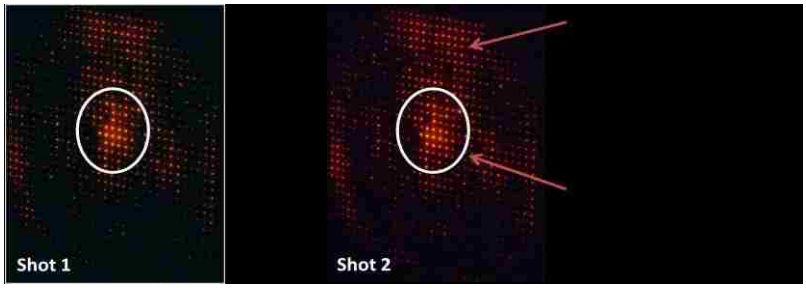

Figure 4.27 Far field radiation pattern at a distance 100 cm from the antenna.

It was obvious that the output mode is not a clean TE_{11} mode, since a mix of other mode patterns appeared again, as shown in Fig. 4.27. Since the oscilloscope that was used in this experiment is limited to 12.5 GHz, higher frequency modes could have been generated and not detected by our diagnostics. The appearance of additional, higher-frequency modes seemed to be typical in higher beam current experiments [41] where the

beam current (4.4 kA) is about 3.3 times the start current (1.35 kA). This suggests that, at high currents, the start current threshold is exceeded for more than one mode. For the parameters of our SWS, the TM_{02} passband extends from about 13.7 GHz to 17 GHz, which suggests this mode can be a candidate for the second mode. A fraction of the TM_{02} mode could have been reflected by the Bragg reflector and the cathode with a different mode pattern. In addition, BWO linear theory calculations (Chapter 2) show that the larger ripple leads to a larger growth rate for the BWO instability. Intuitively, one would expect that the larger growth rate translates to reduced start current thresholds for the TM_{01}, nonaxisymmetric, and higher modes as well. Thus, the SWS was operating in multiple modes, as was observed in the experiments.

These were some reasons behind generating impure modes that are related to the RBWO section. More reasons for mode impurity can be listed as follows

1- The BWO generated mode was not only a TM_{01} mode, but also other modes were generated simultaneously.
2- The discontinuity between the SWSs caused a reflection of undesired modes, in addition to the TM_{01} mode, toward the output before mode conversion occurred.
3- The Bragg reflector converted only 70% of the incident TM_{01} mode to the HE_{11} mode and then reflected 95% of the HE_{11} mode.
4- Part of the unreflected TM_{01} energy (about 30%), the unconverted TM_{01} energy (less than 5%), and other higher order modes were reflected back by the cathode toward the output.
5- Since the longitudinal component of the electric field in the SWS does not generally disappear, the mode in the Bragg reflector structure was actually a

hybrid mode, HE_{11}, which comprises the TE_{11} mode and 15% of the TM_{11} mode. The Bragg reflector was designed to reflect only the TE_{11} mode and not reflect the TM_{11} mode. The TM_{11} mode propagated toward the cathode and reflected back toward the output.

Fortunately, the undesired modes have relatively small powers compared to the desired mode's power on axis. That allowed us to make most of the measurements on axis, since the TE_{11} mode is mainly there and the power of the higher order modes are off axis.

4.2.3.3. MAGIC Simulations for Field Pattern Investigation

By analyzing the mode pattern captured by the neon bulb array, one can note that there is one bright spot at the center and four less bright spots around it, as shown in Fig. 4.28.

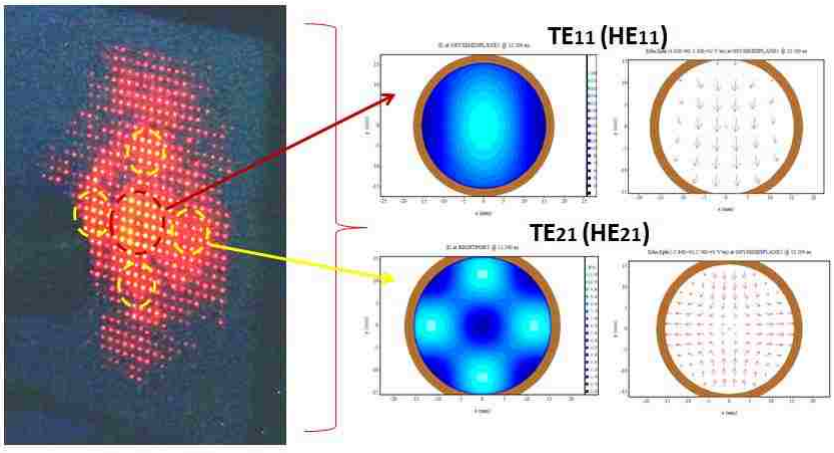

Figure 4.28 Mode pattern construction.

The center bright spot is basically the main output mode (TE_{11}) and the other four spots may be related to the TE_{21} mode. Now the question is how did the TE_{21} mode

appear?. By changing the ideal high voltage input pulse in our simulations to a more realistic looking one, a TE_{21} mode appeared, especially at lower power levels, as shown in Fig. 4.29.

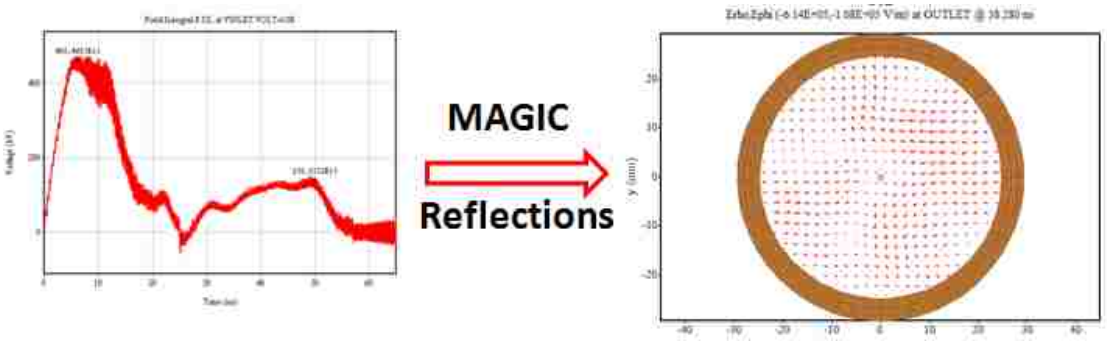

Figure 4.29 Appearance of TE_{21} at the output of RBWO with Bragg reflector when the reflections were added to the simulation SINUS-6 input pulse.

In fact, our BWO does not generate a pure TM_{01} mode as it was supposed to. By adding reflections to the input pulse MAGIC simulations showed that the generated wave is a mix of mainly a TM_{01} mode and TE_{01} mode. The TM_{02} mode was also observed, as shown in Fig. 4.30. Half of the RF output signal was a TE_{01}-like mode, which has the same energy distribution as the TM_{01} mode. That makes it difficult to recognize the existence of the TE_{01} mode by using the open-shutter photographs of the neon bulb array. The mode mixing was more severe at the output when a cutoff section was added instead of the cavity resonator reflector. This means that the cavity reflector reflected mainly the TM_{01} mode, as was expected.

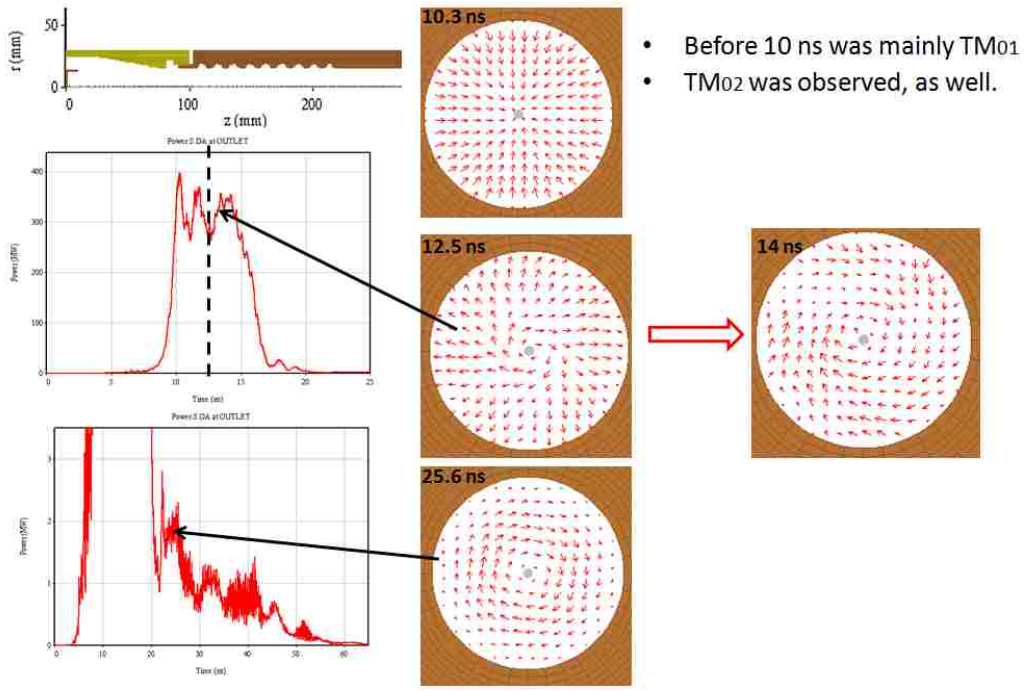

Figure 4.30 Generated mode at the output of the RBWO with a cavity resonator reflector.

The existence of the TE_{21} mode needed to be clarified analytically. Using the relations in Sec. 2.2.1., the wavenumber of the TE_{21} mode (x_{21} = 3.0542) can be found as

$$h_{TE_{21}} = \sqrt{(\frac{\omega}{c})^2 - (\frac{x_{21}}{r_0})^2} = \ 198.773\ \mathrm{m}^{-1}.$$

By using the Bragg condition (2 – 53), the difference between the Bragg axial wavenumber and the TE_{21} wavenumber is about 162.9 m^{-1} at about 12 GHz (note that these values are for a smooth wall waveguide), which corresponds to 3.832, the root of the Bessel function (or its derivative). In our experiments the diagnostics maximum bandwidth was limited to 12.4 GHz, which cannot pick up signals with a frequency content larger than 12 GHz. This value is the same as the roots of the Bessel function of the TE_{01} and TM_{11} modes (3.832), which are degenerate modes. By applying the Bragg condition of the azimuthal index (2 – 55), one can notice that there is no way for the TE_{21}

mode to be a result of the TE_{01} mode. Since the TE_{01} and TM_{11} modes are degenerate modes, there is no frequency mismatch ($\Delta k = k_{\perp TM11} - k_{\perp TE21}$), but there is a geometrical mismatch ($\Delta h = h_{TM11} - h_{TE21}$). This explains some power coupling between the TE_{01} and TM_{11} modes occurred in the Bragg structure before mode conversion between TM_{11} and TE_{21} modes took place, as shown in Fig. 4.31.

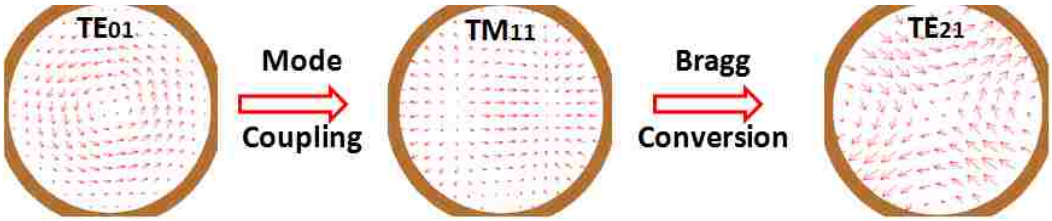

Figure 4.31 Mode coupling between the degenerate TE_{01} and TM_{11} modes and Bragg mode conversion between TM_{11} and TE_{21}.

4.2.3.4. Magnetic Field Scan

For BWO oscillators, it is important to know the region of cyclotron absorption to prevent operating the device in this region. The static magnetic field was varied by changing the current that passes through the solenoidal coils. The experimental results and MAGIC simulations show that cyclotron absorption occurs around 1.2 T, as shown in Fig. 4.32. Since the magnet circuit was modified and not calibrated, the magnetic field values were estimated and are not accurate. In addition, the magnetic field lines start flaring at the BWO region, which is not a desired situation for ideal operation. This explains the shift of the experimental data curve from the simulation one, as shown in Fig. 4.32.

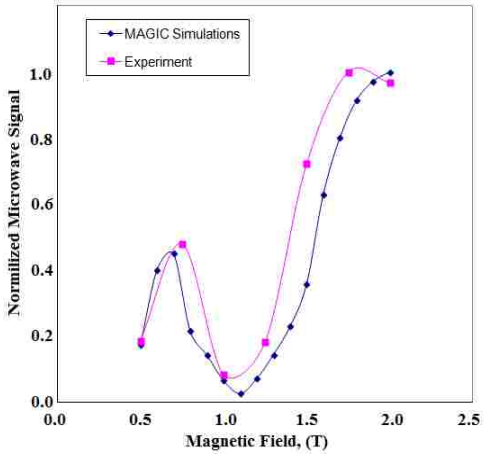

Figure 4.32 The magnetic field scan in both MAGIC simulation and in experiments.

We close this section with a brief discussion of the efficiencies achieved by our RBWO. This efficiency was obtained by comparing the product of the maximums of the input beam power to peak microwave power at 2 T magnetic field. A microwave calorimeter at UNM (Appendix) was used to measure the microwave energy, where 2.424 J was picked by the calorimeter with a 460 kV, 4.1 kA electron beam. Since the calorimeter absorbs 85% of the signal at 10 GHz, the total energy radiated by the RBWO would be about 2.85 J. Therefore, the output radiation power of 240 MW and the efficiency of about 13% were calculated from measurements. Even though the power output was a lower bound and a conservative estimate, the efficiency and the output power were generally consistent with MAGIC simulations.

CHAPTER 5. SINGLE/DUAL BAND OPERATION OF RELATIVISTIC BWO

The generation of several frequencies (in particular, two frequencies) might be beneficial for some applications such as navigation, detection of targets, electronic attack, diagnostics, sonochemical effects of irradiation, among others [101,102]. Recently, many different dual-band microwave sources have been described in the literature, although for the most part they are based on low power crystal oscillators that are used in wireless applications.

In HPM devices, multispectral (or multimoding) was regarded usually as a bad situation and the emphasis was put on the regions in the parameter space where stable single-mode operation was possible. In 1997, Dumbrajs [103] presented the first gyrotron design that oscillates stably at two different frequencies simultaneously. In 1999, Yang [104] designed a composite dual-frequency Cerenkov oscillator with T-type structure based on both a RBWO and a relativistic orotron. The two outputs were perpendicular to each other. In the case of pulsed relativistic beams, an obvious disadvantage of this scheme is the necessity of synchronizing the beams and subsequent multiplexing of the output radiation. In addition, generation of dual-frequencies in RBWOs was observed based on operation in the cross-excitation instability regime. It was limited to low efficiency and uncontrollable output frequency spectrum.

A few publications about dual band RBWOs have appeared that use sectioned electrodynamic systems (two SWSs or more) [105,106]; there is no information about the temporal distribution of the generated frequencies. Probably, as in [106], it was assumed

that they are generated independently. This might be possible in the linear regime but close to saturation even small differences can lead to suppression of a weaker competing mode [107]. In this Chapter, the design of a dual-band high power BWO is described and the results of its investigation are presented [108,109].

5.1. Dual-Band RBWO Design and Principle of Operation

To demonstrate the generation of two microwave signals with linearly polarized Gaussian radiation we choose the oscillator that consists of two BWOs with sinusoidal-profile SWSs, which is described by (2 – 1) and shown in Fig. 5.1.

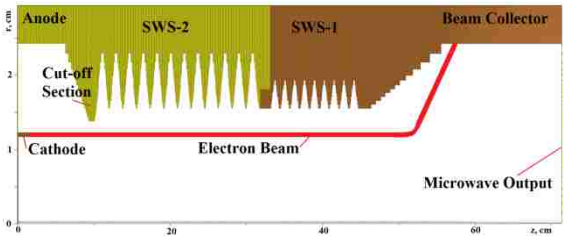

Figure 5.1 Design of an oscillator with two SWSs.

These SWSs are the SWS of the BWO and the SWS of the Bragg structure that we discussed in the previous chapters. In Chapter 3 we described a 10 GHz oscillator whose minimal radius of the Bragg structure was chosen to be significantly greater than the electron beam radius that is guided by uniform magnetic field. That was because of the concern that the Bragg reflector fields can cause unfavorable modulation of the electron beam for the operating TM_{01} mode in the BWO. In the present Chapter, however, the inner radius of the Bragg structure was chosen as the inner radius of the BWO structure, very close to the radius of the electron beam. By using this configuration interaction

between the electron beam and the two structures occurred and two microwave signals were generated. One should expect that, by increasing the number of sections, it is possible to generate linear spectra comprising a large number of individual frequencies. The generation is due to a change in the synchronism conditions which was provided by variation of the corrugation period and shape.

From now on the SWS of the BWO will be called SWS-1 and the SWS of the Bragg structure will be SWS-2. SWS-1 is an axisymmetric system whose radius is described by (2 – 1) or

$$r_{w1} = r_{0,1} + r_{1,1}\sin(\bar{h}_1 z), \qquad (5-1)$$

while SWS-2 (this system is placed on the "cathode" end of the SWS, Fig. 5.1) is a combination of left- and right-single-fold spiral corrugations that are described by

$$r_{w2} = r_{0,2} + r_{1,2}\sin(\bar{h}_2 z + \bar{m}\,\theta) = r_{0,2} + 2r_{1,2}\sin(\bar{h}_2 z)\cos(\bar{m}\,\theta). \qquad (5-2)$$

Here z and θ are the axial and azimuthal coordinates, respectively; $r_{0,1}$ and $r_{0,2}$ are the average radii in each section; $r_{1,1}$ is the amplitude of the corrugation in SWS-1 and $r_{1,2}$ is the amplitude of the each spiral corrugations in SWS-2 (for combined SWS-2 the corrugation amplitude must be doubled, as shown in (5 – 2)), and d_1 and d_2 are the axial periods of corrugation. The parameters of SWS-1 are chosen to be the same as for the SWS described in Chapter 3, while the parameters of SWS-2 were chosen to be different from the SWS described in Chapter 3; these parameters are summarized in Table 5.1. The operating points of both SWSs on the corresponding dispersion characteristics are displayed in Fig. 5.2.

Table 5.1 The periodic structures dimensions.

Quantity	**SWS-1**	**SWS-2**
Average Radius, r_0	1.74 cm	2.28 cm
Corrugation amplitude, r_1	0.19 cm	0.366 cm
Axial period, d	1.3 cm	1.8 cm
Number of periods, N	9	12
Azimuthal index, m	0	1
Pitch angle, ψ	0	7.124^{o}

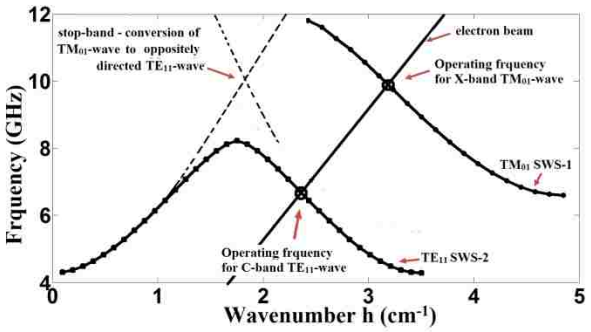

Figure 5.2 Dispersion characteristics of synchronous operating waves for SWS-1 and SWS-2.

For SWS-1, the synchronous interaction of electrons with the first negative spatial harmonic of the operating backward TM_{01} mode at frequency 10 GHz takes place when the applied voltage is U = 460 kV (γ = 1.9), as shown in Fig. 5.2. SWS-2 fulfills two functions: at 10 GHz it serves as a Bragg reflector that converts the backward TM_{01} wave to a linearly polarized forward TE_{11} mode, as was described in Chapter 3. At 7 GHz this operates as a BWO in which the operating TE_{11} mode is synchronous with the same electron beam. The slow space-charge wave of the electron beam interacts with the -1st spatial harmonic of the TM_{01} operating wave for SWS-1, while it interacts with the -2nd

spatial harmonic of the TE_{11} operating wave for SWS-2. For a sufficiently large detuning, such a configuration of the interaction space makes possible the generation of noise-like chaotic signals. The Cerenkov synchronism condition for both SWSs can be written as

$$\omega_0 \approx h_n v_0; \quad h_n = \begin{cases} h_z - \bar{h}; \text{ for SWS} - 1 \ (\mathrm{TM}_{01} \text{ mode}) \\ h_z + \bar{h}; \text{ for SWS} - 2 \ (\mathrm{TE}_{11} \text{ mode}) \end{cases}. \qquad (5-3)$$

The result of this synchronism is the absolute instability and oscillations begin for both SWSs. The SWS-1 operation principle was described in Chapter 3. In the next section the operation of SWS-2 will be discussed.

5.2. RBWO with Asymmetric Mode Operation

As for all TM modes, the hybrid mode, HE_{11}, has a strong axial electric field component, which allows it to interact with the electron beam and extract energy. In order to generate the HE_{11} mode, a helically corrugated SWS-2 was designed [109]. It should be pointed out here that SWS-2 was not originally designed to operate as a BWO, but rather as a Bragg reflector. The strong interaction between SWS-2 and the electron beam was observed, and the HE_{11} mode was generated. Even though the helically corrugated SWS-2 was not optimized to operate as a stable RBWO oscillator, it apparently was able to.

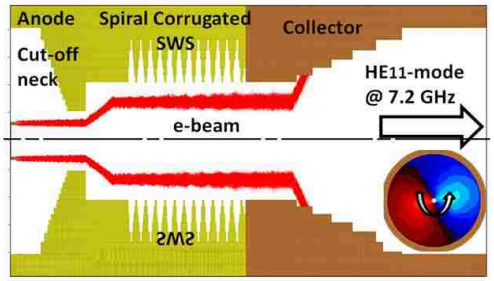

Figure 5.3 RBWO with a cutoff section and magnetic field decompression.

The generated HE_{11} mode, near the region of cyclotron absorption, propagates in the direction opposite to the electron beam streaming and is at C-band (7.1 GHz). To extract the operating mode axially a cutoff neck reflector must be used. A cavity reflector has been widely used to reflect the operating $TM_{0\rho}$ mode to overcome the disadvantages of the cutoff neck reflector. However, the cavity reflector cannot be used here because the surface current paths of hybrid modes and $TM_{0\rho}$ modes are different.

Using a surface current perturbation approach, one can explain the use of cavity resonator reflectors in BWOs operating in $TM_{0\rho}$ modes. Since $TM_{0\rho}$ modes have surface current components in the longitudinal direction only (see, for example, the TM_{01} mode in Fig. 5.4), the cavity resonator reflector is everywhere transverse to these current lines. As a result, the cavity resonator reflector acts as a short circuit and reflects most of the microwave energy. If an H-wave, such as the TE_{11} mode, is generated instead of the TM_{01} mode in a BWO, the cavity reflector cannot reflect most of the microwave energy. The interpretation of this is that the H-waves have surface current components in both axial and azimuthal directions. For instance, the linearly polarized TE_{11} mode has left- and right-hand surface current paths, while the circularly polarized TE_{11} mode has one of these paths. The cavity resonator perturbation is not transverse to these helical paths

everywhere. In addition, The HE_{11} mode not only has one/two helical paths of the surface current, but also has a longitudinal component, as shown in Fig. 5.4. We should mention here that the TE_{11} mode and HE_{11} mode will be used interchangeably in subsequent Chapters since they have almost the same field distribution [110]. The only difference is that there is a strong longitudinal component of the electric field for the hybrid mode, HE_{11}, while there is none for the transverse electric modes (TE modes).

For the HE_{11} operating wave, the cavity resonator reflector reflects different field components with different reflection coefficients and different phases. The resultant mode will have a complicated pattern and the reflected power will be small due to destructive interference.

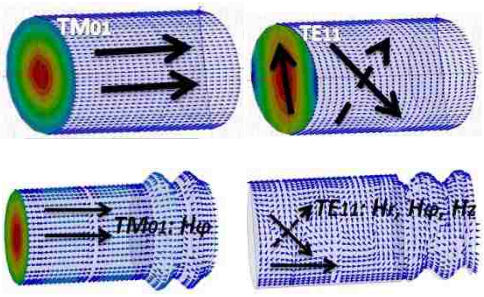

Figure 5.4 Lines representing surface currents for both the TM_{01} mode and the TE_{11} mode.

In our simulations, the RBWO is driven by an input voltage pulse that is a flat-top pulse of 460 kV with 1 ns risetime and 25 ns duration. An annular cathode produces an electron beam (2.35 kA) with R_{cath} the outer radius and t_{cath} its thickness, as shown in Table 5.2. Both uniform and nonuniform (magnetic field decompression of the electron beam) magnetic fields with peak value 2 T are used to guide the electron beam inside the tube.

Table 5.2 The annular cathode dimensions.

Quantity	Uniform Magnetic Field	Non-niform Magnetic Field
Cathode radius, R_{cath}	1.35 cm	0.822 cm
Cathode thickness, t_{cath}	0.051 cm	0.051 cm

From MAGIC simulations, about 100 MW microwave power was measured at the output when a cutoff section was used with left-hand, right-hand spiral corrugations, or both spiral corrugations, as shown in Fig. 5.5. The microwaves generated at 7.2 GHz have a very clean HE_{11} pattern, as shown in Fig. 5.6.

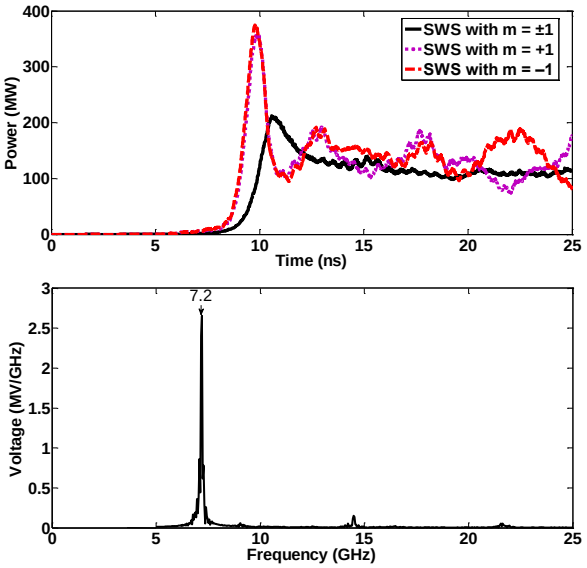

Figure 5.5 The output power (top) and the output signal FFT (bottom) from a RBWO with a cutoff neck reflector.

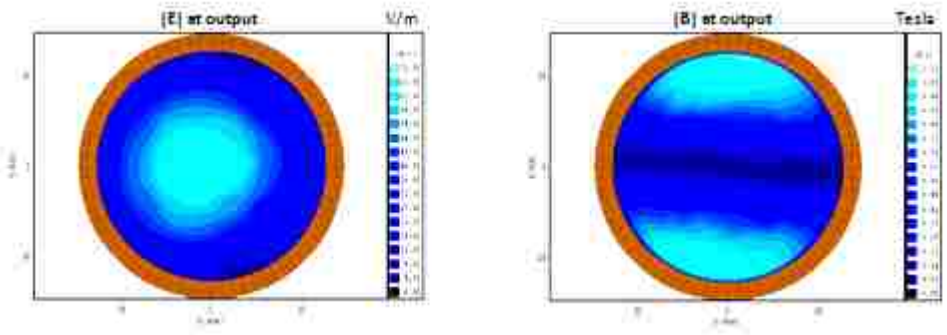

Figure 5.6 The amplitude of the output electric and magnetic fields.

5.3. Single/Dual Band TE_{11} Mode Radiation from a RBWO in a Uniform Magnetic Field

To demonstrate the dual band properties of the BWO, we performed computer simulations using MAGIC. This oscillator radiates the TE_{11} mode (Fig. 5.7) with output power 150 MW in X-band and 130 MW in C-band (Fig. 5.6) when the applied voltage is 460 kV.

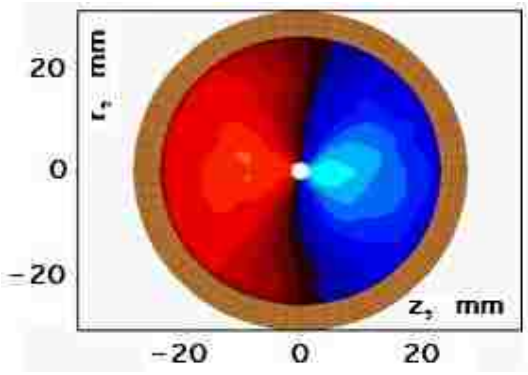

Figure 5.7 Structure of the radial component of radiated electric field.

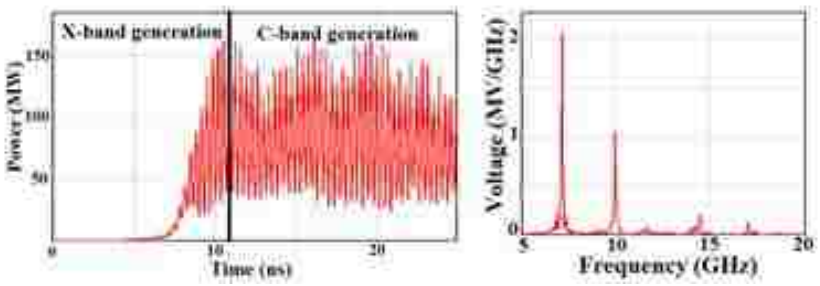

Figure 5.8 Output power and spectra for both frequency bands generated.

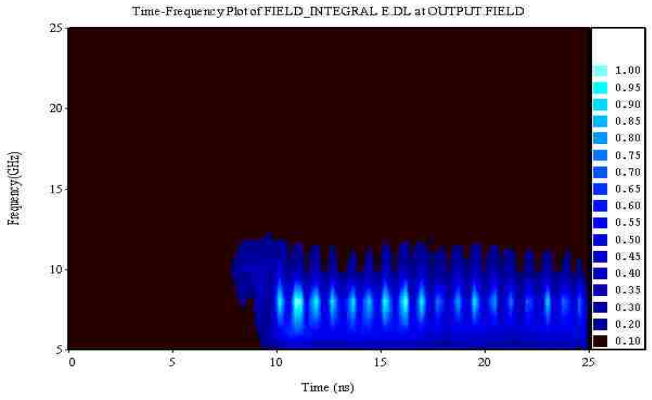

Figure 5.9 Time-frequency plot for C-band and X-band.

We found that C-band generation appears after X-band generation. This can be explained by the proximity of the operating current to the start current for this mode in SWS-2, which causes a delay in generation (Fig. 5.8 and Fig. 5.9), whereas fast starting X-band generation is provided by the operating current significantly exceeding (2-3 times) the start current for SWS-1. In addition, higher power C-band generation suppresses X-band generation. Since C-band generation is more intense, suppression of X-band generation is a consequence of mode competition. The suppression of SWS-1 generation can also be explained by a depression in electron energy caused by SWS-2. This gives the possibility to control the duration of generating different frequencies within the microwave pulse by changing the operating current (Fig. 5.10). The lower the

operating current, the later that C-band generation starts and the longer is X-band generation, as depicted in Fig. 5.10.

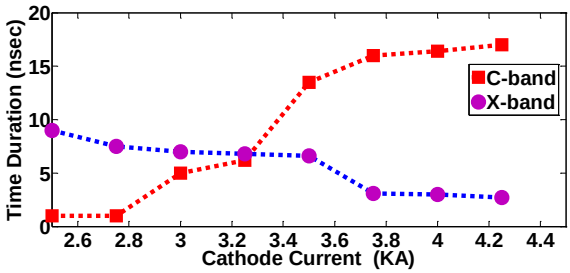

Figure 5.10 The duration of 7 GHz and 10 GHz generation is controlled by the electron beam current.

This oscillator is capable of radiating a Gaussian microwave beam not only for fixed frequencies, but also across a range of frequencies. Frequency tuning can be achieved by changing the interaction of cyclotron waves of the electron beam with the fundamental spatial harmonic of the operating wave, which is realized by choosing the guide magnetic field to be close to the resonant value, as shown in Fig. 5.11. That can be achieved for both bands by changing the magnetic field near the region of cyclotron absorption (RCA). Thus, as a whole, 6% frequency tuning for both C-band and X-band is achievable.

The RCAs of the X-band BWO with SWS-1 and the C-band BWO with SWS-2 (Fig. 5.11) do not overlap at different frequencies. That gives the opportunity to achieve single frequency generation at different values of the uniform guide magnetic field.

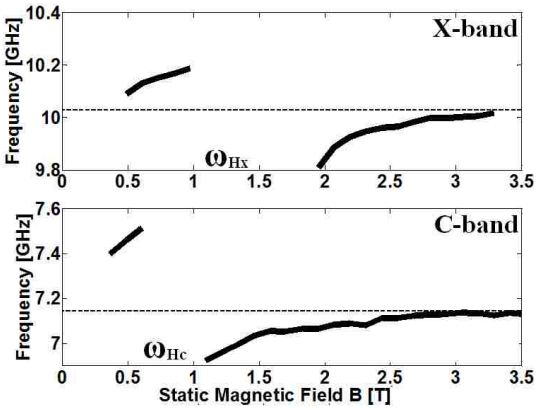

Figure 5.11 Dependencies of frequencies of generation on the guide magnetic field demonstrating frequency tunability.

5.4. Single/Dual Band TE_{11} Mode Radiation from RBWO in a Nonuniform Magnetic Field

A nonuniform magnetic field can also be used to generate single frequency output from sectioned electrodynamic systems. In Chapter 3 it was shown that single mode generation is provided when fields of the Bragg reflector do not interact with the electron beam. This takes place when there is a large radial gap between the reflector and electrons. The large gap can be provided with magnetic decompression (Fig. 5.12) of the electron beam [12,109] in order to only generate 10 GHz (Fig. 5.13). In common, the nonuniform magnetic field can be used in order to increase the gap between the electron beam and any SWS section to weaken the interaction of the electromagnetic field with the electron beam.

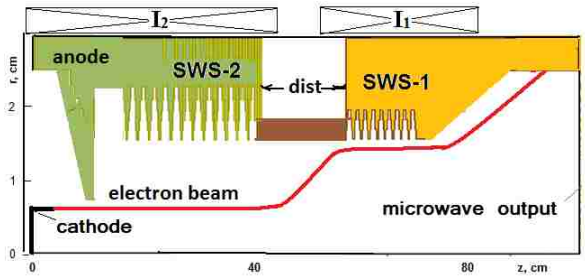

Figure 5.12 BWO design with magnetic decompression of the electron beam. The current in the coils are not the same ($I_2 > I_1$).

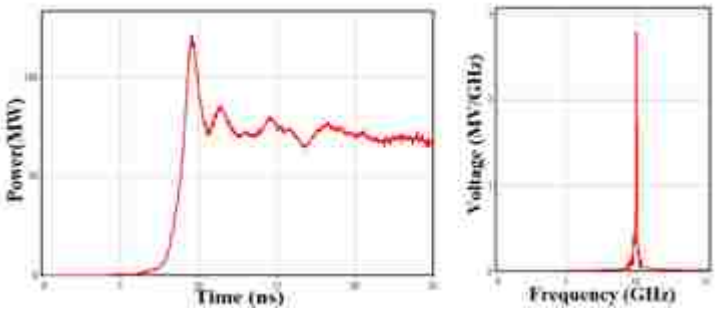

Figure 5.13 X-band power generation and FFT of the microwave signal from a RBWO with magnetic decompression of the electron beam.

For X-band generation, the radial gap between the electron beam and SWS-2 can be increased by increasing the current in the solenoid (I_2) to allow for the interaction between the electron beam and SWS-1 alone. In this case, SWS-2 acts solely as a Bragg reflector.

For only C-band generation the electron beam propagates close to SWS-2, which operates as a BWO with the operating TE_{11} mode, whereas the gap between the electron beam and SWS-1 must be large, as shown in Fig. 5.14. However, even with a uniform magnetic field, single mode C-band generation is possible with sufficient distance "dist" between SWS-1 and SWS-2, when SWS-2 operates as a BWO as well. The dependence of C-band signal frequency on distance between the SWS-2 and the reflector is shown in Fig. 5.15.

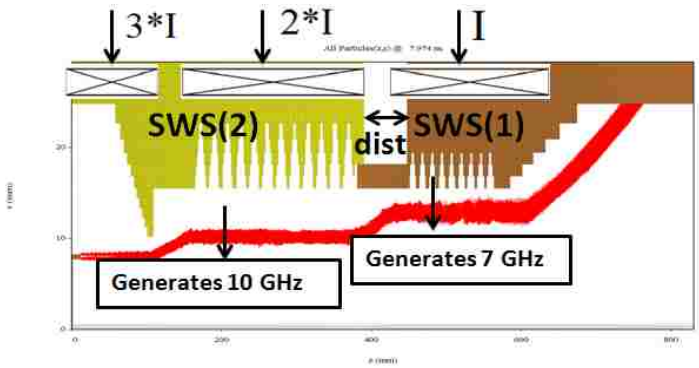

Figure 5.14 Use of an axially nonuniform magnetic field to weaken the unwanted interaction.

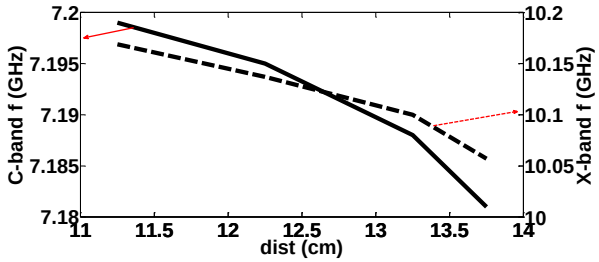

Figure 5.15 Dependence of oscillation frequency in the X- and C-band of the distance between the SWSs.

Figure 5.15 shows the dependence of X-band generation on the distance between SWSs "dist" when the Bragg reflector field's effect are weakened by a nonuniform magnetic field. This result is basically similar to changing "dist" in an earlier BWO [80,85] using a cavity as a premodulator, which also demonstrated frequency tuning.

In fact, the changing in "dist" affects the start conditions. It was shown that the oscillator start current decreases as the modulation phase increases. Since the length of the transit process [63] is $t_r \sim (1 - (I_{st}/I_b)^{1/2})^{-1/2}$, there is a possibility to change the microwave radiation pulselength of the oscillator without changing parameters of the electrodynamic system and beam current.

The device could operate independently at two different frequencies when the "dist" is sufficiently large. By slightly changing the distance between the structures, the RF

pulsewidth can be controlled. Therefore, short microwave pulses can be produced, in both frequency bands, that is useful for radar applications. Figure 5.16 shows the microwave pulsewidth controlled by the distance between the SWSs.

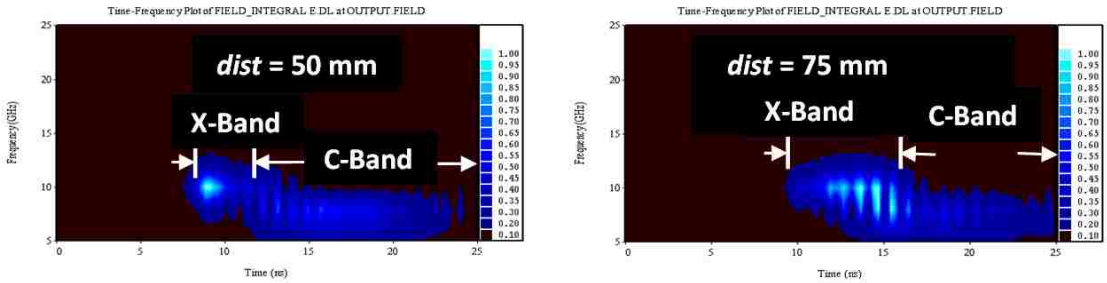

Figure 5.16 C- and X-bands signal pulsewidth as a function of the distance between SWSs.

CHAPTER 6. RELATIVISTIC BWO WITH GAUSSIAN RADIATION EXTRACTED RADIALLY USING AN ELECTROMAGNETIC BANDGAP MEDIUM

Since linear devices require a longitudinal component of the electric field to interact with the electron beam current, the RBWO typically is known to radiate TM modes in a circular waveguide. The microwave signal usually is extracted axially after reflecting the TM mode from the upstream end of the SWS by using either a cutoff neck reflector or a cavity reflector.

In order to produce a Gaussian beam from BWOs, a mode converter usually is used at the downstream end. In this Dissertation, a Bragg reflector of a circular waveguide, which was described in Chapter 3, was used at the upstream end to reflect the operating TM_{01} mode and to simultaneously convert it to a TE_{11} mode. Even though an asymmetric mode can be generated in these devices [10], a cutoff waveguide section is the only means to effectively reflect that wave for radiation. The disadvantage of the cutoff neck reflector, especially for high frequency devices, is its proximity to the electron beam. That leads to electron beam scrape-off and alignment difficulty. Because SWSs with period ~ $\lambda/2$ have been used for decades to generate HPM radiation, combining a periodic SWS with an EBG medium can improve the performance of Cerenkov devices. In this Chapter, the novel idea of combining an EBG medium with the SWS of a RBWO is used for coupling and extracting Gaussian radiation pattern. The EBG structure follows a slot antenna concept, where the slot array is cut at the SWS wall to perturb the surface currents. The slots are used for coupling between the interaction region and a concentric circular waveguide. After that, the generated wave can be radiated axially by using a horn

antenna. The EBG structure makes the BWO more compact and allows for more power to be extracted, not only for asymmetric modes but for symmetric modes as well.

TE modes in periodic structures always have an axial electric field component. The HE_{11} mode is the fundamental mode of a circular corrugated waveguide that can be generated from different combinations of $TE_{1\rho}$ modes and $TM_{1\rho}$ modes [110]. The HE_{11} mode is a low-loss mode where the Ohmic loss is comparable to that of the TE_{01} mode, which has the lowest loss in a smooth wall waveguide [110]. At the open-ended corrugated waveguide, the HE_{11} mode couples to the fundamental free-space Gaussian mode with almost no loss over wide bandwidths. In addition, it can propagate in any polarization, from linear to circular. Its linear polarization is nearly ideal, with negligible cross-polarization at large waveguide diameters.

6.1. RBWO with Radial Extraction

In this Section, a novel way of extracting the HE_{11} mode from a RBWO is introduced. The SWS of the RBWO is loaded with an EBG medium (Fig. 6.1) to couple the generated mode to a concentric waveguide. Cold test simulations were performed using HFSS for the SWS to obtain the dispersion characteristics. The dispersion diagrams of the HE_{11} mode for the SWS with and without the EBG medium are shown in Fig. 6.2. Basically, the EBG medium is formed by cutting a very small portion of the sinusoidal peaks of the SWS envelope. The dispersion curve is not affected at the operating frequency even though the passband region is generally reduced.

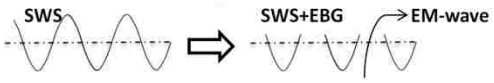

Figure 6.1 A sketch of the SWS envelope with and without EBG.

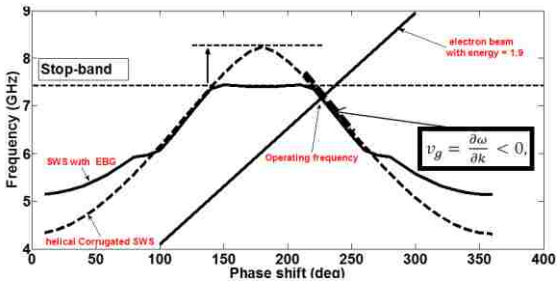

Figure 6.2 Dispersion characteristics for a SWS with and without an EBG.

The RBWO with a helical cut based EBG medium and a holes based EBG medium is shown in Fig. 6.3. The radial gap (*s*) between the outer radius of the inner structure and the inner radius of the outer structure is about 1 cm. Even though the gap has been slightly increased, the output power was insignificantly affected. In addition, the device output was extended to form a circular waveguide output, and the output results remained the same.

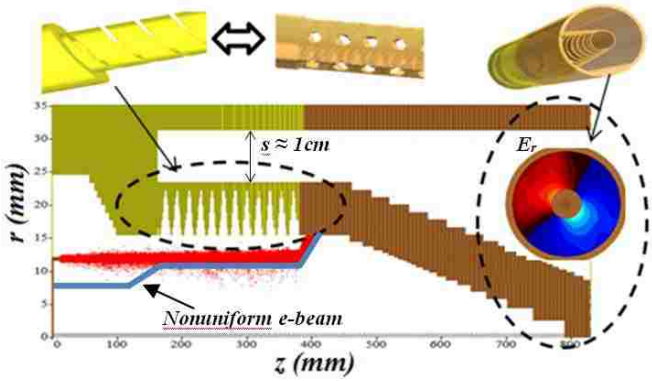

Figure 6.3 RBWO with radial extraction by using a helical slot and holes based EBG media.

The measured power and FFT of the output signal, when the helical cut based EBG medium was used, are shown in Fig. 6.4. This EBG medium was designed so that the SWS is not connected to the electron beam dump in order to avoid any resonance with the

slot length and a concentration of the current density at the ends. Due to a potential difference between the electron beam collector and the concentric waveguide, a low frequency or DC-component at the output of the RBWO was observed. The low frequency component causes the field and the power at the output to be shifted, as shown in Fig. 6.4.

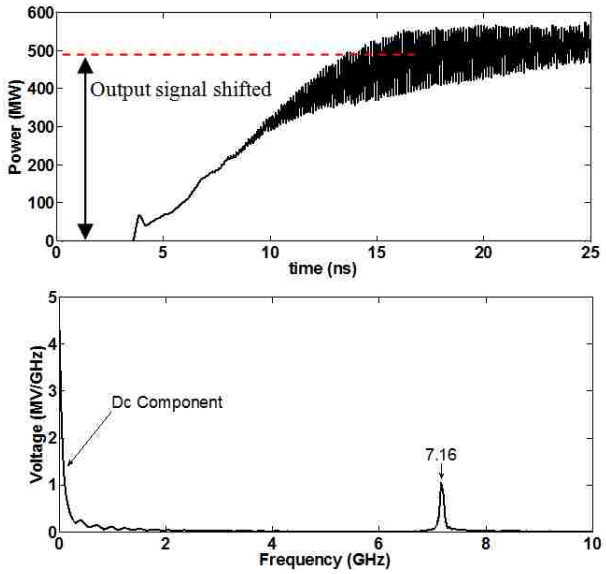

Figure 6.4 The output power for an uniform magnetic field and FFT of the RBWO with a helical slot coupling.

The helical slot based EBG medium can be considered as a uniform leaky waveguide antenna. Generally, a uniform leaky waveguide antenna can be replaced by periodic leaky slots with no change in performance [112,113], as shown in Fig. 6.5.

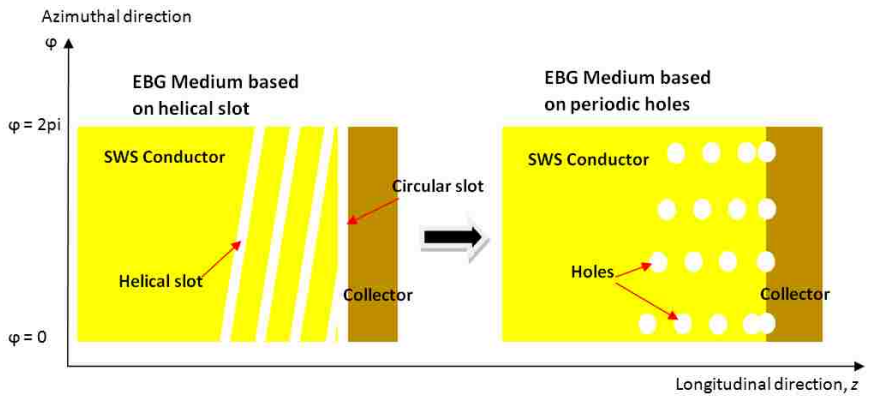

Figure 6.5 A uniform leaky waveguide antenna was replaced by periodic leaky slots.

Given this replacement, the output power and the FFT of the output microwave generation for both uniform and nonuniform guide magnetic fields are shown in Fig. 6.6.

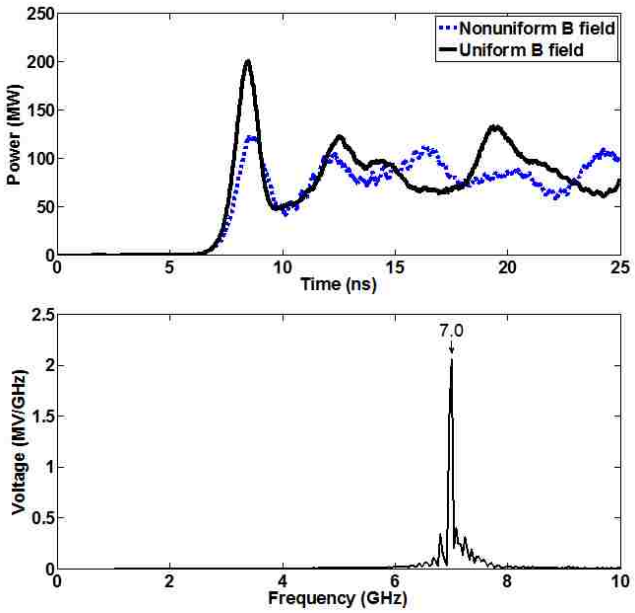

Figure 6.6 The output power and FFT of the RBWO with circular slots coupling.

One can notice that the RF power is fluctuating (Fig. 6.6), which means the RBWO does not provide stable performance. The fluctuation of the power is attributed to two reasons:

1- Unstable operation of the BWO, which is due to:

i. the SWS of the RBWO not being designed to operate as a BWO, instead it was designed as a Bragg reflector [109]. It has been used just to prove the the idea of using an EBG medium with a SWS.

ii. the electron beam current (2.35 kA) is not 2-3 times greater than the start current (1.35 kA), which is required for stable BWO operation.

2- The second reason is that the holes are not located at the same current density amplitude and phase. Therefore, the surface current perturbation is different from one hole to another. Unfortunately, MAGIC is not capable of showing the surface current density distributions in order to optimize the positioning of the holes.

Comparing Figures 5.5 and 6.6, one can notice a smaller time delay of the output signal when an EBG medium was used instead of the cutoff section. The fast signal extraction can be considered a reduction of the pulse-shortening phenomenon, which is very important when a very short voltage pulse, such as SINUS-6 pulse, is used. In addition, if we compare the FFT of the RBWO with and without the EBG medium, we see a slight difference of the output frequency. This is due to the EBG medium interacting with the electron beam. Meshing can play an important role in this matter as well. For further investigations, the magnetic field scan has been performed from 1.2 T to 2.2 T for both cases where more interaction was observed at lower magnetic fields. As the magnetic field scan was performed, the frequency tuning of this device was about 200 MHz around the operating frequency.

6.2. Cutoff Mode Extraction

The cutoff section is added here to show that greater power can be extracted through the EBG structure where the wave is trapped, as shown in Fig. 6.7. For different reasons [114-116], a microwave device with a below cutoff mode as an operating wave might be desired. A cutoff mode can be generated using metamaterial structures in several microwave devices [114]. The great challenge, in this case, is the extraction of the below cutoff mode where the wave is trapped inside the waveguide. The concept of the EBG medium is based upon surface current perturbation and can be used to extract even a cutoff mode.

This method is suitable to extract both backward/forward waves, and for propagating/cutoff modes. Furthermore, the EBG medium can be used to extract the forward and backward propagating mode like that generated in orotrons. In both cases, the group velocity is close to zero, which allows for greater energy extraction from accelerated electrons.

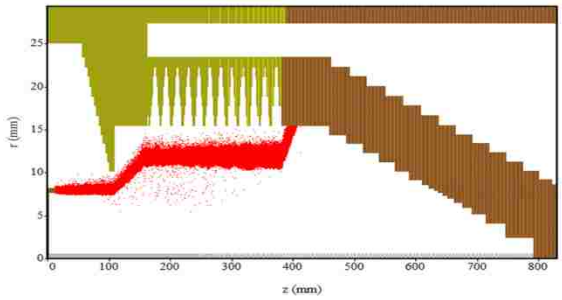

Figure 6.7 The RBWO with EBG medium design for cutoff mode devices.

6.3. Physics of the Electromagnetic Bandgap Medium

The EBG medium is a cut on the waveguide's wall, which can take different shapes. The magnetic coupling employed by slots at the waveguide wall can be interpreted as a slotted waveguide antenna. The slot couples the wave to a concentric waveguide only if the slot cuts across surface current lines corresponding to the waveguide's mode. Surface currents on the wall of the waveguide flow with different paths for different modes. This is due to the field structure of the waveguide's mode; these field structures are generally different. The direction of the surface current (*J*) depends on the magnetic field vector (*H*) of the mode, and related by

$$\bar{J} = \hat{n} \times \bar{H}, \qquad (6-1)$$

with

$$\hat{n} = \begin{cases} \hat{r}; & \text{a smooth wall waveguide} \\ \hat{r}\ \dfrac{dr_w}{dz} + \hat{z}; & \text{a corrugated waveguide} \end{cases}$$

where $\hat{n}$ is the unit vector perpendicular to the waveguide inner wall, r_w is the corrugated profile (2-1) of the waveguide inner surface, and $\hat{r}$ & $\hat{z}$ are the unit vectors in the radial and longitudinal direction, respectively.

For coupling between the waveguide mode and free-space, an antenna designer needs to be careful about different parameters, such as slot dimensions, slot spacing, and waveguide termination. Fortunately, in this EBG medium design, these restrictions can be avoided or relaxed for different reasons, which are explained below.

For an antenna design, all dimensions of the slot must be small compared to the wavelength, so the phase variation across the slot and the side lobes can be neglected

[117]. However, for the EBG medium, slots need not be small since the coupling will be between two concentric waveguides. Thus, the energy of the main and side lobes is contained inside the outer waveguide, which will shape the mode.

In the waveguide slotted antenna design, the slots are spaced by exactly one wavelength (resonant wave slot array) and are less than or greater than the wavelength (traveling wave slot array). Proper choice of the slot spacing depends on the feed end and the desired radiation pattern [117]. For the EBG medium, the wave is generated inside the structure (no feed end); thus, more degrees of freedom are available for the slot spacing. In addition, the corrugation on the waveguide's inner surface is similar to filling the waveguide with a dielectric for the guide's wavelength reduction.

Finally, an unmatched load at the termination end of the antenna increases reflections and the side lobes due to the power traveling toward the feed end. Since the EBG medium is an array which is duplicated around the circumference of the waveguide, neither slot spacing by a wavelength nor the waveguide termination as a matched load are required [118].

In principle, the leaky waveguide antennas leak the power continuously as the wave propagates on the guiding structure with a phase constant less than the free space wavenumber. Since the phase velocity is greater than the speed of light [112,113], these antennas are perfect for coupling between waveguides. The helical slot, which was used as a first EBG medium design, is basically a proper opening of a waveguide structure. This allows the energy to be leaked near the SWS outer wall. Since the output signal was mixed with a DC component, the helical slot was replaced by periodic slots. Even though the reason for replacing a uniform slot (helical slot) with periodic slots (holes) in antenna

design problems [112] was different from the reason considered here, the effect on the waveguide field distribution is the same. When the periodic slot spacing is about $\lambda/2$ and its diameter is less than $\lambda/4$, the helical slot and the periodic holes behave similarly – they extract the same power from the interaction region. In addition, because the periodic slots can be approximated as small apertures, and the spacing is less than a half wavelength, none of the modes except the lowest order H-mode can be coupled to the concentric waveguide. Even though the periodic slots can take any shape, circular holes were chosen since less metal is cut away and there is less loss of mechanical strength. Furthermore, these slots are practically simpler to machine since the areas are drilled rather than cut away from the conductor.

6.4. EBG Medium Replacing the Cavity Resonator Reflector

Using a surface current perturbation approach, the physics of the cavity resonator and the cutoff section reflectors were explained. As mentioned earlier, the use of a cavity resonator reflector in BWO devices is effective to reflect modes that have a surface current component in the longitudinal direction only. On the other hand, the use of the cutoff neck reflectors has the disadvantage of electron beam alignment difficulty, even though it can reflect any mode pattern.

Because of the disadvantage of the cutoff section and cavity resonator, the EBG medium was proposed to replace them. The EBG medium can extract any propagating and cutoff mode by properly perturb the surface current component of the operating mode. The extracted mode pattern and polarization could be the same as the operating mode or they could be different dependent on the shape and the location of the slots with

respect to each other. This means that the EBG medium can be used as a polarized mode converter as well.

CHAPTER 7. POWER COMBINER FOR HIGH POWER CERENKOV DEVICES

Power handling in a single HPM source is limited by material technology and breakdown. If it is desirable to generate coherent microwaves with power greater than can be obtained from a single HPM source, microwave beam combining of the output of several HPM sources can be a solution. Increasing the peak output power of the microwave pulse with a Gaussian beam is very important for many applications [1,79]. One promising way to increase microwave power is by summing the output radiation from several microwave sources by using either an antenna array or a waveguide structure. Summing the power from several microwave oscillators connected in parallel to a single pulser leads to coherent summation as long as the difference in phase is <25% when a fast rising voltage pulse is used [119,120].

Recently, an experimental study of power summation from two RBWOs where in each oscillator a gigawatt output power radiated at gigahertz frequency was demonstrated [119-121]. The coherent summation of fields radiated by their horn antennas was verified by the imaging of the expected interference pattern.

Coherent and incoherent microwave summation in waveguide structures has been investigated for a long time. Rectangular waveguide structures with the fundamental TE_{10} mode were successfully used to combine HPM sources without experiencing breakdown [122-125]. Circular waveguide structures were also proposed [126-129] for efficient field summation. Some of these structures used a circular waveguide operating in the fundamental TE_{11} mode as in [124]. Others used a rectangular waveguide structure with

circular to rectangular waveguide coupling where the TE_{11} circular waveguide mode couples with the TE_{10} rectangular waveguide fundamental mode.

In general, standard waveguides suffer breakdown at high power levels and oversized waveguides raise the risk of exciting higher order modes. Therefore, a controlled mode conversion and coupling can be a possible solution to combining and handling high microwave power level in oversized waveguide structures. Combining lower order modes to a higher order mode is suggested for the first time in order to overcome the limitation of the RF breakdown issue.

In this present work, our goal is to combine the output power of two or more RBWOs driven by a single high current electron beam accelerator. The T-junction suggested, in Sec. 7.2, comprises two TM_{01}-TE_{11} serpentine mode converters [130] with a common output, as shown in Fig. 7.1. Furthermore, *N* serpentine mode converters were used to design an *N*-way microwave power combiner (Sec. 7.3)

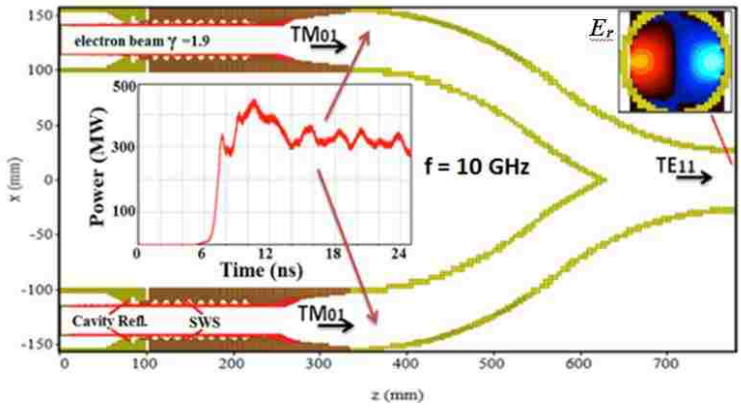

Figure 7.1 Two RBWOs with a cavity resonator reflector to provide two input TM_{01} modes for the power combiner.

7.1. Serpentine Mode Converter

The serpentine mode converter that is described here has been designed at UNM to convert the TM_{01} mode of an X-band RBWO to the TE_{11} mode. This type of mode converter is very efficient and widely used [131]. The serpentine structure profile is usually approximated by a 5rd order polynomial as

$$r(z) = \frac{R\,z}{2L^3}\,(2L^2 - 4\,z^4), \qquad (7-1)$$

where the waveguide bend is along the z-axis and *R*, *L* and the serpentine converter's dimensions are shown in Fig. 7.2.

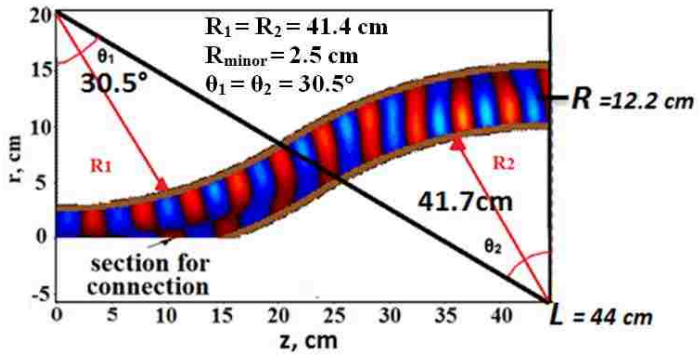

Figure 7.2 Radial electric field in the serpentine mode converter.

Coupled wave theory is widely used to understand and calculate mode conversion inside curved waveguides, which can be described by

$$\frac{dA_x(z)}{dz} = i\,h_x A_x(z) + i\sum_{x=1}^{N,x\neq y} C_{xy}(z)\,A_y(z), \qquad (7-2)$$

where $A_{x,y}$ and $h_{x,y}$ are the field amplitude and the wavenumber of x and y waves, respectively. The coupling coefficient ($C_{x,y}$) for any mode in a smooth wall waveguide due to parameters, such as diameter change and curvature are given in [132].

Using coupled wave theory (7 – 2), the field amplitude in the mode converter is calculated and can be plotted as a function of the structure length to show how the input wave decays and the converted wave grows. In addition, HFSS simulation results of the amplitude of the electric field agree with the theoretical one, as shown in Fig. 7.3.

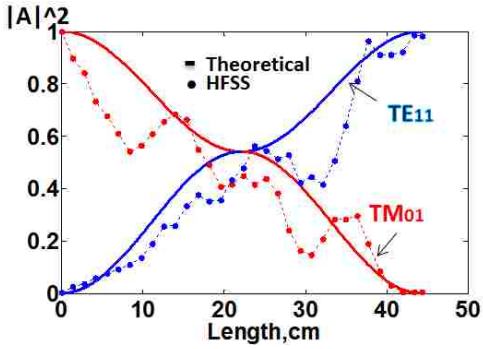

Figure 7.3 The field amplitude along the mode converter when TM_{01} is the input mode.

This mode converter not only converts the TM_{01} mode to the TE_{11} mode, but also converts a linearly polarized TE_{11} mode back to the TM_{01} mode. The electric field vector at the input of the converter must be in the plane of the waveguide bend for TE_{11} to TM_{01} conversion. Otherwise the TE_{11} mode will propagate toward the output, as can be observed in Fig. 7.4. The conversion efficiency of the serpentine mode converter is about 95% for conversion between the TM_{01} mode and the TE_{11} mode, as shown in Fig. 7.4 and proven in [128].

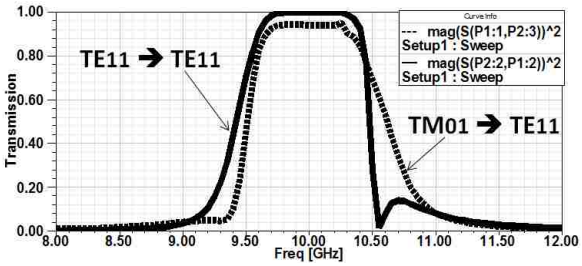

Figure 7.4 The transmission coefficient when the input TE_{11} mode is parallel and perpendicular to the plane of bend.

7.2. Two-Channel Power Combiner Design and Simulation

The proposed power combiner comprises two serpentine mode converters. For combining the power of two RBWOs, it is convenient to connect two mode converters along the connection section to form the common output cylindrical waveguide. The two microwaves with Gaussian beams are combined at the intersection region of the mode converters. This device not only combines the microwave power, but is also converts the input mode to a more desirable output mode.

The sources are driven by the same high voltage accelerator to prevent phase difference. Two 460 kV X-band RBWOs are used to provide the power combining of two operating TM_{01} modes. The input voltage pulses have identical very fast risetime (1 ns) to prevent phase difference, which can negatively affect the summation. Practically, this can be achieved using a biased ferrite coaxial transmission line, as described in [120]. When the input power of the power combiner is about 350 MW, the measured combined power is about 600 MW (Fig. 7.5 left) at their identical frequencies f = 10.1 GHz.

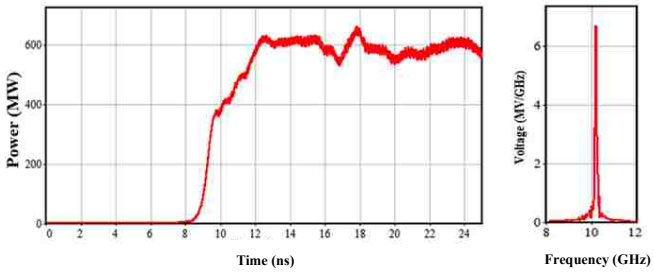

Figure 7.5 X-band power as a function of time and FFT of power combiner output.

As shown in Fig. 7.6, the output mode is the TE_{11} mode for the TM_{01} input mode. In contrast, for a serpentine mode converter, when two TE_{11} modes are combined, the output is a TM_{11} mode with a very small fraction of the TM_{01} mode. Since for many applications it is required to have the microwave energy concentrated on-axis, the TM_{11} mode can be

converted to the HE_{11} mode using a corrugated waveguide section as in [131]. In both TM_{01} and TE_{11} input cases, the power conversion efficiency is about 42%, where 50% is the maximum efficiency for a two-channel power combiner without losses. The two input modes are constructively interfering at the common waveguide output and combined, as shown in Fig. 7.8. When the input waves are TE_{11} modes perpendicular to the bend plane, the wave will couple equally to TE_{n1} modes (TE_{01}, TE_{11}, and TE_{21}).

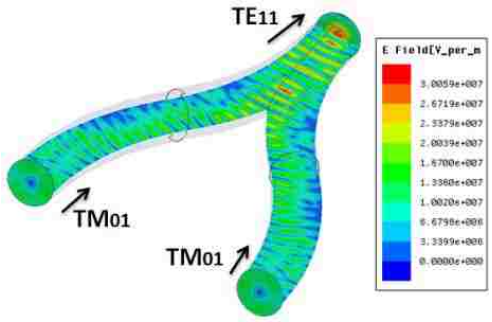

Figure 7.6 The electric field distribution when the TM_{01} mode is used as the input.

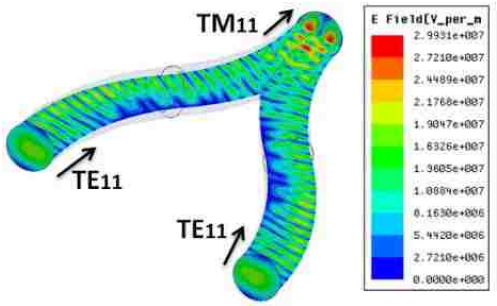

Figure 7.7 The electric field distribution when the TE_{11} mode is used as the input.

The coupling between the input channels can have a negative effect on the HPM source's performance. The coupling between channels can reduce the efficiency of HPM generation and cause intermodulation. For both TE_{11} mode and TM_{01} mode input at one input channel, the coupling to the other input channel is less than 10% for all output modes. The coupling can be further reduced by using a grid of wires or inserted plates for the TE_{11} mode case as an input mode.

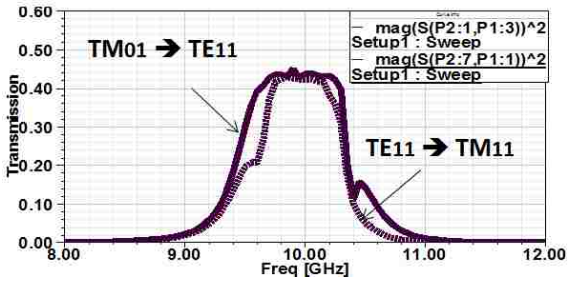

Figure 7.8 The transmission coefficient TE_{11} mode and TM_{01} mode input cases.

7.3. *N*-Way Microwave Power Combiner

The Wilkinson *N*-Way microwave combining structure sums the power of *N* devices with very high efficiency [133,134]. This technology sums power from *N* semiconductor sources to obtain <1 kW of microwave power. That is limited by thermal energy and by the use of a heat sink. Even though waveguide combiners had been suggested, a standard waveguide operating in the fundamental mode was used. The standard waveguide suffers breakdown at less than megawatts microwave power level. Therefore, the limitations are no longer the power-limiting factor of the combiner; rather, the breakdown voltage of the combiner transmission lines determine its ultimate power handling capability. To solve this issue, an overmoded waveguide can be used which can handle a gigawatts of power if properly designed.

In this section, an *N*-way microwave power combiner for HPM applications is proposed and simulated based on a serpentine mode converter. For a serpentine mode converter, the electric field vector at the input of the converter must be in the plane of the waveguide bend for TE_{11} to TM_{01} conversion. Otherwise the TE_{11} mode propagates toward the output without conversion, as shown in Fig. 7.4. The TE_{11} input modes are injected in the plane perpendicular to the waveguide bend plane. In the first design, four serpentine

waveguide sections are connected to a large (oversized) circular waveguide section, as shown in Fig. 7.9. This allows for greater powers to be handled without suffering breakdown.

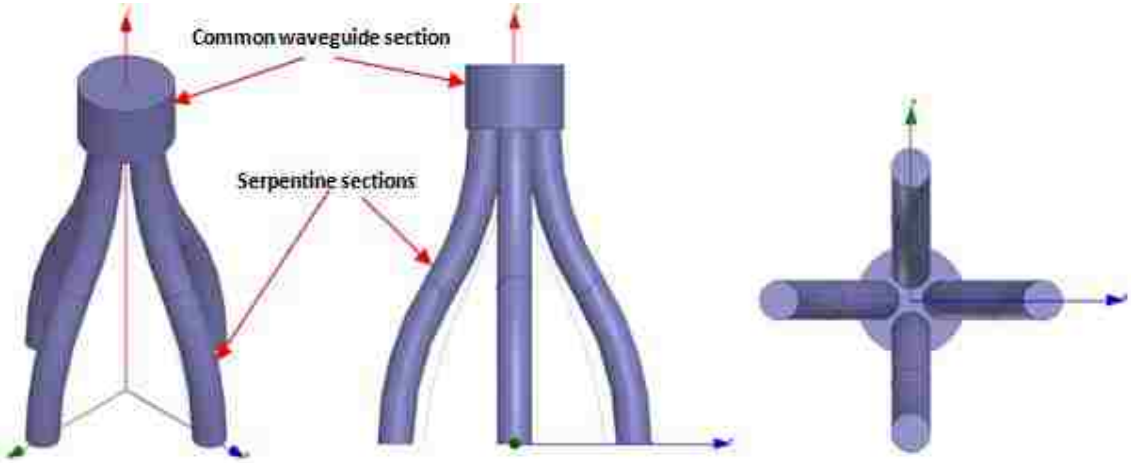

Figure 7.9 4-way power combiner based on four serpentine mode converters.

The maximum efficiency of a 4-way combiner/divider device is 25%. From HFSS simulations, about 22% efficiency was observed, as shown in Fig. 7.10. The TE_{11} input mode couples to a TE_{01} mode, as shown in Figs. 7.10 and 7.11.

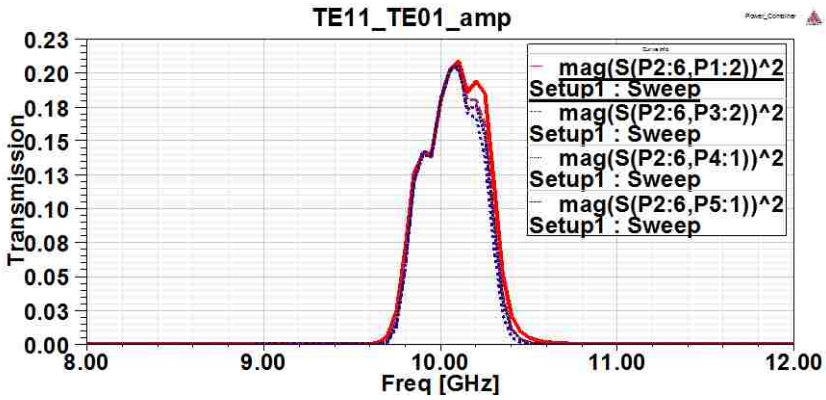

Figure 7.10 The transmission between TE_{11} input mode and a TE_{01} output mode.

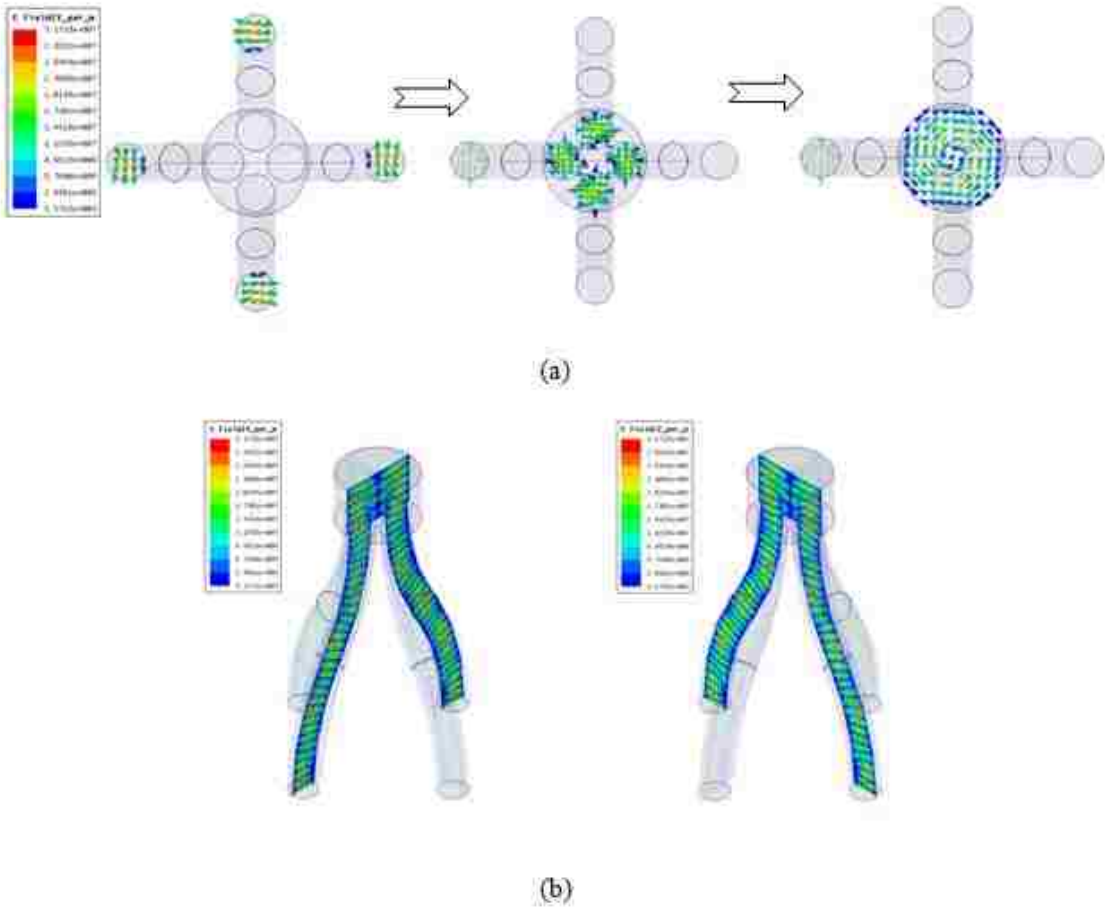

Figure 7.11 The mode pattern of the 4-way power combiner.

As the number of input channels N are increased, the output TE_{01} mode becomes cleaner and the coupling/combining efficiency reaches its maximum (12.5%), as shown in Figs. 7.13 and 7.14.

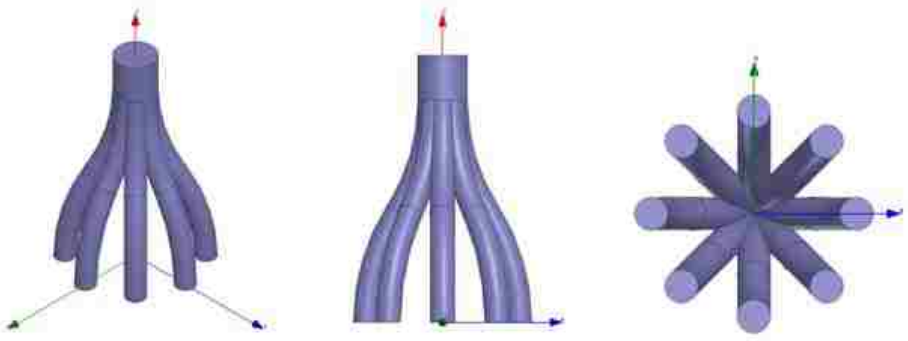

Figure 7.12 An 8-way power combiner.

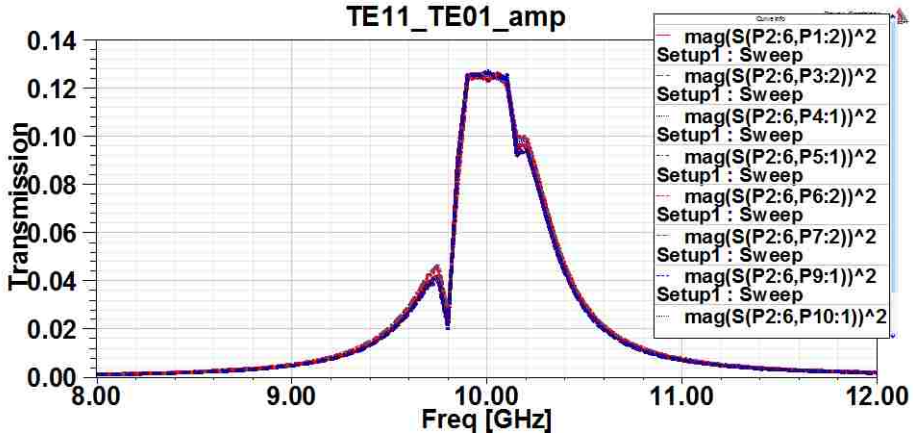

Figure 7.13 The transmission coefficient between the input TE_{11} and the output TE_{01} modes.

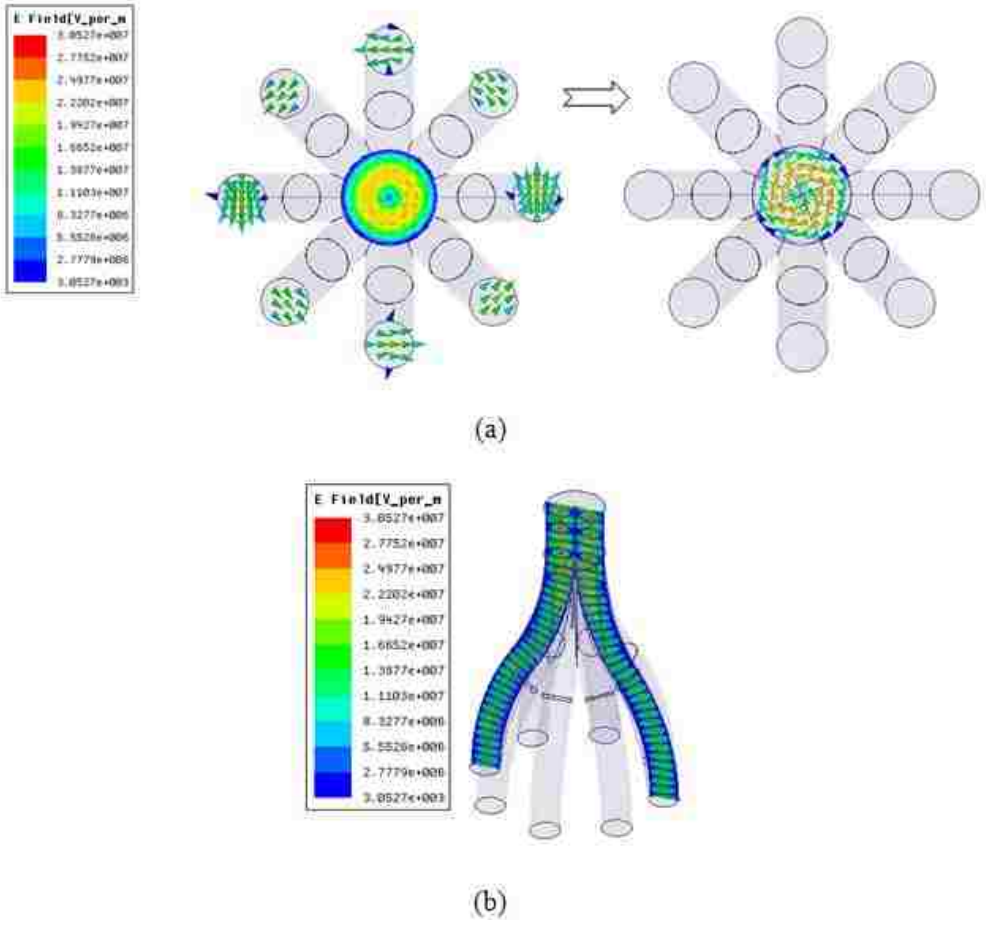

Figure 7.14 The mode pattern of the 8-way power combiner.

This concept gives the same results when the TM_{01} modes are the input and the TE_{11} modes arrive at the right phase and polarization at the input of the oversized waveguide section. In addition, the *N*-way power combiner can be achieved by enlarging the output waveguide section and *N* input channels are added at the larger diameter, as shown in Fig.7.15. The result is a TE_{0N} mode when *N* TE_{11} modes are injected. The TE_{0N} to HE_{11} mode converter can be used to produce a Gaussian beam at the output by using a proper mode converter.

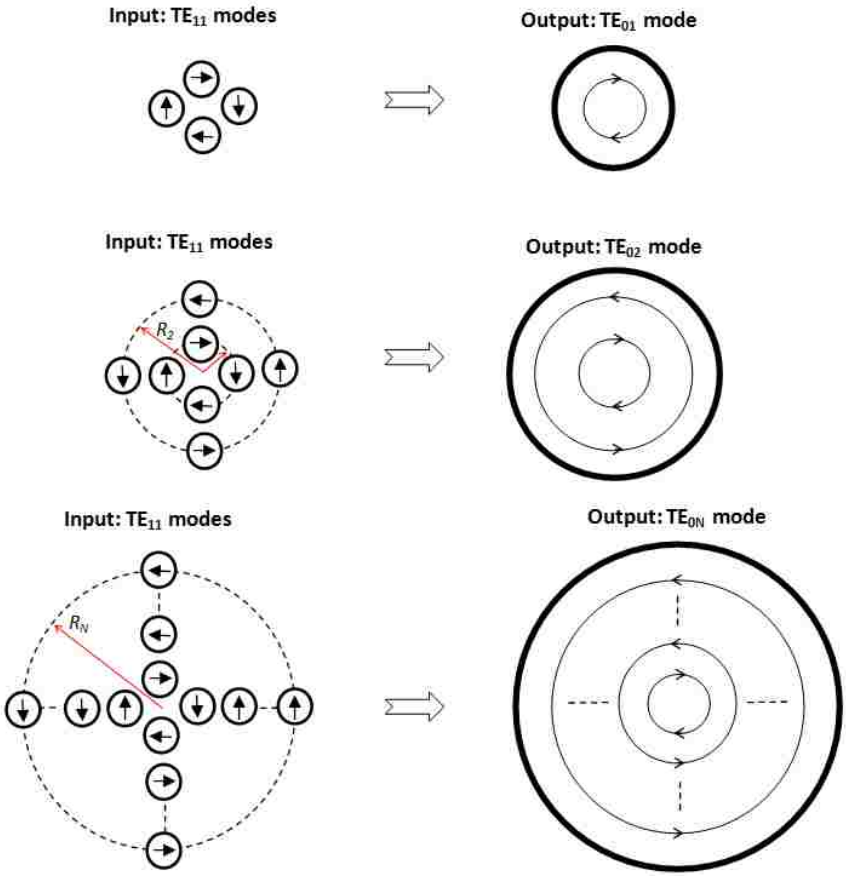

Figure 7.15 The electric field vector of the input and output field for *N*-way power combiner.

We close this chapter with a brief discussion of the electrical breakdown, which limits the power combining process. Breakdown is a serious malfunction that occurs more frequently at higher fields. In general, two breakdown limitations exist. The average power causes breakdown through heating effects and the peak power causes breakdown through arcing effect (secondary electron emission or multipaction). For pulsed regime of operation, the peak power is usually the main reason of the breakdown in waveguide structures. These structures are usually pumped into high vacuum state, in which the electric field breakdown threshold is greater than 1.0 MV/cm at short microwave pulse duration (< 1 μs) [1]. The magnitude of the electric field at the structure's wall is a key parameter determining when breakdown will occur. Thus, the relation between the power in a waveguide and the electric field at the wall was derived for different waveguide modes [1,143]. Therefore, it can be estimated that the power handling capacity at 10 GHz reaches 10 GW for TE_{11} and TM_{01} input modes while it reaches 46.7 GW for TE_{01} output mode. Practically, the serpentine mode converter operated at 400 MW at the UNM with no breakdown. The breakdown field is highly dependent on the pressure inside the guide. Of course, in a perfect vacuum there would be no breakdown at all, because there would be no gas to ionize.

CHAPTER 8. CONCLUSIONS AND FUTURE WORK

This dissertation comprised four main themes. An RBWO generating single band HPM, a dual-band RBWO, an RBWO with asymmetric mode generation and extraction, and microwave power combining.

1- We have demonstrated a simple, effective way to generate Gaussian-like radiation with linear polarization whose direction of polarization can be changed by rotating a combined Bragg reflector. Detailed investigations have been performed for single-spiral Bragg reflectors with left- and right-fold corrugations. A study of the dispersion characteristics of the Bragg reflector has helped us understand the SWS physics. The Bragg reflector structure is designed to be cutoff at 10 GHz for the TE_{11} mode. Thus, the converted forward TE_{11} mode from the backward TM_{01} mode cannot propagate through the Bragg reflector structure. Instead it reflects toward the output. The TE_{11} mode was primarily clean at the output frequency, even though a small amount of power of the backward TM_{01} mode reflected at the anode toward the output.

2- Using MAGIC PIC simulations, we have demonstrated operation of a dual-band RBWO consisting of two SWSs with sinusoidal corrugation, an axisymmetric SWS-1 at the output end and SWS-2 at the cathode end with combined left- and right-single-fold spiral corrugations. This BWO can generate a Gaussian microwave beam at X-band and C-band with 6% tuning in each frequency band by change the distance between the SWSs and the guide magnetic field near the RCA. X-band generation is realized when SWS-1 operates as a BWO with the operating TM_{01} mode and SWS-2 operates as a Bragg reflector, converting the

backward TM_{01} mode to a forward linearly polarized TE_{11} mode. C-band generation is realized when SWS-2 operates as a BWO. We also show that the generation of each frequency component takes place at different times within the microwave pulse.

3- A novel means of extracting a Gaussian radiation from the RBWO was introduced. An EBG medium, which belongs to a broad family of engineered materials called metamaterials, was used to radially couple the generated mode from the interaction region to a concentric waveguide. The novel EBG medium follows a slotted waveguide antenna concept where the slot array is cut at the SWS wall in order to perturb the surface currents of the operating wave. The first EBG medium design was based on a traveling wave slot antenna (uniform leaky wave antenna). About half of the input voltage pulse was measured at the output when the SWS and the collector are not connected. This led to the design of an EBG medium based on a periodic leaky wave antenna. Microwave power of about 100 MW was extracted with a Gaussian radiation pattern.

4- We have proposed a power combiner using a circular waveguide T-junction to combine the output of two RBWOs driven by the same pulsed power generator. This combiner not only combines the microwave power, but also outputs a Gaussian beam when a TM_{01} mode is used as the input mode. As in the serpentine mode converter case, the electric field vector at the input of the combiner must be in the plane of the waveguide bend for TE_{11} to TM_{11} combining and conversion. For both TE_{11} mode and TM_{01} mode input, the power transmission efficiency is 42% where 50% is the maximum efficiency for a two-channel power combiner

without losses. In addition, 2-, 4-, and *N*-Way power combiner structures were designed and characterized using HFSS. Their structures are overmoded waveguides in which input and output modes are different.

A brief list of recommendations for verifying and improving the results are given as a future work to be performed:

1- A mode purification experiment is important to study the output mode pattern of the single-band RBWO with Bragg reflector.
2- Experiments to verify single/dual band RBWO operation should be performed.
3- Experiments to study the *N*-way power combiner for short HPM pulses should also be performed.

APPENDIX

A: Current Monitors

Rogowski Coil:

Rogowski coils have been in use since 1912 [136]. Early applications of Rogowski coil technology were limited to measurement of magnetic fields due to the low signal output. The advancement of electronics has provided opportunities to use Rogowski coil technology in a wide range of applications. In particular, the low voltage output of Rogowski coils is compatible for use with microprocessor based systems. The advantages offered by Rogowski technology; accuracy, measurement range, bandwidth, unlimited short circuit current tolerance, and design flexibility are rapidly generating interest in a number of applications.

A Rogowski coil, also called an air-core coil, is a coil consisting of many windings lined up in a toroidal configuration encircling the current path [137]. It is a special type of mutual inductor that is often used to measure high AC and transient currents. Since the output signal of the Rogowaski coil is proportional to current flowing through it, it can be considered as a transformer [138]. Figure A.1 shows the basic configuration of the current sensor.

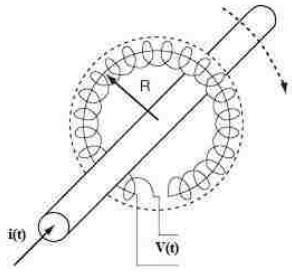

Figure A.1. Basic configuration of a Rogowski coil used to measure the beam current at the entrance of the SWS [138].

In many applications the use of traditional magnetic (iron) core transformers (CTs), solid or split, may be limited by both electrical characteristics and mechanical design. Magnetic CTs have typically been used in permanent applications, while magnetic core clamp-on CTs have long been the standard in portable test and measurement applications.

Rogowski coils are different from the conventional CTs in which the magnetic core of the CTs is replaced by air core. In fact, CTs provide a convenient means for measuring low currents or very brief, high amplitude currents, but are restricted by the Coulomb limit. Once this limit is exceeded, the CT output becomes nonlinear due to saturation of the magnetic core and the serious residual magnetism of the iron core at high currents, which can lead to excessive measurement errors.

When a Rogowski coil is placed around a current-carrying conductor, according to Ampere's law, the coil generates a voltage, *V(t)*, proportional to the coil's mutual inductance, *M*, and the time of change of current, *di(t)/dt*, and is given by

$$V(t) = M\ \frac{d\ i(t)}{dt}. \qquad (A-1)$$

The current is derived using the relations

$$i(t) = \frac{1}{M} \int V(t)dt, \qquad (A-2)$$

where the mutual inductance For toroidal coils is given by

$$M = \begin{cases} \frac{\mu_0}{2\pi}\ N\ W\ \ln(\frac{b}{a}); & \text{for a rectangular cross} - \text{section coil} \\ \frac{\mu_0}{2}\ N\left(a + b - 2\sqrt{ab}\right); & \text{for a circular cross} - \text{section coil} \end{cases},$$

here μ_0 is the permeability of air, *N* is the number of turns of the coils, *W* is the width (thickness in current direction) of the toroid, *b* is the outside radius, and *a* is the inside radius.

For non-self-integrating coils, the output of the coil is proportional to *di/dt*, rather than to the current itself. As a result, an integrator is needed to complete the current-measuring system. This can be done by one of two common means: (1) by use an electrical or electronic integrator, or (2) by using numerical integration in software after the coil output voltage is digitized. The electronic integrator maybe as simple as a passive RC circuit for moderating fast systems (1μs to 10 ms), or it may be a feedback amplifier based integrator (for long-pulses) [139].

For exceptionally fast systems, the L/R characteristics of the coil itself may be used to make a self-integrating Rogowski coil. The most severe limitation of the self-integrating coil is nonuniform excitation in the windings of the coil. If the risetime of the current pulse is shorter than the transit time in the sensor, the voltages induced in different locations along the torus reach the metering resistor with different delays, which can lead to strong oscillations, distorting the pulse shape. Although it is still possible to reproduce the risetime of a step pulse if the Rogowski coil is terminated with an impedance much higher than the Rogowski coil impedance $(L/C)^{1/2}$, it is no longer possible to measure current pulses with duration less than the wave transit time along the coil (the speed of light and length of coil's wire ratio). Therefore, it is not completely true that the signal response of a coil is independent of the current density distribution inside the torus [138].

To eliminate the portion of the signal created by a large flux penetrating the main opening of the torus, it is possible to compensate for this by feeding one end of the wire back through the winding at a mid-radius ($R_c = (a+b)/2$), as shown in Fig. A.2. Alternatively, the Rogowski coil can be built into a metallic housing, which short-circuits the main opening and reduces capacitive pickup.The housing must be slotted at the inner

side to allow the flux to penetrate. However, at the large electrical stresses associated with high-power fast rising pulses, flashover can occur at the shielding groove or along the surface of the sensor itself, resulting in false signals [138]. Also, two layers of winding, one of the opposite pitch to the other, is used to help cancel the effect of stray magnetic fields upon the coil [137, 139].

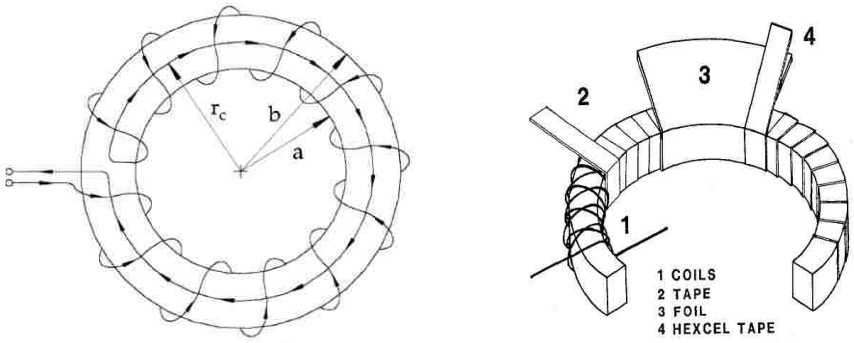

Figure A.2. Flux compensation methods [137,139].

Rogowski Coil Calibration:

After building the coil and the integrator, the reminding task is to calibrate the coil against a reference. This calibration step is necessary to account for errors due to the approximations used in calculations and tolerances in manufacturing. On way of calibration consists of measuring a current with both the Rogowski coil and a reference, such as a commercially available CT or a known current source.

In this work, a Rogowski coil was used at the cathode end to measure the total electron beam current. The coil has a L/R time of ~1 μs, allowing for effective self-integration of the current signal and easy output directly to a fast oscilloscope. The Rogowski was calibrated by previous students using a custom pulser that consists of a 50 Ω coaxial line that is charged and then switched into a 50 Ω load. Current dumped by the coaxial line into the load was then recorded using an oscilloscope. At the same time, the

Rogowski signal was recorded and calculated as V_{load}/2x50. Comparison between these two signals yielded the calibration constant of 20A/V. This calibration setup and procedure are similar to that described in [140] and shown in Fig A.3.

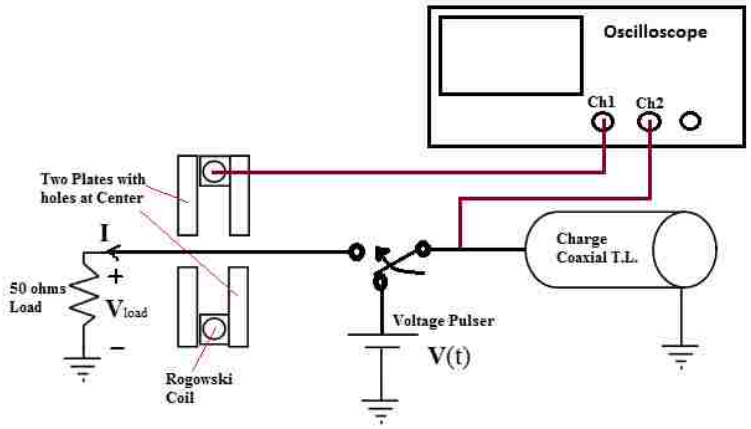

Figure A.3. Calibration setup for the Rogowski coil.

Current-Viewing Resistors (CVRs):

The problems associated with flux-coupled sensors when used with high-power fast-rising pulses can be avoided with CVRs, also called shunts [138]. For fast risetimes, high common-mode voltages, high current levels, the net result of these conditions is to discourage direct measurement of current via shunts or sampling resistors [139].

Generally, the shunts used are low inductance resistors that are empirically calibrated. Low inductance in the shunt is necessary to prevent $L(di/dt)$ voltages from corrupting measurements of current. Shunts require the use of voltage dividers on instrumentation to reduce common-mode voltage when those voltages are large. These dividers, in turn, reduce the signal-to-noise ratio in the current measurement.

In our experiment, a 5 mΩ shunt was used to measure the current passed through the solenoid coils. The current duration is in order of milliseconds. The shunt is terminated

by a 50 Ω scope channel after attenuating the signal and the measured current can be calculated as (V_{scope} * Attenuation/5 mΩ).

B: Voltage Monitor

Two common techniques are usually used for measurement of voltages. The first technique is the use of high-impedance voltage dividers with low-inductance resistors. These dividers reduce the signal-to noise ratio and are potentially difficult to compensate properly for frequency. This technique can be related to the shunts that discussed in the previous Section.

The second technique, which was used in this work, is the use of a capacitive voltage divider. A capacitive sensor built into a transmission line as a capacitive voltage divider is shown in Fig. B.1.

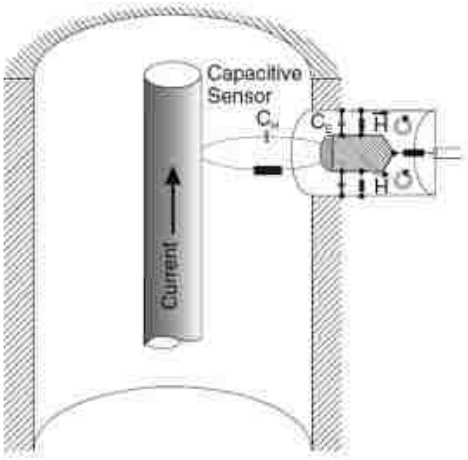

Figure B.1. Scheme of capacitive sensor integrated into a coaxial line [138].

High voltage dividers with predominantly capacitive coupling to the high-voltage electrode are frequently employed in liquid dielectric transmission lines. In Fig. B.1, capacitors C_H and C_E represent high voltage and low voltage arms, respectively. C_E is the

capacitance between the sensor and the ground and C_H is the capacitance between the active sensor area and the opposite (high-voltage) electrode. The capacitance normally is on the order of a few pF that draws very little current from the main circuit and the voltage measured by the probe V_{meas} can be expressed as

$$V_{meas}(t) = \frac{C_H}{C_H + C_E} V_{total}(t), \qquad (B-1)$$

where C_H is given by

$$C_H = \frac{\epsilon\epsilon_0 A}{a \ln(\frac{b}{a})}; \; C_H \ll C_E, \qquad (B-2)$$

here *a* and *b* are the inner and the outer radii of a coaxial cylindrical line for the case of a pure TEM wave propagating across area *A*.

The capacitive divider probe for voltage measurements on the SINUS-6 is located towards the end of the transmission line in oil right before transition to vacuum.

Capacitive Divider Probe Calibration:

The equivalent circuit of the calibration setup is shown in Fig. B.2. This diagnostic was calibrated by sending a 5 kV pulse back into the transmission line through the cathode connection. The transmission line was first charged through a 50 MΩ charging resistor and a variac-controlled 10 kV DC power supply. It was then discharged through a spark gap switch to a matched load, which in this case is a 100 Ω resistor. The charge voltage on the line was measured using a x1000 high voltage probe connected to a multimeter. To provide the high voltage probe with the required 1 MΩ input impedance, a 1.1 MΩ resistor was placed parallel with the 12 MΩ impedance of the multimeter. The

response of the capacitive divider probe was recorded on a digital oscilloscope. The calibration constant was calculated by taking the ratio of the charging voltage and the voltage on the oscilloscope. This experiment was repeated for several different charging voltages in order to confirm the consistency of the calibration procedure. The calibration constant was measured to be 2.45 kV/V.

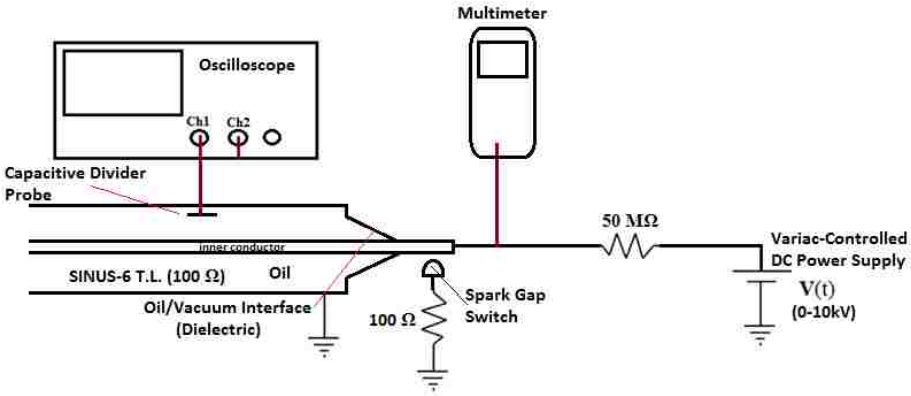

Figure B.2. Calibration setup for the capacitive voltage divider probe.

C: Power Measurements

In previous experiments at UNM, the pickup signal from a rectangular waveguide antenna was sent through a crystal detector for power measurement. The open rectangular waveguide and crystal detector method is sensitive to mode and polarization. If more than one mode exists, the measurements are not accurate. Unfortunately, the RBWO with Bragg reflector experiment simultaneously outputs the TE_{11} and TM_{11} modes. This is what forced the need for a mode-flexible microwave power diagnostic. The microwave calorimeter, which was constructed at UNM [141], was used because of its ability to measure energy from any radiated mode without complication. The UNM calorimeter is similar to that which was built in Tomsk, Russia [142]. Its structure consists of two round sections of clear acrylic (polystyrene) glass of 45 cm diameter and thickness 0.9525 cm

(3/8 inch), which sandwich a 40 cm diameter, 0.9525 cm thick layer of pure ethanol and several rigidity struts, as shown in Fig. C.1.

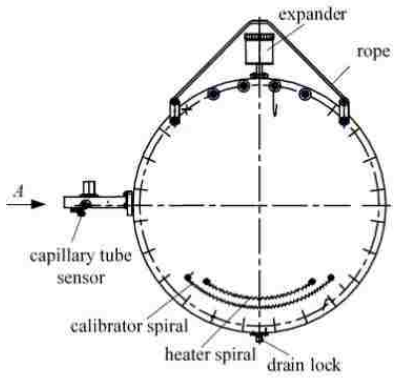

Figure C.1. UNM's calorimeter construction is similar to that used in Tomsk, Russia [142].

Once microwave energy is absorbed, it causes expansion of the alcohol volume into a glass capillary tube of inner diameter 1 mm. Measurement of the expansion of this volume was accomplished with a resistive bridge. The moving column of ethanol between the two parallel filaments provides a changing voltage. The signal was buffered, filtered, and then sent to a PC's USB COM-port, where it is displayed in an Arduino software scrolling data screen.

Calorimeter Calibration:

Calibration of the calorimeter for both the energy and frequency response was performed. For energy calibration, it was straightforward: a well regulated 20 V DC power supply switched into the 6 Ω nichrome wire calibration coil that is immersed into the body of alcohol. Measurement of the voltage across the calibration wire and integrating the square pulse over time yielded the Ohmic-heating energy deposition. A

calibration curve yielded after averaging several measured shots at a series of energies is in Fig. C.2.

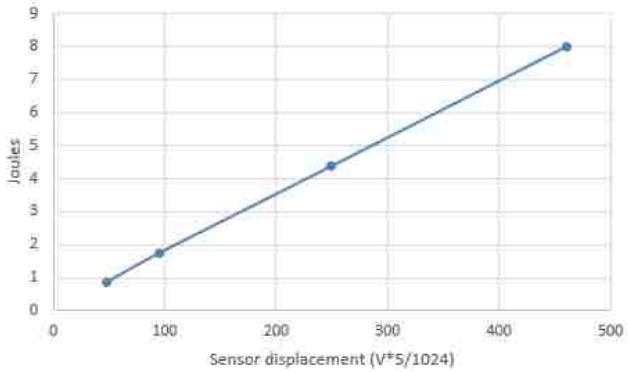

Figure C.2. Calorimeter calibration curve [141].

HPM impinging on the surface of the calorimeter are reflected, absorbed, and transmitted to varying degree depending on frequency, as measured by two horn antennas and a network analyzer, Fig. C.3. A typical power absorption coefficient for the RBWO experiments producing 10 GHz was about 85%, as shown in Fig. C.4.

Figure C.3. Frequency calibration setup for the microwave calorimeter.

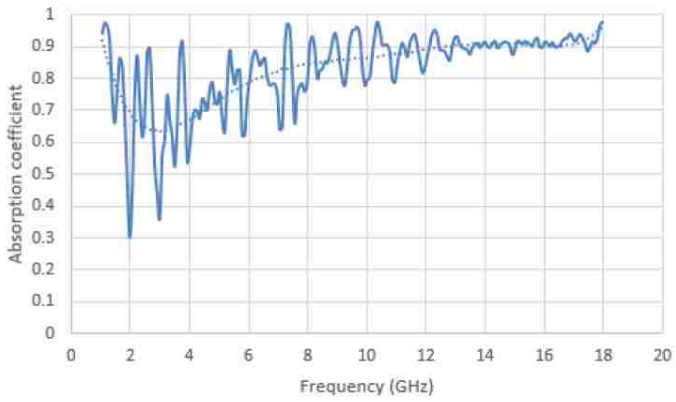

Figure C.4. Absorption coefficient for the UNM calorimeter [141].

REFERENCES

[1] J. Benford, J. A. Swegle, E. Schamiloglu, *High Power Microwaves, 3rd Ed.* (CRC Press, Boca Raton, FL, 2016).

[2] A.S. Gilmour, *Microwave Tubes* (Artech House, Norwood, MA, 1986).

[3] R.J. Barker and E. Schamiloglu, Eds., *High-Power Microwave Sources and Technologies* (IEEE Press/John Wiley and Sons, New York, NY, 2001).

[4] A.S. Gilmour, *Principles of Traveling Wave Tubes* (Artech House Print on Demand, Norwood, MA, 1994).

[5] A. Blyakhman, D. Clunie, R. Harris, G. Mesyats, M. Petelin, G. Postoenko, and B. Wardrop, "Nanosecond Gigawatt Radar: Indication of Small Targets Moving Among Heavy Clutters," in *Proc. 2007 IEEE Radar Conf.* (Boston, MA, 2007), pp. 61-64.

[6] A.D. Oliver, P.J.B. Clarricoats, L. Shafai, and A.A. Kishk, *Microwave Horns and Feeds* (IET, London, UK, 1994).

[7] V.D. Vinogradov and G.G. Denisov, "The Conversion in a Bent Waveguide with a Variable Curvature," *Radiophys. Quantum Electron.*, vol. 33, p. 540-545, 1990.

[8] B.Z. Katsenelenbaum, L. Mercader del Rio, M. Pereyaslavetz, M. Sorolla Ayza, and M. Thumm, *Theory of Nonuniform Waveguides* (IET, London, UK, 1998).

[9] V.I. Belousov, E.V. Koposova, I.M. Orlova, N.Y. Peskov, and M.I. Petelin, "Auxilliary Elements of High-Power Quasioptical Waveguide Ducts," *Gyrotrons: Collected Papers*, V.A. Flyagin, Ed. (Institute of Applied Physics, Russian Academy of Sciences, Nizhny Novgorod, Russia, 1989), pp. 155-160.

[10] N.F. Kovalev, N.G. Kolganov, A.V. Palitsin, and M.I. Fuks, "Relativistic BWO with Cyclotron Selection of an Asymmetric Wave," in *Strong Microwave in Plasmas* (Institute of Applied Physics, Russian Academy of Sciences, Nizhny Novgorod, Russia, 2000), pp. 845-850.

[11] N.F. Kovalev, A.V. Palitsin, and M.I. Fuks, "Cyclotron Suppression of Generation in a Relativistic BWO of Cerenkov Type," *Radiophys. Quantum Electron.*, vol. 49, pp. 93-107, 2006.

[12] E.B. Abubakirov, M.I. Fuks, N.G. Kolganov, N.F. Kovalev, A.V. Palitsin, and A.B. Volkov, "Reduction of Focusing Magnetic Field in Relativistic Cerenkov Oscillators," in *Strong Microwaves in Plasmas* (Institute of Applied Physics, Russian Academy of Sciences, Nizhny Novgorod, Russia, 1996), pp. 810-828.

[13] M. Fuks, E. Schamiloglu, N. Kovalev, and A. Palitsin, "Self-Consistent Theory of Cyclotron Phenomena in Relativistic BWOs," in *Proc. SPIE – Intense Microwave Pulse VIII* (Orlando, FL, 2001), pp. 146-156.

[14] E.B. Abubakirov, J.P. Brasile, A.N. Denisenko, M.I. Fuks, N.F. Kovalev, A.V. Saveljev, M. Simon, E.I. Soluyanov and V.V. Yastrebov, "Oversized Relativistic BWO with Selective Bragg Mode Converter," *Digest of Technical Papers of the*

International Workshop on HPM Generation and Pulse Shortening (Edinburgh, UK, 1997), pp. 179-183.

[15] E.B. Abubakirov, A.N. Denisenko, M.I. Fuks, E.A. Kopelovich, N.F. Kovalev, A.V. Saveljev, E.I. Soluyanov and V.V. Yastrebov, "Relativistic Backward Wave Oscillator using a Selective Mode Converter," *Tech. Phys.*, vol. 44, pp. 1356-1359, 1999.

[16] R. Kompfner, "The Invention of Traveling Wave Tube," *IEEE Trans. Electron Dev.*, vol. ED-23, p. 730, 1976.

[17] J.A. Nation, "On the Coupling of a High-Current Relativistic Electron Beam to a Slow Wave Structure," *Appl. Phys. Lett.*, vol. 17, p. 491, 1970.

[18] Y. Carmel, J. Ivers, R.E. Kribel, and J. Nation, "Intense Coherent Cerenkov Radiation due to the Interaction of a Relativistic Electron Beam with a Slow-Wave Structure," *Phys. Rev. Lett.*, vol. 33, pp. 1278-1282, 1974.

[19] N.F. Kovalev, M.I. Petelin, M.D. Raizer, A.V. Smorgonskii, and L.E. Tsopp, "Generation of Powerful Electromagnetic Radiation Pulses by a Beam of Relativistic Electrons," *Sov. Tech. Phys. Lett.*, vol. 18, pp. 232-235, 1973.

[20] L.S. Bogdankevich, M.V. Kuzelev, and A.A. Rukhadze, "Plasma Microwave Electronics," *Sov. Phys. Usp.*, vol. 24, pp. 1-16, 1981.

[21] N.F. Kovalev, V.I. Petruhina, and A.V. Smorgonsky, "Ultra-Relativistic Carcinotron," Radiotechnique and Electronics, vol. 20, pp. 1547-1550, 1975.

[22] N.F. Kovalev and V.I. Petruhina, "Ultra-Relativistic Carcinotron with a Jump in Beam-RF Coupling," *Electr. Techn. SVCH*, vol. 7, pp. 101-105, 1977.

[23] N.M. Bykov, V.P. Gubanov, A.V. Gunin, S.D. Korovin, G.A. Mesyats, S.D. Polevin, A.M. Roitman, V.V. Rostov, A.V. Smorgonsky, and A.F. Yakushev, "Relativistic Periodic-Pulse Microwave Oscillators," in *Relativistic High-Frequency Electronics* (Institute of Applied Physics, USSR Academy of Science, Gorky, USSR, 1988), pp. 101-125.

[24] S.D. Korovin, S.D. Polevin, A.M. Roitman, and V.V. Rostov, "Relativistic Backward Tube with Variable Phase Velocity," *Sov. Tech. Lett.*, vol. 18, pp. 265-269, 1992.

[25] N.F. Kovalev, N.G. Kolganov, A.V. Palitsin, and M.I. Fuks, "Relativistic BWO with Cyclotron Selection of an Asymmetric wave," in *Strong Microwave in Plasmas* (Institute of Applied Physics, Russian Academy of Sciences, Nizhny Novgorod, Russia, 2000), pp. 845-850.

[26] E.B. Abubakirov, N.F. Kovalev, and M.I. Fuks, "High-Selectivity Resonator for Powerful Microwave Sources," in *Proc. 11th Int. Conf. on High-Power Particle Beams* (Institute of Plasma Physics, Prague, Czech Republic, 1996), Vol. 1, pp. 410-413.

[27] V.L. Bratman, G.G. Denisov, N.S. Ginzburg, and M.I. Petelin, "FELs with Bragg Reflection Resonators: Cyclotron Autoresonance Masers Versus Ubitrons," *IEEE J. Quantum Electron.*, vol. 19, pp. 282-296, 1983.

[28] High Frequency Structure Simulator (HFSS 13.0.2), Version 13, Ansoft Corporation, Pittsburgh, PA, 2011. http://www.ansys.com/

[29] http://www.cst.com/

[30] B. Goplen, L. Ludeking, D. Smithe, and G. Warren, "User-Configurable MAGIC for Electromagnetic PIC Simulations," *Comput. Phys. Commun.*, vol. 87, pp. 54-87, 1995.

[31] J.R. Pierce, "Theory of the Beam-Type Traveling-Wave Tube," *Proc. IRE*, vol. 35, pp. 111-123, 1947.

[32] J.R. Pierce, *Traveling Wave Tubes* (Van Nostrand, New York, NY, 1950).

[33] H.R. Johnson, "Backward-Wave Oscillators," *Proc. of the IRE*, vol. 43, pp. 684-697, 1955.

[34] G.N. Rapoport, "Non-linear Theory of the "O"-Type BWO with Periodic Slow-Wave Structure," *Radiotekhnika i elektronika*, vol. 9, pp. 483-504, 1964.

[35] S.E. Tsimring, *Electron Beams and Microwave Vacuum Electronics* (John Wiley and Sons, New York, NY, 2007).

[36] N.F. Kovalev and A.V. Smorgonsky, "The Theory of an Ultrarelativistic TWT," *Radio Eng. Electron. Phys.*, vol. 20, pp. 133-136, 1975.

[37] C.A. Balanis, *Advanced Engineering Electromagnetics, 2nd Ed.* (John Wiley and Sons, New York, NY, 2012).

[38] D.G. Swanson, *Plasma Waves, 2nd Ed.* (Taylor & Francis, Boca Raton, FL, 2003).

[39] F.F. Chen, *Introduction to Plasma Physics and Controlled Fusion, Vol. 1, Plasma Physics, 2nd Ed.* (Springer, New York, NY, 2006).

[40] K. Minami, M. Saito, Y. Choyal, K.P. Maheshwari, and V.L. Granatstein, "Linear Dispersion Relation of Backward-Wave Oscillators With Finite-Strength Axial Magnetic Field," *IEEE Trans. Plasma Sci.*, vol. 30, pp. 1134-1146, 2002.

[41] J.A. Swegle, J.W. Poukey, and G.T. Leifeste, "Backward Wave Oscillators with Rippled Wall Resonators: Analytic Theory and Numerical Simulation," *Phys. Fluids*, vol. 28, pp. 2882-2894, 1985.

[42] C.S. Lui and V.K. Tripathi, *Interaction of Electromagnetic Waves with Electron Beams and Plasmas* (World Scientific, River Edge, NJ, 1994).

[43] I.P. Trifonov and N.I. Karbushev, "Excitation by a Relativistic Electron Beam of a Backward Wave in a Smooth Waveguide Containing a Dielectric Rod" *Sov. Phys. Tech. Phys.*, vol. 283, pp. 263-266, 1983.

[44] A.F. A1exandrov, S.Yu. Galuzo, V.I. Kanavets, and V.A. Pletyushkin, "Excitation of Surface Waves by a Relativistic Electron Beam in a Corrugated Waveguide," *ZhTF*, vol. 51, pp. 1727-1730, 1981.

[45] B.N. Brejzman and D.D. Ryutov, "Powerful Relativistic Electron Beams in a Plasma and in a Vacuum (Theory)" *Nucl. Fusion*, vol. 14, pp. 873-907, 1974.

[46] H.S. Uhm and J.Y. Choe, "Properties of the Electromagnetic Wave Propagation in a Helix-Loaded Waveguide," *J. Appl. Phys.*, vol. 53, pp. 8483-8488, 1982.

[47] B.T. Henoch, *Investigations of the Disk-Loaded and Helical Waveguide* (KTH, Stockholm, Sweden, 1958).

[48] K.W.H. Foulds, and J.R. Mansell, "Propagation of an Electromagnetic Wave through a Helical Waveguide," *Proc. IEE*, vol. 111, pp. 1789-1798, 1964.

[49] Y. Wei, W. Wang, J. Sun, B. Jia, A.K. Sinha, S. Liu, and G. Park, "Experimental Demonstration of the Effect of Groove Shape on the Wave Properties of the Helical Groove Waveguide," *IEEE Microw. Compon. lett.*, vol. 13, pp. 484-486, 2003.

[50] Y. Wei, W. Wang, and J. Sun, "An Approach to the Analysis of Arbitrarily Shaped Helical Groove Waveguides," *IEEE Microw. Guided Wave lett.*, vol. 10, 2000.

[51] G. Saxon, T.R. Jarvis, and I. White, "Angular-Dependent Modes in Circular Corrugated Waveguide," *Proc. IEE.*, vol. 110, pp. 1365-1373, 1963.

[52] W. Walkinshaw, "Theoretical Design of Linear Accelerators for Electrons," *Proc. Phys. Soc.*, vol. 61, pp. 246-254, 1948.

[53] C.C. Tang, "On the Wave Propagation and Mode Conversion in a Helically Corrugated Multimode Circular Waveguide," *IEEE Trans. Microw. Theory Techn.*, vol. MTT-14, pp. 275-284, 1966.

[54] L. Young, Ed., *Advances in Microwaves, Vol. 4* (Academic Press, New York, NY, 1969).

[55] L. Moreland, "Effects of Varying Coupling Impedance, Finite Length, and Asynchronous Harmonics on High Power BWO Performance," Dissertation, Dept. of Elec. and Comp. Eng., University of New Mexico, New Mexico, 1995.

[56] G.W. Buckley and J. Gunson, "Theory and Behavior of Helix Structures for a High-Power Pulsed Traveling-Wave Tube", *Proc. IEE.*, vol. 106, pp. 478-486, 1959.

[57] H.P. Freund, M.A. Kodis, and N.R. Vanderplaats, "Self-Consistent Field Theory of a Helix Traveling Wave Tube Amplifier," *IEEE Trans. Plasma Sci.*, vol. 20, no. 5, pp. 543-553, 1992. Also, R.G. Hutter, *Beam and Wave Electronic in Microwave Tubes, 1st Ed.* (Van Nostrand, New York, NY, 1960).

[58] C. Chen, "Pierce-Type Dispersion Relation for an Intense Relativistic Electron Beam Interacting with a Slow-Wave Structure," *Phys. Plasmas*, vol. 1, pp. 167-170, 1994.

[59] J. Swegle, "Approximate Treatment near Resonance of Backward and Traveling Wave Tubes in the Compton Regime," *Phys. Fluides*, vol. 28, pp. 3696-3702, 1985.

[60] M.I. Petelin, "The Similarity Principle for High-Frequency Devices Having Ultrarelativistic Electron Beams," *Radiophys. Quantum Electron.*, vol. 13, pp. 1229-1231, 1970.

[61] K. Minami, K. Ogura, Y. Aiba, M.R. Amin, X.D. Zheng, T. Watanabe, Y. Cannel, W.W. Destler, and V.L. Granatstein, "Starting Energy and Current for a Large Diameter Finite Length Backward Wave Oscillator Operated at the Fundamental Mode," *IEEE Trans. Plasma Sci.*, vol. 23, pp. 124-132, 1995.

[62] V.S. Ivaov, N.F. Kovalev, S.I. Krementsov, and M.D. Raizer, "Relativistic Millimeter Carcinotron," *Sov. Tech. Phys. Lett.*, vol. 4, pp. 329-330, 1978.

[63] N.S. Ginzburg, S.P. Kuznetsov, T.N. Fedoseeva, "Theory of Transients in Relativistic Backward-Wave Tubes," *Radiophys. Quantum Electron.*, vol. 21, pp 728-739, 1978.

[64] N.I. Zaitsev, N.F. Kovalev, B.D. Kol'chungin, and M.I. Fuks, "Experimental Investigation of a Relativistic Carcinotron," *Sov. Phys. Tech. Phys.*, vol. 52, pp. 986-989, 1982.

[65] B. Levush, T.M. Antonsen, A. Bromborsky, W. Lou, and Y. Carmel, "Theory of Relativistic Backward-Wave Oscillators with End Reflections," *IEEE Trans. Plasma Sci.*, vol. 20, pp. 263-280, 1992.

[66] N.F. Kovalev, I.M. Orlova, and M.I. Petelin, "Wave Transformation in a Multimode Waveguide with Corrugated Walls," *Radiophys. Quantum Electron.*, vol. 11, pp 449-450, 1968.

[67] N.S. Ginzburg, N.Y. Peskov, R.M. Rozental, and A.S. Sergeev, "Using Two-Dimensional Bragg Structures for the Synchronization of Radiation in Planar Backward Wave Oscillators," *Tech. Phys. Lett.*, vol. 35, pp. 190–192, 2009.

[68] I.V. Konoplev, P. McGrane, A.W. Cross, K. Ronald and A.D.R. Phelps, "Wave Interference and Band Gap Control in Multiconductor One-Dimensional Bragg Structures," *J. Appl. Phys.*, vol. 97, pp. 073101-7, 2005.

[69] A. Shaw, B. Roycroft, J. Hegarty, D. Labilloy, H. Benisty, C. Weisbuch, T.F. Krauss, C.J.M. Smith, R. Stanley, R. Houdré and U. Oesterle, "Lasing Properties of Disk Microcavity Based on a Circular Bragg Reflector," *Appl. Phys. Lett.*, vol. 75, pp. 3051-3053, 1999.

[70] G.G. Denisov, V.L. Bratman, A.D.R. Phelps, and S.V. Samsonov, "Gyro-TWT with a Helical Operating Waveguide: New Possibilities to Enhance Efficiency and Frequency Bandwidth," *IEEE Trans. Plasma Sci.*, vol. 26, pp. 508-518, 1998.

[71] Y. Lai, S. Zhang, X. Wei, S. Wang, C. Yu, and L. Yang, "Multiwave Interaction Analysis of a Coaxial Bragg Structure with a Localized Defect Introduced in Sinusoidal Corrugations," in *Proc. Asia Pacif. Microw.* (Singapore, 2009), pp. 457-460.

[72] H. Kogelnik and C.V. Shank, "Coupled-Wave Theory of Distributed Feedback Lasers," *J. Appl. Phys.*, vol. 43, pp. 2327-2335, 1972.

[73] G.G. Denisov and M.G. Reznikov, "Corrugated Cylindrical Resonators for Short-Wavelength Relativistic Microwave Oscillators," *Radiophys. Quantum Electron.*, vol. 25, pp 407-413, 1982.

[74] M.I. Petelin, "Mode Selection in High Power Microwave Sources," *IEEE Trans. Electron Dev.*, vol. ED-48, pp. 129-133, 2001.

[75] L. Brillouin, *Wave Propagation in Periodic Structures* (McGraw-Hill, New York, NY, 1946).

[76] S.D. Korovin and V.V. Rostov, "High-Current Nanosecond Pulse-Periodic Electron Accelerators Utilizing a Tesla Transformer," *Russ. Phys. J.*, vol. 39, pp. 1177-1286, 1986.

[77] A. Elfrgani, M. Fuks, S. Prasad, and E. Schamiloglu, "X-Band Tunable Relativistic BWO with Linearly Polarized Gaussian Radiation," in *Proc. 16th Int. Symp. Electromagn. Launch Technol.* (China, 2012), pp. 1-5.

[78] A A. Elfrgani, M. Fuks, S. Prasad, and E. Schamiloglu, "X-Band Relativistic Backward Wave Oscillator with Two-Spiral Corrugated Bragg Reflector," in *Proc. IEEE Int. Power Modulator Conf. High Voltage Workshop* (San Diego, CA, 2012), pp. 756–759.

[79] A. Elfrgani, S. Prasad, M. Fuks, and E. Schamiloglu, "Relativistic BWO with Linear Polarized Gaussian Radiation Pattern," *IEEE Trans. Plasma Sci.,* vol. 42, pp. 2135-2140, 2014.

[80] S. Prasad, C.J. Buchenauer, M. Fuks, C. Leach, M. Roybal, E. Schamiloglu, and W. White, "X-Band Relativistic BWO with Frequency Tuning," in *Proc. IEEE Int. Conf. Plasma Sci.* (San Diego, CA, 2009), p. 1.

[81] I.K. Kurkan, V.V. Rostov, and E.M. Totmeninov "A Possible Method of Reducing the Magnetic Field in a Relativistic Backward-Wave Tube," *Tech. Phys.,* vol. 24, pp. 388-389, 1998.

[82] S.D. Korovin, S.D. Polevin, A.M. Roitman, and V.V. Rostov, "Influence of the Traveling Wave on Efficiency of the Relativistic BWO," *Sov. Tech. Phys. Lett.,* vol. 20, pp. 12-16, 1994.

[83] S.A. Kitsanov, A.I. Klimov, S.D. Korovin, I.K. Kurkan, I.V. Pegel, and S.D. Polevin, "Pulsed 5-GW Resonance Relativistic BWT for a Decimeter Wavelength Range," *Tech. Phys. Lett.,* vol. 29, pp. 259–261, 2003.

[84] S.D. Korovin, I.K. Kurkan, V.V. Rostov, and E.M. Totmeninov "Relativistic Backward-Wave Oscillator with a Discrete Resonance Reflector," *Radiophys. Quantum Electron.,* vol. 42, pp. 1047-1054, 1999.

[85] E.M. Totmeninov, A.I. Klimov, I.K. Kurkan, S.D. Polevin, and V.V. Rostov, "Repetitively Pulsed Relativistic BWO with Enhanced Mechanical Frequency Tunability," *IEEE Trans. Plasmas Sci.,* vol. 36, pp. 2609-2612, 2008.

[86] L.D. Landau and E.M. Lifshitz, *Electrodynamics of Continuous Media, Vol. 8, 1st Ed.* (Pergamon Press, London, UK, 1960).

[87] C.C. Johnson, *Field and Wave Electrodynamics* (McGraw-Hill, New York, NY, 1965).

[88] H. Guo, Y. Cannel, W.R. Lou, L. Chen, J. Rodgers, D.K. Abe, A. Bromborsky, W. Destler, and V.L. Granatstein, "A Novel Highly Accurate Synthetic Technique for Determination of the Dispersive Characteristics in Periodic Slow Wave Circuits," *IEEE Trans. Microw. Theory Techn.,* vol. MTT-40, pp. 2086-2094, 1992.

[89] G. Xi, Y. Zi-Qiang, C. Wei-Ping, and J. Yan-Nan, "Dispersion Characteristics of a Slow Wave Structure with a Modified Photonic Band Gap," *Chin. Phys. B,* vol. 20, pp. 30703-6, 2011.

[90] Y. Cannel, H. Guo, W.R. Lou, D. Abe, V.L. Granatstein, and W.W. Destler, "Novel Method for Determining the Electromagnetic Dispersion Relation of Periodic Slow Wave Structures," *Appl. Phys. Lett.*, vol. 57, pp. 1304-1306, 1990.

[91] C.A. Balanis, *Antenna Theory: Analysis and Design 3rd Ed.* (John Wiley & Sons., New York, NY, 2005).

[92] S.B. De Assis Fonseca and A.J. Giarola, "Microstrip Disk Antennas, Part I: Efficiency of Space Wave Launching," *IEEE Trans. Antennas Propag.,* vol. AP-32, pp. 561–567, 1984.

[93] S.B. De Assis Fonseca and A. J. Giarola, "Microstrip Disk Antennas, Part II: the Problem of Surface Wave Radiation by Dielectric Truncation," *IEEE Trans. Antennas Propag.,* vol. AP-32, pp. 568–573, 1984.

[94] A. Elboushi and A. Sebak, "High Gain Microstrip Fed Slot Coupled Hybrid Antenna for MMW Applications," in *Proc. Radio Wireless Symp.* (Santa Clara, CA, 2012), pp. 303-306.

[95] J.T. Aberle and F. Zarosh, "Analysis of Probe-Fed Circular Microstrip Pateches by Circular Cavities," *Electromagnetics,* vol. 14, pp. 239-258, 1994.

[96] W. Main, Y. Cannel, K. Ogura, J. Weaver, G. Nusinovich, S. Kobayashi, J.P. Tate, J. Rodgers, A. Bromborsky, S. Watanabe, M.R. Amin, K. Minami, W.W. Destler, and V.L. Granatstein, "Electromagnetic Properties of Open and Closed Overmoded Slow-Wave Resonators for Interaction with Relativistic Electron Beams," *IEEE Trans. Plasmas Sci.,* vol. 22, pp. 566-577, 1994.

[97] C.K. Chong, D.B. McDermott, M.M. Razeghi, N.C. Luhmann, Jr., J. Pretterebner, D. Wagner, M. Thumm, M. Caplan, and B. Kulke, "Bragg reflectors," *IEEE Trans. Plasma Sci.,* vol. 20, pp. 393-402, 1992.

[98] "SINUS-6 Repetitively-Pulsed Electron Beam Accelerator & High Power Microwave Source: Operation & Maintenance Manual," High Current Electronics Institute-Tomsk-Russia, Version 1, pp. 1-41, 1992.

[99] D. Meeker, "Finite Element Method Magnetics," http://www.femm.info/wiki/HomePage, 2008.

[100] S.A. Shunailov, A.G. Reutova, V.G. Shpak, M.I. Yalandin, and G.A. Mesyats, "Injection Criteria and Energy Characteristics of Runaway Electron Beam Accelerated with a Nonuniform Field in Atmospheric Gap," *J. Korean Phys. Soc.,* vol. 59, pp. 3517-3521, 2011.

[101] A.V. Gaponov-Grekhov and V.L. Granatstein, *Applications of High-Power Microwaves* (Artech House, Norwood, MA, 1994).

[102] C.P. Zhu, R. Feng, and Y.Y. Zhao, "Sonochemical Effect of a Bifrequency Irradiation," *Chin. Sci. Bull.* vol. 45, pp. 142-145, 2000.

[103] O. Dumbrajs, "Multifrequency Gyrotron for Plasma Heating and Diagnostics," *Int. J. Infrared Milli.,* vol. 18, pp 2111-2115, 1999.

[104] Z. Yang, Z. Liang, B. Zhang, J. Li, W. Ma, S. Hu, and S. Liu, "A Cerenkov Oscillator Operating at Two Different Wave Bands," *Int. J. Infrared Milli.,* vol. 20, pp 83-92, 1999.

[105] N.S. Ginzburg, R.M. Rozental, and A.S. Sergeev, "Dual Band Operation of the Relativistic BWO," in *Proc. 4th IEEE Int. Conf. Vac. Electron.* (Seoul, Korea, 2003), pp. 181–182.

[106] Y. Tang, L. Meng, H. Li, L. Zheng, Y. Yin, and B. Wang, "A Dual-Frequency Coaxial Relativistic Backward-Wave Oscillator with a Modulating Resonant Reflector," *Phys. Scripta,* vol. 85, pp. 05581-7, 2012.

[107] D.I. Trubetskov and M.I. Rabinovich, *Oscillations and Waves: In Linear and Nonlinear Systems* (Kluwer Academic Publishers, Dordrecht, Netherlands, 1989).

[108] A. Elfrgani, S. Prasad, M. Fuks, and E. Schamiloglu "Single/Dual Band Relativistic BWO using Electron Beam Magnetic Field Decompression," in *Proc. IEEE Int. Conf. Pulsed Power Plasma Sci.* (San Francisco, CA, 2013), p. 1.

[109] A. Elfrgani, S. Prasad, M. Fuks, and E. Schamiloglu, "Dual-Band Operation of Relativistic BWO with Linearly Polarized Gaussian Output," *IEEE Trans. Plasma Sci.,* vol. 42, pp. 2141-2145, 2014.

[110] K.J. Button, Ed., *Infrared and Millimeter Waves, Vol. 13* (Academic Press, Waltham, MA, 1986).

[111] M. Friedman and M. Ury, "Production and Focusing of a High Power Relativistic Annular Electron Beam," *Rev. Sci. Instrum.,* vol. 41, pp. 1334-1335, 1970.

[112] L.O. Goldstone and A.A. Olinert, "Leaky-Wave Antennas I: Rectangular Waveguides," *IRE Trans. Antennas Propag.,* vol. 7, pp. 307-319, 1959.

[113] L.O. Goldstone and A.A. Olinert, "Leaky-Wave Antennas II: Circular Waveguides," *IRE Trans. Antennas Propag.,* vol. 9, pp. 280-290, 1961.

[114] D. Shiffler, J. Luginsland, D.M. French, and J. Watrous, "A Cerenkov-like Maser Based on a Metamaterial Structure," *IEEE Trans. Plasma Sci.,* vol. 38, pp. 1462-1465, 2010.

[115] J. Hummelt, S. Lewis, M. Shapiro, and R.J. Temkin, "Design of a Metamaterial Based Backward-Wave Oscillator," *IEEE Trans. Plasma Sci.,* vol. 42, pp. 930-936, 2014.

[116] M.I. Fuks (Private communication).

[117] N. Marcuvitz, *Microwave Handbook, MIT Radiation Lab Vol. 10* (McGraw-Hill, New York, NY, 1951).

[118] J.S. Ajioka, "Slot Antenna in Circular Waveguide," U.S. Patent 4825219, 1989.

[119] A.A. El'chaninov, A.I. Klimov, O.B. Koval'chuk, G.A. Mesyats, I.V.Pegel, I.V. Romanchenko, V.V. Rostov, K.A. Sharypov, and M.I. Yalandin, "Coherent Summation of Power of Nanosecond Relativistic Microwave Oscillators," *Tech. Phys.,* vol. 56, pp. 121-126, 2011.

[120] V.V. Rostov, A.A. El'chaninov, I.V. Romanchenko, and M.I. Yalandin, "A Coherent Two-Channel Source of Cerenkov Superradiance Pulses," *Appl. Phys. Lett.,* vol. 100, pp. 224102-1-4, 2012.

[121] M.I. Yalandin, S.A. Shunailov, M.R. Ul'maskulov, K.A. Sharypov, V.G. Shpak, V.V. Rostov, I.V. Romanchenko, A.A. El'chaninov, and A.I. Klimov, "Synphase Operation of Nanosecond Relativistic 37-GHz Backward-Wave Oscillators without Electrodynamic Coupling," *Tech. Phys.,* vol. 38, pp. 917-920, 2012.

[122] W. Bostick, E. Everhart, and M. Labitt, "Parallel Operation of Magnetrons," Research Lab. Electron., MIT, Cambridge, MA, Tech. Rep. 14, 1946.

[123] G. Li, T. Shu, J. Zhang, J. Yang, and C. Yuan, "Generation of Gigawatt Level Beat Waves," *Appl. Phys. Lett.,* vol. 96, pp. 234102-1, 2010.

[124] G. Li, T. Shu, C. W. Yuan, J. Zhu,J. Liu, B. Wang, and J. Zhang, "Simultaneous Operation of X band Gigawatt Level High Power Microwaves," *Laser Part. Beams,* vol. 28, pp. 35-44, 2010.

[125] Q. Zhang, C. Yuan, and L. Liu, "T-junction Waveguide-Based Combining High Power Microwave Beams," *Phys. Plasmas,* vol. 18, pp. 83110-4, 2011.

[126] L.B. Mullett, "Improvements in Microwave Circuits" British Patent 667 290, 1952.

[127] B.E. Kingdom, "A Circular Waveguide Magic-Tee and its Application to High-Power Microwave Transmission," *J. British Inst. Radio Eng*., vol. 13, pp. 275-287, 1953.

[128] G. Li, T. Shu, C. Yuan, J. Zhang, Z. Jin, and J. Yang, "Combining Microwave Beams with High Peak Power and Long Pulse Duration," *Phys. Plasmas,* vol. 17, pp. 033301-5, 2010.

[129] G. Li, T. Shu, C. Yuan, J. Zhang, J. Yang, Z. Jin, Y. Yin, D. Wu, J. Zhu, H. Ren, and J. Yang, "Coupling Output of Multichannel High Power Microwaves," *Phys. Plasmas,* vol. 17, pp. 123110-5, 2010.

[130] D.V. Vinogradov and G.G. Denisov, "Waveguide Mode Converter" USSR Patent 1566424, 1988.

[131] H. Li and M. Thumm, "Mode Conversion Due to Curvature in Corrugated Waveguides," *Int. J. Electron.,* vol. 71, pp. 333-347, 1991.

[132] S.P. Morgan, "Theory of Curved Circular Waveguide Containing an Inhomogeneous Dielectric," *Bell Syst. Tech. J.,* vol. 36, 1209-1251, 1957.

[133] E.J. Wilkinson, "An N-Way Hybrid Power Divider," *IRE Trans. Microw. Theory Techn.,* vol. 8, pp.116-118, 1960.

[134] K.J. Russell, "Microwave Power Combining Techniques," *IEEE Trans. Microw. Theory Techn.,* vol. MTT-27, pp. 472-478, 1979.

[135] Y. Teng, J. Sun, C. Chen, and H. Shao "Microwave Generation Enhancement of X-band CRBWO by Use of Coaxial Dual Annular Cathodes," *AIP Advances,* vol. 3, 072130-16, 2013.

[136] W. Rogowski and W. Steinhaus, "Die Messung der Magnetischen Spannung," *Archiv für Elektrotechnik,* vol. 1, pp. 141-150, 1912.

[137] J.D. Ramboz, "Machinable Rogowski Coil, Design, and Calibration," *IEEE Trans. Instrum. Meas.,* vol. 45, pp. 511-515, 1996.

[138] H. Bluhm, *Pulsed Power Systems: Principles and Applications* (Springer, New York, NY, 2006).

[139] K. Nalty, R. Zowarka, and L.D. Holland, "Instrumentation for EM Launcher Systems," *IEEE Trans. Magn.,* vol. 20, pp. 328-331, 1984.

[140] D. Pellinen and V. Staggs, "A Technique to Measure High-Power Electron Beam Currents," *Rev. Sci Instrum.,* vol. 44, pp 46 – 49, 1973.

[141] C. Leach, "High Efficiency Axial Diffraction Output Schemes for the A6 Relativistic Magnetron," Dissertation, Dept. of Elec. and Comp. Eng., University of New Mexico, New Mexico, 2014.

[142] A.I. Klimov, P.V. Vykhodtsev, A.A. Elchaniniov, O.B. Kovalchuk, I.K. Kurkan, S.D. Polevin, E.M. Tomeninov, and V.V. Rostov, "A Calorimeter for High Power Microwave Pulse Measurement," in *Proc. 15th Int. Symp. High Current Electron.* (Tomsk, Institute of High Current Electron. Sibir. Branch Russ. Acad. Sci., 2008), pp. 422-424.

[143] A. Das and S. Das, *Microwave Engineering, 2nd Ed.* (Tata McGraw Hill Education Private Limited, New Delhi, India, 2010).